01-Dec-2020

This is a non-peer reviewed preprint submitted to EarthArXiv. This manuscript has been submitted for publication in *Geophysical Journal International*. If accepted, the published version will be linked to this EarthArXiv submission. Please feel free to contact the authors with questions or comments.

Joel D. Simon
jdsimon@princeton.edu

# Recording earthquakes for tomographic imaging of the mantle beneath the South Pacific by autonomous MERMAID floats

Joel D. Simon[1], Frederik J. Simons[1] and Jessica C. E. Irving[2]
[1]*Department of Geosciences, Princeton University, Princeton, NJ 08544, USA, E-mail: jdsimon@princeton.edu*
[2]*School of Earth Sciences, University of Bristol, Bristol BS8 1RJ, UK*

**SUMMARY**
We present the first 16 months of data returned from a mobile array of 16 freely-floating diving instruments, named MERMAID for Mobile Earthquake Recording in Marine Areas by Independent Divers, launched in French Polynesia in late 2018. Our 16 are a subset of the 50 MERMAIDs deployed over a number of subsequent cruises in this vast and understudied oceanic province as part of the collaborative South Pacific Plume Imaging and Modeling (SPPIM) project, under the aegis of the international EarthScope-Oceans consortium. Our objective is the hydroacoustic recording, from within the oceanic water column, of the seismic wavefield generated by earthquakes worldwide, and the nearly real-time transmission by satellite of these data, collected directly above and on the periphery of the South Pacific Superswell. This region, characterized by anomalously elevated oceanic crust and myriad seamounts, is believed to be the surface expression of a deeply-rooted mantle plume. Tomographically imaging Earth's mantle under the South Pacific with data from these novel instruments requires a careful examination of the earthquake-to-MERMAID travel-times of the high-frequency *P*-wave detections within the windows selected for reporting by the discrimination algorithms on board. We discuss a workflow suitable for a fast-growing mobile sensor database to pick the relevant arrivals, match them to known earthquakes in the global earthquake catalogs, calculate their travel-time residuals with respect to global seismic reference models, characterize their quality, and estimate their uncertainty. We detail seismicity rates as recorded by MERMAID over 16 months, break these statistics down by magnitude to quantify the completeness of our catalog, and discuss magnitude-versus-distance relations of detectability for our network. The projected lifespan of an individual MERMAID is five years, allowing us to estimate the final size of the data set that will be available for future study. To prove their utility for seismic tomography we compare the MERMAID data quality against "traditional" land seismometers and their low-cost Raspberry Shake counterparts, using waveforms recovered from instrumented island stations in the geographic neighborhood of our floats. Finally, we provide the first analyses of travel-time anomalies for the new ray paths sampling the mantle under the South Pacific over the first 16 months of operation of our array.

**Key words:** MERMAID; South Pacific Ocean; Seismic-phase identification; Seismic velocities

## 1 INTRODUCTION AND HISTORICAL MOTIVATION

More than 70% of Earth's surface is covered by water. Seismic data recorded in the global oceans are sparse in both spatial and temporal coverage, especially in the Southern Hemisphere. Fig. 1 proves this point by mapping, in blue, the location of every seismic station retrievable from the Incorporated Research Institutions for Seismology (IRIS). While the map is indubitably incomplete, and the recorded presence of a station does not imply that the data are also available, it illustrates the sparsity of seismic sampling in the oceans, especially in the Southern Hemisphere.

Historically, seismic studies in and of the oceans have proven complex and costly. What follows is a brief recapitulation of the relatively short history of the field (only about one hundred seismic records from the deep-ocean bottom existed by the 1960s, according to Bradner 1964) to place MERMAID in its proper historical perspective (see also Simons et al. 2009).

Early attempts to instrument the oceans for regional and global seismology came in the form of encased seismometers dropped in free fall onto the seafloor from a ship, with or without anchored tether, and with a variety of mechanisms for recovery and data retrieval (Ewing & Vine 1938; Bradner 1964; Whitmarsh 1970).

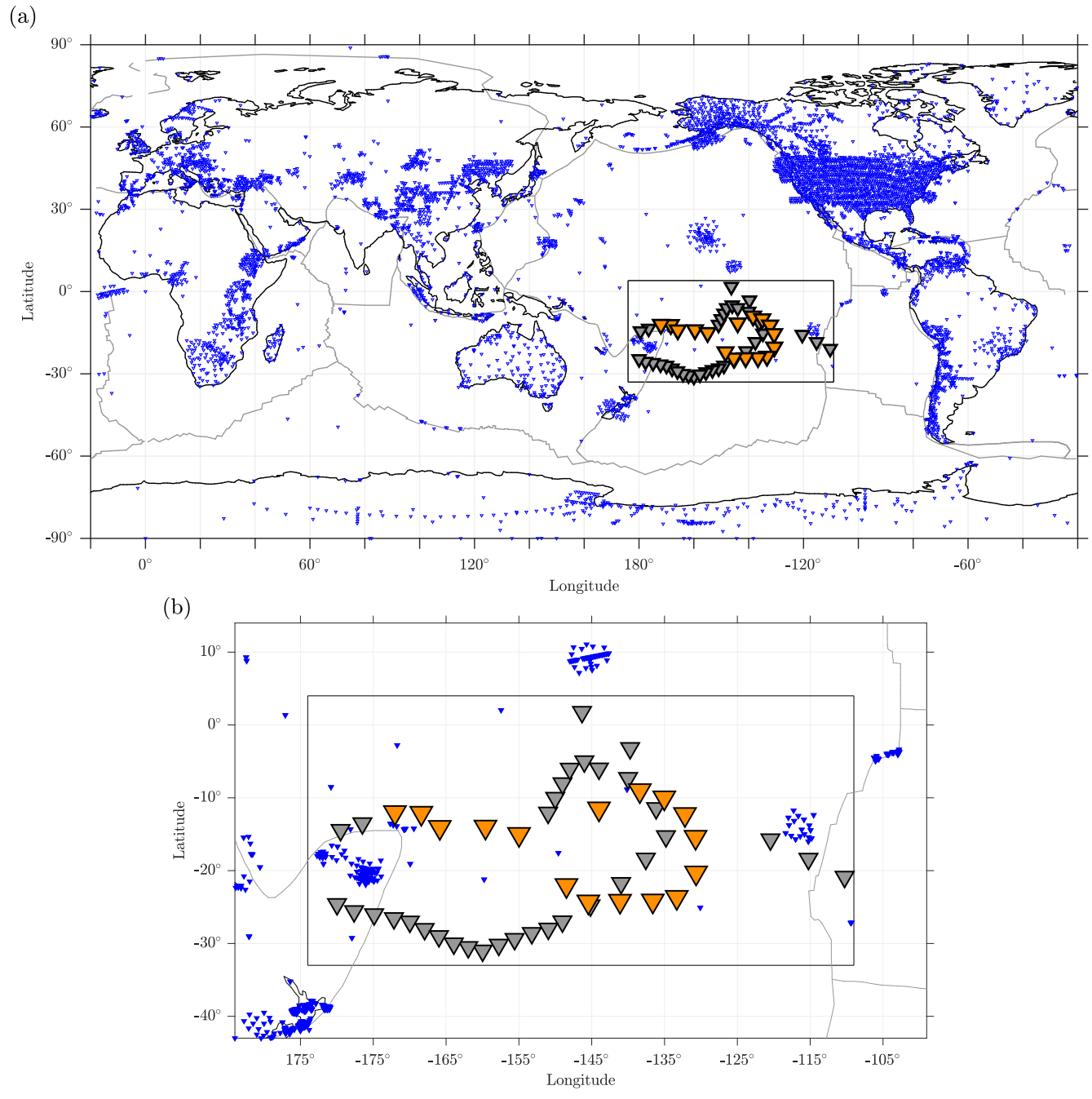


**Figure 1.** All seismic stations (smaller blue triangles) *ever* reported to the Incorporated Research Institutions for Seismology (IRIS), and the locations (orange and gray larger triangles) of the Mobile Earthquake Recording in Marine Areas by Independent Divers (MERMAID) at the time of their deployment: (a) global map that plots all 46295 reported stations; (b) zoom-in showing detail of the 50-MERMAID array in the South Pacific. The 16 MERMAIDs maintained by Princeton whose data are discussed in this study are highlighted in orange. The black rectangle drawn inside both maps is the boundary of the region searched for nearby island stations, the details of which are discussed in Section 9.

Progress toward true instrument autonomy came in the form of freely-drifting telemetered devices, either neutrally-buoyant mid-column floating versions of ocean-bottom sensors (e.g. Bradner et al. 1970), or sonobuoys, with a hydrophone loosely suspended from a surface buoy (e.g. Reid et al. 1973). Most of these experiments were short-lived due to power restrictions. Longer-lived moored sonobuoys (e.g. Kebe 1981) and moored hydrophones (e.g. Fox et al. 1993) could provide continuous hydroacoustic data at the expense of requiring seafloor cables to power them, restricting their spatial coverage.

In the last three decades, ocean bottom seismometry with long-life robust, three-component broadband sensors has positively flourished (Zhao et al. 1997; Webb 1998; Webb & Crawford 2003; Suetsugu & Shiobara 2014). Nevertheless, to this day such instruments remain physically large and expensive to install (Beauduin et al. 1996; Collins et al. 2001), requiring a specialized research

vessel both for deployment and recovery (Stephen et al. 2003), as establishing semi-permanent installations (e.g. Duennebier et al. 2002; Romanowicz et al. 2006) worldwide remains a developing goal for the international community (Montagner et al. 1998; Romanowicz & Giardini 2001; Favali & Beranzoli 2006; Kohler et al. 2020).

Evolving from single-station cabled seafloor installations (Butler et al. 2000; Petitt et al. 2002; Romanowicz et al. 2006), ambitious multi-station, multi-instrument cabled arrays have been rooted on the seafloor off the coasts of Japan (Hirata et al. 2002; Shinohara et al. 2014), the Canadian Northeast Pacific (Barnes et al. 2013; Matabos et al. 2016), and Oregon (Cowles et al. 2010; Toomey et al. 2014; Kelley et al. 2016) for the long-term monitoring of the oceanic environment from the shelf to the deep ocean. These installations provide high-quality data with low latency, but they require massive upfront costs, demand costly maintenance, are limited by cables and, being permanent, cannot be rapidly reinstalled or reassigned in the case of developing seismic crises (e.g. Duennebier et al. 1997).

The current fleet of recoverable ocean bottom seismometers (OBS) is autonomous but unable to transmit data while deployed, hence data acquisition and processing are separated by months or years, unless catastrophe precludes recovery (Tolstoy et al. 2006). More recently, wave-powered gliders that float at the surface and may be remotely controlled to remain in the vicinity of an ocean-bottom station have been used as a go-between to relay data from seafloor to shore via acoustic modem and satellite uplink (Berger et al. 2016). This coupling of technologies allows the delivery of seismic data from the seafloor in near real-time. While they have shown promise, such solutions remain costly to operate, and they have not yet enjoyed large-scale deployment. Kohler et al. (2020) proposed a pilot experiment that would see the installation of a long-term broadband seismic network on the seafloor utilizing the newest advances in wave glider and OBS technologies including in situ battery replacement. Campaigns like that proposed, where data are acquired autonomously and in near real-time, and instrument lifespans measured in years instead of weeks or months, will generate data sets that nicely complement those returned by MERMAID.

Beyond gliders, still other solutions to the logistical problem of data recovery are currently being tested. These include ocean-bottom systems that periodically release data pods from the seafloor, each with a self-contained telecommunications unit to relay data via satellite upon surfacing (Hammond et al. 2019). Finally, while the age where the cables themselves may act as seismic sensors appears to have arrived (e.g. Lindsey et al. 2019; Sladen et al. 2019; Williams et al. 2019), such technology is in its infancy.

Despite those advances in technology, no single seismic instrument has solved all the issues just presented: the ability to deliver high-quality data with autonomy, low cost, low latency, and nimbleness. Nor should we assume that any single instrument can be designed to optimize for all. Our instrument, MERMAID, fills a gap in instrumentation by providing low-cost hydroacoustic records suitable for global seismology (Simons et al. 2006b) from the oceans in near real-time (Hello et al. 2011) without the requirement of a research vessel for deployment and, being unrecovered, negating the need for a recovery cruise.

While MERMAID's data sets of hydroacoustic time series, collected by a single limited-bandwidth hydrophone floating at mid-column water depths, forever will remain less "complete" in comparison with data sets recorded by a well-coupled three-component broadband ocean-bottom seismometer, its benefits are its lower manufacturing costs, its logistical simplicity, its algorithmic flexibility (Sukhovich et al. 2011, 2014) in selecting promising seismic phases to report with each surfacing, and its longevity—currently projected to be about five years (∼250 dive cycles) on a single battery charge. Hence, MERMAID can be thought of as a 21st century sonobuoy without the previous century's drawbacks. Fulfilling the promise of the first-generation MERMAID instrument (Simons et al. 2009) and substantiating the record accumulated by MERMAIDs of the second generation (Sukhovich et al. 2015; Nolet et al. 2019), the over 1300 records presented here, collected by the current third generation of instruments, constructed by OSEAN SAS of Le Pradet, France, *are* closing the seismic data gap in the world's oceans.

Studying the interior of the Earth using seismic tomography (Nolet 2008; Romanowicz 2008; Rawlinson et al. 2010), primarily of *P*-delay times, was, and remains to date, MERMAID's primary strength and objective. Joubert et al. (2016) and Nolet et al. (2019) have shown that the accuracy of MERMAID's position underwater, interpolated from multiple surfacings, and the accuracy with which the arrival time of seismic *P* phases can be determined from the sometimes noisy acoustic records, are of sufficiently high quality to constrain velocities for tomographic inversion. Simon et al. (2020) presented a new algorithm for the multiscale estimation of event arrival times and their precision, which closes the loop from detection and discrimination of *P* waves in the ocean, to the accurate determination of their travel times, to the assessment of their uncertainties.

In this paper we leverage all of these developments and present the first 16 months of data returned by the 16 MERMAIDs owned and operated by Princeton University that were deployed in French Polynesia in August and September 2018. We compare their waveforms with traces available from 20 seismic island stations in the same region, and with records from a set of five comparatively less expensive, but increasingly more abundant, Raspberry Shake (Anthony et al. 2019) instruments.

We study the statistics of our growing catalog of seismic data, a lasting product of this study, to comment on its completeness, and to estimate the total number of tomographic-quality records that can be expected to be returned per MERMAID over its projected five-year lifetime. We compute MERMAID travel-time residuals against the one-dimensional (1-D) ak135 velocity model of Kennett et al. (1995), we correct those residuals for bathymetry and MERMAID's cruising depth, and, lastly, readjust them using the fully three-dimensional (3-D) and elliptical *P*-wave speed model LLNL-G3Dv3 of Simmons et al. (2012). We estimate the uncertainties on our residuals, compute signal-to-noise ratios, and compare these statistics with a complementary data set derived from traditional seismometers and Raspberry Shake stations installed on ocean islands. These travel-time residuals will be the inputs for future tomographic studies, with our uncertainties serving as weights in the inversion.

Finally, for a taste of the likely signals from the Earth's mantle

**Figure 2.** A MERMAID being deployed as part of the South Pacific Plume Imaging and Modeling (SPPIM) project. (*Left*) François Quemeneur and Jean-François "Jeff" Barazer launching MERMAID from R/V *Alis* in September 2018. (*Right*) Lead engineer Yann Hello aboard R/V *L'Atalante* in August 2019. In the background: Fernand Le Bousse. Photo by Lucas Sawade.

that will emerge from our data collection, we project our carefully-measured residuals onto their 1-D ray paths to reveal average velocity perturbations with respect to the 1-D velocity model that tomography will further image.

## 2 THE MERMAID INSTRUMENT

The purpose of the MERMAID float is to return seismic data of tomographic quality from the global oceans in near real-time. The instrument (Fig. 2) and its dive cycle (Fig. 3) were inspired by oceanic floats (Swallow 1955; Rossby & Webb 1970; Davis et al. 1992, 2001), which have become ubiquitous in the global oceans (see Gould 2005, for historical perspective). A major player in this arena is the international Argo program, which has been continuously providing the scientific community with a wealth of temperature, salinity, and trajectory data over the last several decades (Lavender et al. 2000; Roemmich et al. 2009; Davis 2005; Abraham et al. 2013). Along with the payload required for in situ observations and hydrographic profiling, a contemporary APEX Argo float is equipped with a hydraulic pump which modulates an expandable bladder that allows it to be neutrally buoyant at many mid-column depths, a Global Positioning System (GPS) for location tracking, and a satellite link for data transmission.

Argo floats collect and transmit data over repeated dive cycles. A typical cycle begins with the float deflating its bladder to achieve negative buoyancy so that it may sink to a predetermined parking depth (generally between 1000 m to 2000 m below the sea surface), at which point it passively drifts at depth for a set amount of time (usually around 10 days), before finally reinflating its bladder to slowly rise back to the surface. During this ascent it samples and processes a roughly vertical column of water via a conductivity-temperature-depth (CTD) sensor. Once at the surface it acquires a GPS fix, transmits the new data via satellite, and repeats the process. Because they are autonomous and drift at the whim of ocean currents Argo floats are practically guaranteed to sample the water column at a previously unsampled location every time they ascend. As of 11 April 2020 there were 4060 Argo floats actively reporting from within every ocean on Earth, and on average some 800 are being deployed yearly to maintain the fleet. Like MERMAID, they are not designed to be recovered.

The first-generation MERMAID float was a modified Sounding Oceanographic Lagrangian Observer (SOLO) float (Davis et al. 2001), fitted with a hydrophone and a custom algorithmic processing unit so that it returned seismologically viable hydroacoustic data recorded at its parking depth (Simons et al. 2006b, 2009). The second-generation MERMAID (Hello et al. 2011; Sukhovich et al. 2015) was a modified APEX float built by Teledyne Webb Research. The current third-generation MERMAID is a redesign from the ground up by Yann Hello at GéoAzur and French engineering firm OSEAN SAS. It is an autonomous robotic float consisting of a High Tech HTI-96-MIN_HEX hydrophone, a Gardner DENVER pneumatic pump, a Garmin GPS 15 unit, a Motorola 9522 two-way Iridium communication module, Electrochem lithium batteries, and dedicated onboard detection and discrimination software (Sukhovich et al. 2011). Once deployed MERMAID sinks to a predetermined depth (usually 1500 m) and records the ambient acoustic wavefield while freely drifting with the mid-column currents. If triggered by seismic activity, or once a threshold time is reached, MERMAID surfaces, transmits the new data, downloads mission-command files via satellite, and repeats the process. Fig. 3 shows the first five dive cycles completed by MERMAID P012 after its deployment on 10 August 2018, and Fig. 4(a) shows the drift trajectories of all 16 MERMAIDs discussed in this study.

The current onboard algorithm used to monitor and process the ambient acoustic wavefield (Sukhovich et al. 2011, 2014) was designed specifically to trigger on tomographic-quality teleseismic *P*-wave arrivals sensitive to mantle structure. Once parked at depth the hydrophone is switched on and data acquisition starts. The hydroacoustic data are processed in real-time by a short-term average over long-term average (STA/LTA) algorithm (Allen 1978), and written to a Secure Digital (SD) card, which retains those data for one year. If the adjustable STA/LTA threshold is exceeded, a windowed section of those data are further interrogated via wavelet decomposition (Simons et al. 2006a), and its energy distribution across six wavelet scales is compared with statistical models of various signals known to exist in the oceans (many of which are not generated by seismic events).

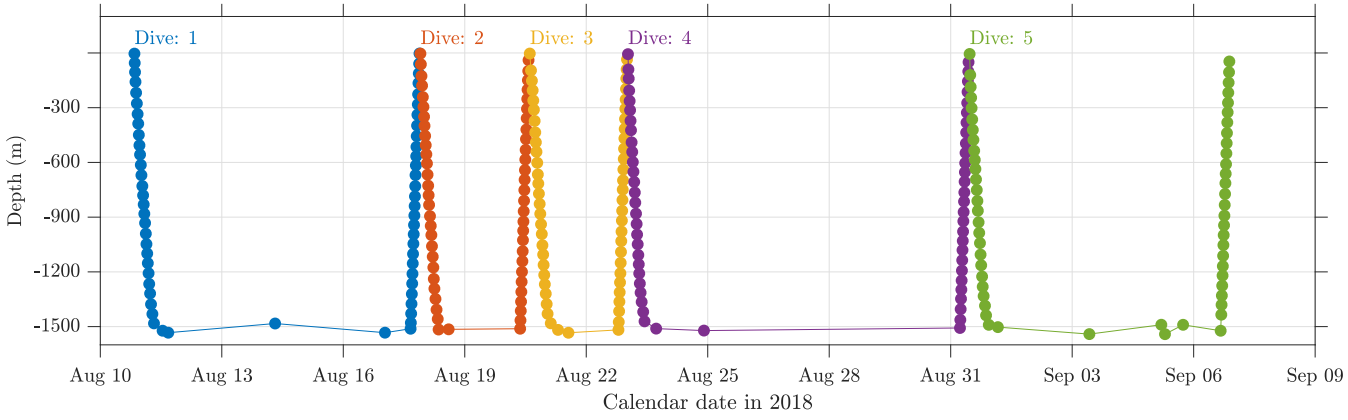


**Figure 3.** The first five dive cycles completed by MERMAID P012 after its deployment on 10 August 2018. The parking depth for MERMAIDs discussed in this study was 1500 m, though, like nearly all mission parameters, this may be adjusted via the two-way Iridium satellite link. Filled circles mark individual pressure readings taken by the onboard pressure sensor and they are connected by similarly colored lines to visually separate each dive cycle. In this example (again, adjustable) descent speeds are on the order of $-2.8\pm1.2$ cm/s ($-100.3\pm44.8$ m/h), translating into $15.5\pm5.3$ h to sink from the surface to the parking depth, while ascent speeds are on the order of $8.0\pm0.2$ cm/s ($289.8\pm8.4$ m/h), meaning it takes MERMAID $5.1\pm0.2$ h to ascend from depth to the surface. MERMAID's onboard detection algorithm prompts immediate surfacing when it records a signal it considers with a high likelihood to be a teleseismic *P* wave, which explains the abbreviated durations of the second and third dives compared to the others in this figure. This rapid triggering and transmission allowed us to receive record sections like those in Fig. 5 within hours of large earthquakes. Depth data were retrieved from MERMAID log files using software written by Sébastien Bonnieux.

A quality criterion is assigned to the signal that encodes the probability that the record under inspection includes a *P*-wave arrival. If it is high enough MERMAID immediately ceases data acquisition, regardless of how long it has been at depth, and surfaces to transmit the signal. Other candidate signals that do not trigger an immediate surfacing are stored on the buffer and marked for transmission at the next opportunity. Currently as its default, and for all records discussed in this study, MERMAID transmits the Cohen-Daubechies-Feauveau (2,4) wavelet and scaling coefficients (Cohen et al. 1992) from scales two through six of a time series originally sampled at 40 Hz and filtered between 0.1 Hz and 10 Hz before digitization. This means that, after reconstruction via inverse wavelet transformation, the MERMAID records presented here are hydroacoustic pressure time series of seismic conversions sampled at 20 Hz.

MERMAID delivers seismic data from the oceans in near real time, with immediate surfacing and data transmission within hours of the largest events. MERMAIDs are individually programmable and mission parameters such as parking depth, maximum time to remain there, criterion thresholding values to trigger surfacing, and so on, all may be monitored and adjusted thanks to two-way Iridium communication. While the ability exists to request data from the MERMAID buffer for up to one year prior (which we have done with success), we found the default trigger algorithm to perform exceptionally well, and in this study we will restrict our discussion to only those triggered records which MERMAID sent us on its own accord. Indeed the default onboard algorithm was left untouched for the entirety of the deployment for all 16 floats discussed here.

## 3 THE EARTHSCOPE-OCEANS CONSORTIUM

The EarthScope-Oceans consortium was founded in 2016, and now counts members from the US (Princeton University, among whom the authors, IRIS Seattle, DBV Technology North Kingstown, RI), Japan (Kobe University, JAMSTEC, ERI), France (Géoazur Sophia Antipolis, EOST Strasbourg, IFREMER Plouzané, OSEAN Le Pradet), South Korea (KIGAM Daejeon), New Zealand (GNS Science, Lower Hutt), the UK (University of Oxford), and China (SUSTech, Shenzhen).

EarthScope-Oceans represents a multidisciplinary group of geoscientists who are coordinating efforts to create a global network of sensors to monitor the Earth system from within the oceanic environment. It intends to shepherd national projects into the international forum where globally relevant, applicable, and mutually agreed-upon decisions can be made on technological aspects of instrument development, science objectives and priorities on different time scales, data management, dissemination, archiving, and education and outreach efforts; much like IRIS (`https://iris.edu/`) or ORFEUS (`http://orfeus-eu.org/`) are doing for the land-based seismological communities today.

EarthScope-Oceans is partnered with the Joint IOC-World Meteorological Organization Technical Commission for Oceanography and Marine Meteorology and abides by the UNESCO agreements on global ocean observation systems, which spell out end-of-life provisions for MERMAID.

The Federation of Digital Seismic Networks (FDSN) granted MERMAID data its own seismic network code (2003; see `https://fdsn.org/networks/detail/MH/` for detailed information). MERMAID floats generate location data, instrumental metadata, and acoustic waveforms. All data recorded during the lifetime of MERMAID floats will be openly accessible from the IRIS Data Management Center (DMC) as soon as technically feasible and with a maximum two-year delay from collection.

## 4 THE MERMAID SPPIM DEPLOYMENT

The 16 Princeton-operated third-generation MERMAIDs whose data are the subject of this study are just one component of the South

Pacific Plume Imaging and Modeling (SPPIM) project, an array of 50 MERMAIDs deployed into the South Pacific to study the underlying mantle composition and temperature with seismic tomography. Drifting united under the EarthScope-Oceans banner, these MERMAIDs are supported and maintained by our global consortium (`http://earthscopeoceans.org`).

A 24-hr trial run completed 12 April 2018 was led by Kobe University's Hiroko Sugioka and JAMSTEC's Masayuki Obayashi from the R/V *Fukae Maru*. During this test deployment MERMAID N003 recorded the magnitude $m_b$ 4.9 earthquake originating at 59.4±5.8 km depth, 56±6.6 km east of Ishinomaki, Japan (according to `https://earthquake.usgs.gov/earthquakes/eventpage/us2000dyw3/`), some 824 km distance from the instrument, which floated 469 m below the surface at the time.

The complete SPPIM array, shown as gray and orange upside-down triangles in Fig. 1, was deployed over several cruises led by Yann Hello (see Fig. 2), research engineer at IRD/Géoazur, chief designer of MERMAID in its current third generation, as currently commercially available from OSEAN SAS of Le Pradet, France.

On the first leg (Nouméa, New Caledonia to Mata-Utu, Wallis & Futuna, 21–28 June 2018), Yann Hello deployed two GéoAzur units from IRD/Genavir vessel R/V *Alis*. On the second leg (Mata-Utu to Papeete, Tahiti, French Polynesia, 3–13 August 2018), Hello deployed five Princeton units from the R/V *Alis*. On the third leg, Frederik Simons deployed 11 Princeton units from the R/V *Alis*, which departed Papeete on 28 August 2018, returning to the same port on 16 September of the same year (`https://campagnes.flotteoceanographique.fr/campagnes/18000519/`, doi: 10.17600/18000519). During this leg, the R/V *Alis* completed a nearly circular trajectory, which can be traced in Fig. 4 by connecting the deployment locations (dark blue) of MERMAID P013, P016, P017, etc., and continuing clockwise back to Tahiti (note that no instruments named P014 or P015 were ever deployed). It was during this cruise that the deployment of the 16 MERMAIDs operated by Princeton was completed.

Five Japanese units were launched from the R/V *Mirai* by Masayuki Obayashi, sailing from Shimizu, Japan to Valparaiso, Chile between 11 December 2018 and 24 January 2019.

The fourth leg (Papeete–Nouméa, 4–29 August 2019) was led by Hello, Obayashi, Zhen Guo and Yong Yu (SUSTech) from the R/V *L'Atalante* (`https://campagnes.flotteoceanographique.fr/campagnes/18000882/`, doi: 10.17600/18000882). This cruise saw the completion of the SPPIM array with the deployment 23 SUSTech MERMAIDs and an additional four from Kobe University.

### 4.1 *MERMAID in its geographic and geologic context*

It bears repeating that MERMAIDs drift with the ocean currents—they do not land on the seafloor like traditional ocean-bottom seismometers (although a "lander" version is currently under development). Fig. 4(a) shows the drift trajectories of all 16 Princeton-operated floats discussed in this study. Every dot represents one GPS fix taken by MERMAID while at the surface, color-coded to show the amount of time elapsed since its deployment (with dark blue representing the launch day, and dark red the last GPS fix of 2019). Each MERMAID trajectory is labeled by the corresponding serial number of the float, excluding the "P0" prefix. By connecting these dots we obtain an approximate (Davis 2005) map of the ocean currents at 1500 m depth, where MERMAID spends the most time. See Nolet et al. (2019) for drift statistics broken down into surface and abyssal components. Also labeled in Fig. 4(a) are the locations of other seismic sensors against which MERMAID data are compared later in this study. Those station locations are marked by upside-down triangles, with the notable exception the collection of stations on Tahiti, French Polynesia, marked by a larger right-side up triangle, to represent the many stations installed there and listed in the legend in the upper-right corner. For the sake of spacing in Fig. 4(a), those station names have had their International Federation of Digital Seismograph Networks (FDSN) and/or network abbreviations removed.

For added geologic and geodynamic context Fig. 4(b) shows a bathymetry map of the same region. We see myriad islands, seamounts (Wessel et al. 2010), hotspot tracks (Wessel & Kroenke 1997), and, in lighter greens, large swaths of anomalously elevated oceanic crust known as the South Pacific Superswell (McNutt & Fischer 1987; McNutt & Judge 1990).

Going deeper into the Earth, Fig. 4(c) maps, at 2700 km depth, the number of models out of five "voting" for anomalously slow *P*-wave velocities according to the clustering analysis of Cottaar & Lekić (2016). The models used there were HMSL-***P***06 (Houser et al. 2008), GyPSuM (Simmons et al. 2010), LLNL-G3Dv3 (Simmons et al. 2012), *SPani* (Tesoniero et al. 2015), and ME2016 (Moulik & Ekström 2016), with the $V_p$ components used where models described both $V_p$ and $V_S$. Cottaar & Lekić (2016) classified *P*-wave velocities at discrete locations within those five models into three bins: slow, neutral, and fast. They deemed three models concurring a "majority," and five a "consensus."

In Fig. 4(c) we see large swaths of dark red (five votes), proving that there is consensus among all models that broad regions of anomalously slow *P*-wave velocities lie at the base of the mantle under the South Pacific. This region is known as the Pacific Large Low-Velocity Province (LLVP) and is one of two nearly antipodal such regions on Earth, the other being the African LLVP (Garnero et al. 2016). Tanaka et al. (2009a) showed that the lower mantle directly below the South Pacific Superswell is characterized by anomalously slow *P*-wave velocities, although the exact nature of the interaction between LLVPs and surface features like oceanic hotpots and the South Pacific Superswell has long been a topic of debate (e.g. Davaille 1999; Adam et al. 2014). Compelling evidence in the form of whole-mantle tomography (French & Romanowicz 2015) implies that the former may feed the latter via conduits of hot uprising rock that span, potentially discontinuously, from the core-mantle boundary to the surface. The exact geometries, dimensions, and rooting structures of these conduits within or near the boundaries (Cottaar & Romanowicz 2012) of LLVPs remain an area of active research (Garnero et al. 2016), and none of those outstanding questions are resolved in the present study. However, what is known for certain is that the Pacific LLVP is expansive in breadth and height, purportedly rising to the mantle transition zone under the South Pacific Superswell (e.g. Tanaka et al. 2009b; Cottaar & Lekić 2016), it is characterized by anomalously slow seismic velocities, and it lies under our SPPIM deployment. The

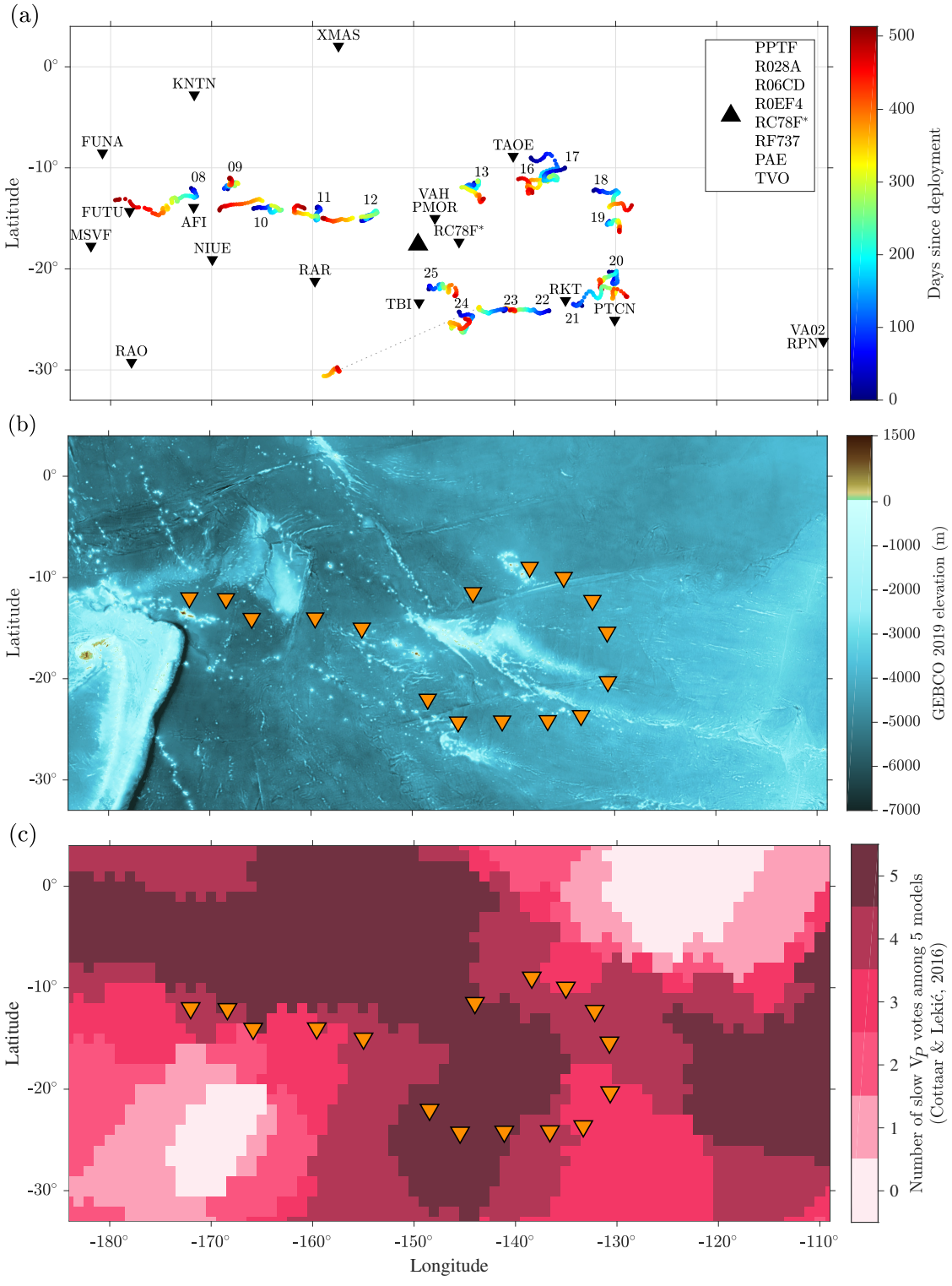


**Figure 4.** (a) MERMAID trajectories with time, and the locations of stationary nearby island stations. This map is a zoom-in of the rectangles drawn inside Fig. 1(a and b), representing a bounding box with edges framed roughly 2° beyond the extent (in all four cardinal directions) of the complete 50-MERMAID SPPIM project at the time of deployment, and representing the total area searched for additional island seismic data in Section 9. Here only the drift-trajectories of the 16 Princeton-operated MERMAIDs that contributed data to this study are shown. The trajectories are color-coded by the time elapsed since deployment, where dark blue represents the location at the time of deployment, and dark red represents the last GPS fix of 2019. Therefore, these trajectories trace an approximate map of ocean currents at 1500 m, the parking depth of MERMAID. The locations of nearby island seismic installations are marked by upside-down triangles, except in the case of a single, large right-side up triangle representing the collection of stations on Tahiti, French Polynesia. Station RC78F appears twice in this map, and its name is starred in the legend, because it was relocated during our experiment. (b) Deployment locations of our 16 MERMAIDs (orange triangles) overlain on a map of bathymetry and topography from the GEBCO 2019 model (Weatherall et al. 2015; GEBCO Bathymetric Compilation Group 2019). (c) Deployment locations of our 16 MERMAIDs overlain on a map of showing the number of votes, among five models, for anomalously slow *P*-wave velocities at 2700 km depth according to the clustering analysis of Cottaar & Lekić (2016).

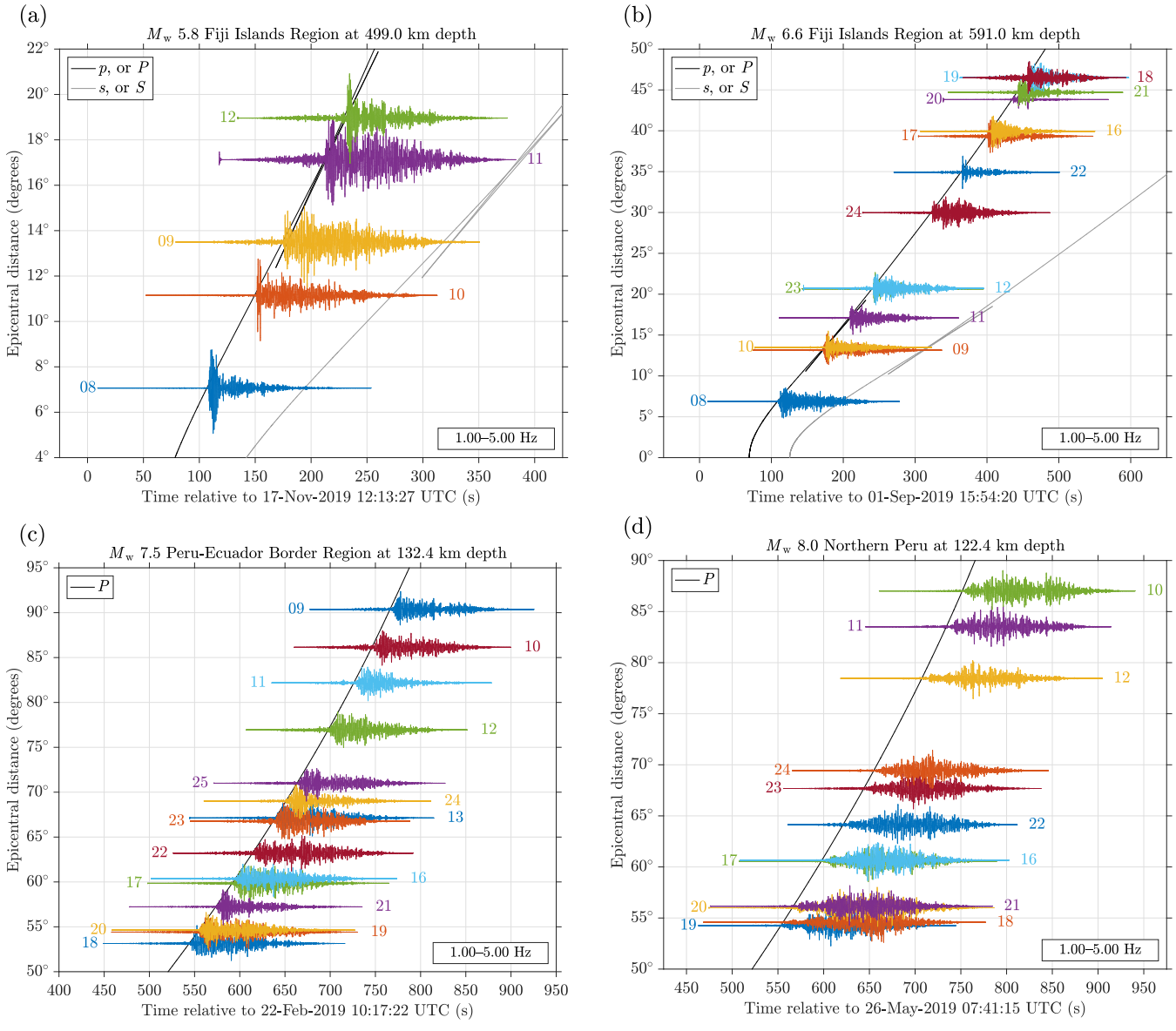


**Figure 5.** Examples of MERMAID record sections. In every panel different colors correspond to individual MERMAIDs reporting the relevant records, which are shown with unit scaling, filtered between 1–5 Hz. For the events identified in the titles theoretical travel-time curves in the ak135 velocity model (Kennett et al. 1995) are overlain as shown in the legend.

teleseismic arrivals recorded by MERMAID are therefore expected to sample slow regions of the deep mantle, and their measurement will help refine future tomographic studies.

## 5 MATCHING SEISMOGRAMS TO EARTHQUAKES

Fig. 5 is our first example of seismograms recorded by MERMAID as part of the SPPIM project. We show record sections corresponding to four earthquakes, one each within the magnitude ranges: (a) *M*5–5.9; (b) *M*6–6.9, (c) *M*7–7.9, and (d) *M*8–8.9. The seismograms in Figs 5(a–d) are individually color-coded to distinguish the records reported by each MERMAID, whose instrument number is displayed before or after each trace (excluding the "P0" prefix, and noting that the color assignments differ between panels). The seismograms are uncorrected pressure records in their native units of digital counts. By default, MERMAID sends 200 to 250-s-long seismograms, and the seismograms plotted here were demeaned, detrended, and tapered with a symmetric cosine (Hann) taper, before being band-pass filtered between 1 and 5 Hz using a one-pass, four-pole Butterworth filter. Each trace is normalized for plotting purposes, resulting in arbitrary amplitudes within, and between, the panels of Figs 5(a–d). The black solid and/or dashed lines correspond to the theoretical travel times of the phase(s) quoted in the legend, as computed in the ak135 velocity model (Kennett et al. 1995).

The MERMAID onboard detection algorithm identifies time series determined via probabilistic wavelet-subspace analysis to be likely teleseismic *P*-wave arrivals. The algorithm does not provide arrival-time picks beyond the precision afforded by the underlying STA/LTA detection algorithm, nor is it privy to recent global seismicity. Therefore, to produce record sections like those

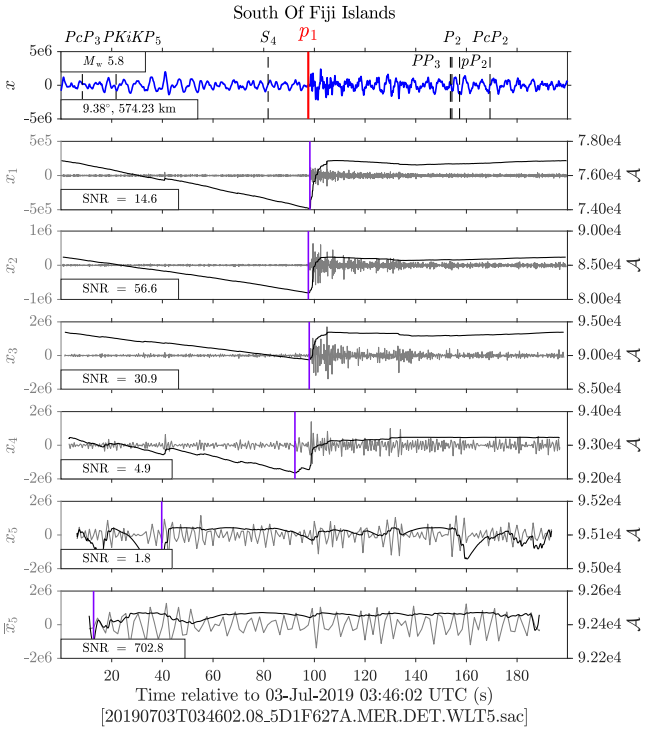


**Figure 6.** MERMAID seismogram after preliminary matching, as displayed for the researcher during manual event verification. The blue trace in the first panel is the raw seismogram, while the gray traces in the underlying panels are the wavelet-subspace projections at five scales, each overlain by their associated Akaike information criterion (AIC) curve (black) and AIC-based arrival-time pick (purple), as described by Simon et al. (2020). The top panel is annotated with the theoretical arrival times of various phases from five distinct earthquakes, as noted in the subscript, computed in the ak135 velocity model, and marked in time by vertical lines. These represent all the phases which have theoretical arrival times within the time window of the seismogram, associated with known global seismic events in the catalogs queried from IRIS. The time of the first-arriving phase associated with the largest earthquake in the set ($p_1$) is marked by a solid red vertical line. Its theoretical arrival time agrees well with the AIC-based arrival-time pick (which is agnostic of seismology) at the first three scales. The agreement of these two distinct estimated arrival times, each calculated in very different ways, lends itself to the confident assignment of "identified" to this seismogram. During manual review this figure (and a secondary, zoomed-in version) is displayed to the researcher, along with the event metadata for all potentially matching events, and they are led through a series of intuitive prompts in MATLAB for easy matching and sorting.

of Fig. 5 we must first determine if the seismograms sent by MERMAID match any events in a global catalog. In this study we searched the USGS National Earthquake Information Center (NEIC) Preliminary Determination of Epicenters (PDE) Bulletin (`https://earthquake.usgs.gov/data/comcat/catalog/us/`) for recent events.

### 5.1 *Automated preliminary matching*

Upon receipt of a fresh seismogram transmitted by MERMAID we immediately wish to determine whether or not the signals it contains correspond to known seismic events. To that end we have developed a complete workflow executed in MATLAB to match untagged, raw seismograms to global seismic catalogs with minimal user intervention. This first step discussed next—the algorithmic querying of global catalogs, the tagging of likely events, the annotating of seismograms with their theoretical phase arrival times, and the multiscale detection of phases against which residuals are displayed—occurs automatically and without user intervention after a MERMAID transmits a new seismogram.

The preliminary matching process begins with the querying of global seismic catalogs with `irisFetch.m` (`https://github.com/iris-edu/irisFetch-matlab/`), a software packaged and distributed by IRIS, for seismic events that occurred in the hour preceding the seismogram. Next, travel times are computed for seismic body waves that are likely to be present in the record using `taupTime.m` (see Section 12 and the Supplemental Material for details) for the ak135 velocity model. Each event with one or more phase-arrivals in the time window of the seismogram is deemed a preliminary match, and all such events are sorted by magnitude (generally the single greatest factor determining phase identification) and saved together as individual structures (a MATLAB data type) in a binary (*.mat) "unreviewed" file.

Preliminary matching generates two Portable Document Format (PDF) plots, both displaying the raw seismogram on which the theoretical phase-arrival times of possible events are marked, and with panels showing wavelet-subspace projections (which are roughly analogous to non-overlapping frequency bands) of the seismogram at five scales. Overlain on the subspace projections are arrival-time picks estimated using an Akaike information criterion (AIC; Akaike 1998) method that is briefly discussed in Section 7.1 and at length by Simon et al. (2020). The first PDF, an example of which is Fig. 6, displays the complete seismogram, and the second (not shown here) is truncated to show detail about a 100 s window centered on the first arrival of the event with the largest magnitude among all potential matches. Usually that is the true match, and thus the seismogram in the top panel of Fig. 6 is annotated using those metadata, its first-arriving phase highlighted a solid red line to set it apart from all other possible phases in the time window of interest rendered in dashed black lines. All named phases are labeled in the top panel, with subscripts identifying the rank of the associated event in the magnitude-sorted preliminary match list. Hence, in Fig. 6, $p_1$ is the theoretical arrival time of a $p$ wave generated by the first preliminary event match, and, $S_4$ is the theoretical arrival time of an $S$ wave from the fourth possible event match.

These preliminary matches are automatically generated and the algorithm only requires a SAC file (Helffrich et al. 2013) as input; i.e., the only relevant information ingested by the algorithm in this preliminary-matching stage is a (mobile) receiver location and a time window (both, of course, being contained in the SAC file itself). Hence, our procedure is not specific to MERMAID data, and we may reasonably assume that it has application beyond the scope of this study, e.g., for single-station or array deployments of traditional broadband land instruments, perhaps in the context of Nuclear Test Ban Treaty verification, Raspberry Shakes (Bent et al. 2018; Anthony et al. 2019; Calais et al. 2019), or various other forms of crowd-sourced "citizen" seismology, e.g., recorded by mobile phones (Kong et al. 2016) or other low-cost instruments (Cochran et al. 2009; Jeddi et al. 2020), and for classroom seismic installations (Balfour et al. 2014; Subedi et al. 2020), where

an experienced researcher may not available to guide the matching process. Further, while the code is provided with default parameters optimized for MERMAID data they are easily tunable to a variety of seismic applications.

### 5.2 *Manual winnowing and sorting*

The second step of the matching procedure involves manual review of the preliminary matches. The review process is simple and intuitive and results in the seismograms being sorted into two classes: "identified" and "unidentified." Those in the former class will have been assessed to contain energies consistent with phase arrivals corresponding to known earthquakes in global seismic catalogs, both by visual inspection and by considering their travel time residuals with respect to the AIC picks. For every SAC file reviewed, the two PDFs generated in the first step are automatically opened for inspection, and the interactive program guides the user through a series of prompts to determine if the event can be identified, and if so, which event(s) and phase(s) should be saved.

The process begins with a helpful printout of metadata on all potential events, with specific focus given to the largest event in the list and its corresponding residuals. At all times the user has quick access to all events, and their corresponding residuals, thanks to their MATLAB structure variables being loaded automatically with each seismogram under review.

We refer again to Fig. 6, whose top panel plots the raw seismogram in blue. The arrival times marked on that top panel are the ak135 predictions. The panels below the first plot the subspace projection of the seismogram at five wavelet scales in gray, the amplitude of which corresponds to the left ordinate axis. Overlain in black in each panel is the associated AIC curve used to generate the arrival-time pick at that scale, $\mathcal{A}$, corresponding to the right ordinate axis. This curve is essentially an inverted likelihood-curve: where it is low, an arrival is likely. The specific AIC arrival-time pick is marked at each scale by a purple vertical line. Quoted in the legend are the corresponding signal-to-noise ratios (SNRs), defined to be the ratio of the maximum-likelihood estimates of the variances of the signal and noise segments,

$$\mathrm{SNR} = \hat{\sigma}^2_{\mathrm{signal}}/\hat{\sigma}^2_{\mathrm{noise}}, \tag{1}$$

the "signal" being the segment after the AIC pick, and the "noise" the segment preceding it. Later in Section 7 we redefine the noise and signal segments en route to identifying with high-precision the arrival times of first-arriving *P* waves in a single frequency band. There, the seismograms being analyzed have already been positively matched to an identified event, which differs from the procedure here, where we wish to inspect the full bandwidth of each seismogram via a multiscale decomposition.

It is important to note that the AIC-based picks are agnostic of seismology. It is their agreement, or lack thereof, with the theoretical arrival times of the phases from the match list that inform the decision to designate a seismogram as "(un)identified." In the case presented in Fig. 6, the purple AIC picks at subspace projection scales one ($x_1$) through three ($x_3$) agree well with the theoretical arrival time of the first-arriving *p* wave computed in ak135. The AIC picks at the other scales are either low-SNR or very near an edge and may be disregarded. We also note that the picks shown here are not influenced by the edges, whose treatment we describe in Simon et al. (2020), so users need not necessarily be wary of an arrival pick near an edge. However, we have noticed that our AIC picker will on occasion report an extremely short noise or signal segment associated with a time series has no clear arrival (the entire seismogram looks like noise). An example of this behavior is the noise segment in the last panel of Fig. 6, $\overline{x}_5$, which is extremely abbreviated, consistent with its having low variance, most unlike the variance of the signal segment. Therefore, a low-SNR signal that is very near an edge does warrant a close inspection. Regardless, because of he agreement between the theoretical arrival time of the *p* wave corresponding to the largest event and the AIC picks at high scales in Fig. 6, this seismogram would be counted among the identified category.

This sorting is accomplished via simple prompts that guide the user through a winnowing process that ultimately results in the seismogram being classified as identified or unidentified, and the relevant event data being saved to a binary (*.mat) "reviewed" file.

Ultimately the decision to mark a seismogram as identified or unidentified comes down to experience processing MERMAID seismograms like the one presented in Fig. 6. The hope, however, is that the workflow developed here is simple enough for new researchers with some experience processing seismic data to quickly grasp and apply it to their own untagged data with minimal training. Indeed, our workflow is already being successfully applied to the 23 SUSTech instruments included in the SPPIM deployment—albeit applied to the same type of data in this case, but importantly, matched by a different researcher.

## 6 THE MERMAID SEISMIC CATALOG

The process just outlined enabled the matching of seismograms to earthquakes in our growing MERMAID seismic catalog, the inspection of which is the focus of this section. We first take a broad look at the catalog itself, before drilling down to the statistics of the rate of return of identified events for individual MERMAIDs. We will also discuss the completeness of our catalog as compared to other global seismic catalogs available over the period of interest, considering the entire activity time of each of the 16 floats through the end of 2019. In this section, when we refer to the "catalog" we specifically mean the seismic catalog of recorded earthquakes, not the catalog of travel-time residuals, which we discuss later. The purpose of this section is to answer questions relevant to any new seismic instrument, such as: "How many earthquakes does MERMAID record per year, and what are the distributions of their magnitudes, epicentral distances, and locations?"; "What do the recorded magnitude-distance relations tell us about detectability thresholds?"; and, "What is the probability that any single earthquake will be recorded by any single MERMAID, and how many earthquakes is each projected to record in its lifetime?"

### 6.1 *Catalog summary: in pictures*

Figs 7 and 8 summarize the MERMAID seismic catalog to date. Fig. 7 plots histograms of earthquake magnitudes and distances, and combines those data with the SNR of the first-arrival in the first global earthquake-detectability diagram for the third-generation

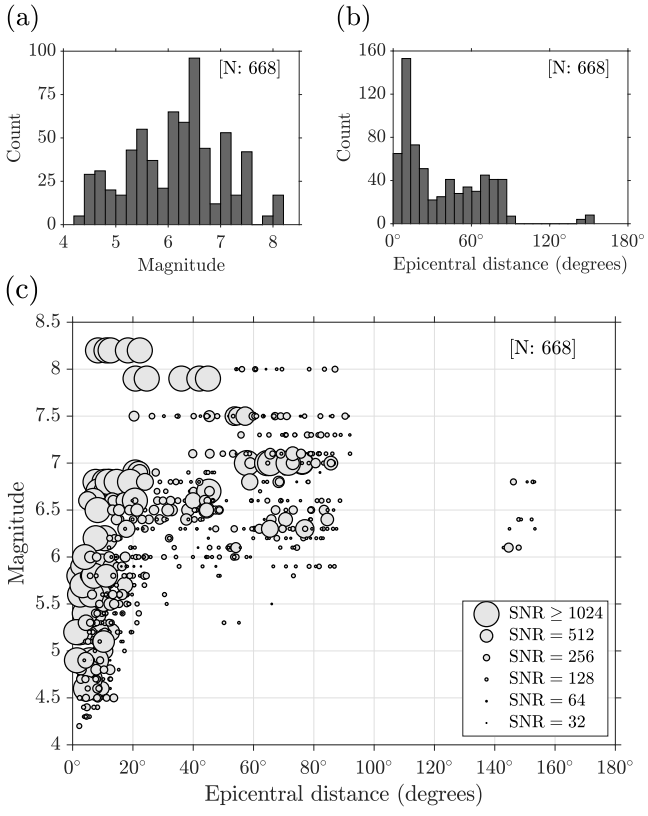


**Figure 7.** Distributions of earthquake magnitudes, epicentral distances, and signal-to-noise ratios (SNR) considering the entire data set across all 16 Princeton-operated MERMAIDs. In total, 668 MERMAID seismograms were identified to contain at least one phase arrival associated with one of 284 unique earthquakes. (a) The distribution of earthquake magnitudes has its minimum at *M*4.2, its maximum at *M*8.2, and its mean at *M*6.1. (b) The distribution of earthquake epicentral distances has a roughly uniform distribution for epicentral distances out to around 90°, except for an obvious peak around 10°, which largely corresponds to light (*M*4-4.9) and frequent earthquakes near Fiji that are sampled by the most proximal floats, mainly MERMAID P008. (c) A scatter plot of the data in (a) and (b), where the marker sizes represent the SNRs of individual arrivals. As expected, the highest-SNR records are associated with the largest and/or nearest earthquakes. Further, we find that for this data set a lower-detection threshold hovers just above *M*6 near 160°, as proven by MERMAID's identification of core phases (see Section 8.4). Note that the linear features in (c), for example, the horizontal string of points around *M*7.5 that extends from roughly 20–100°, are due to the fact that often more than one MERMAID identifies the same earthquake, leading to multiple detections of a the same event at various epicentral distances.

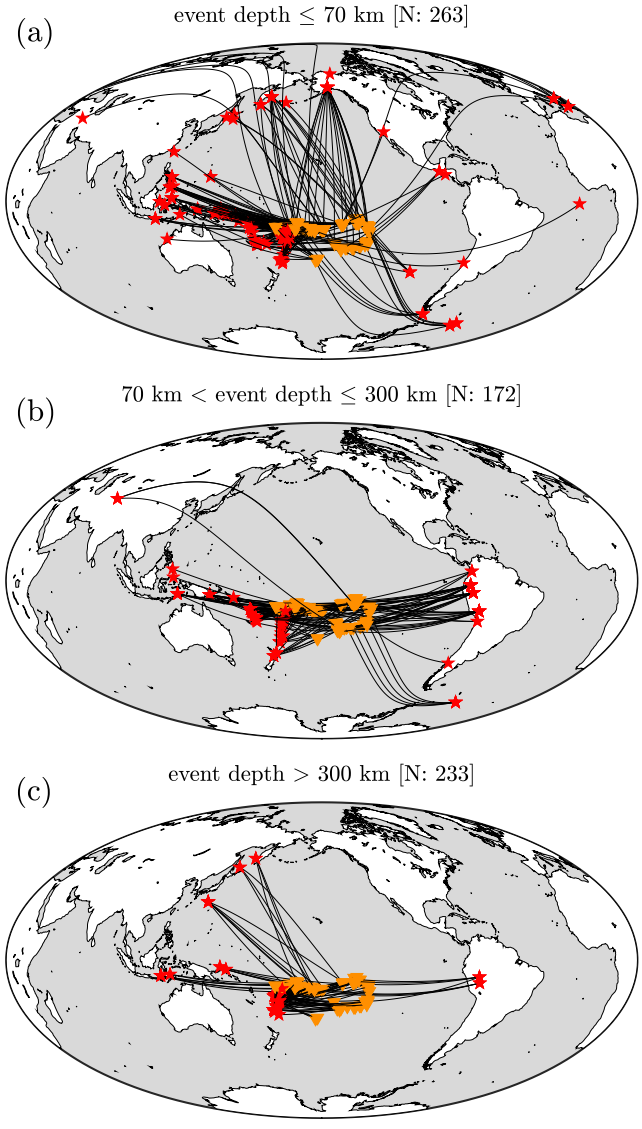


**Figure 8.** Global source-receiver ray paths considering the entire data set across all 16 Princeton MERMAIDs, separated by event depth (from top to bottom): shallow-, intermediate-, and deep-focus. In each panel, the great-circle path (black curves) connects the earthquake location (red asterisks) with the interpolated location of MERMAID at the time of recording (yellow upside-down triangles). Each map is centered on Tahiti, French Polynesia, the approximate center of the SPPIM deployment. The geographic distribution of earthquake locations plotted here shows that MERMAID preferentially records subduction-zone earthquakes in the Pacific Rim, which make sense given that the majority of global earthquakes occur along this so-called "Ring of Fire.".

MERMAID. Fig. 8 plots the ray paths of those earthquakes, connecting them to the locations of the MERMAIDs recording them, binned by event depth. In all, 668 MERMAID seismograms were identified as containing at least one phase arrival associated with one of 284 unique earthquakes.

Fig. 7(a) shows that MERMAID sampled a fairly large range of earthquake magnitudes. The smallest earthquake, a $m_b$ 4.2 at 97.8 km depth in Tonga Islands, was recorded by P008 at an epicentral distance of 2.2°. The largest event, a $M_w$ 8.2 at 600.0 km depth in the Fiji Islands Region was recorded by five out of our 16 MERMAIDs(event details from the NEIC PDE Bulletin. The specific number of MERMAIDs which reported specific earthquakes, broken down by magnitude, is discussed next in Section 6.2.

Fig. 7(b) is a histogram of those same earthquakes but now binned in terms of their epicentral distances. We see fairly consistent sampling at a variety of epicentral distances, implying MERMAID samples tomographically useful data at the global scale, including phases which have transited the core of the Earth. Those arrivals are discussed later in Section 8.4.

Finally, Fig. 7(c) plots the SNR of the first-arriving phase for every earthquake, represented by the size of the marker, as a func-

**Table 1.** The seismic catalog of the 16 Princeton MERMAIDs, complete to end of 2019.

| MERMAID | Deployment | # Wks. | # Seis. | # ID | % ID | $\frac{\#\text{ Seis.}}{\text{yr}}$ | $\frac{\#\text{ ID}}{\text{yr}}$ |
|---|---|---|---|---|---|---|---|
| P008: | 05-Aug-2018 | 73.3 | 251 | 184 | 73.3% | 179 | 131 |
| P009: | 06-Aug-2018 | 73.2 | 130 | 94 | 72.3% | 93 | 67 |
| P010: | 07-Aug-2018 | 73.1 | 125 | 85 | 68.0% | 89 | 61 |
| P011: | 09-Aug-2018 | 72.8 | 73 | 50 | 68.5% | 52 | 36 |
| P012: | 10-Aug-2018 | 72.6 | 245 | 45 | 18.4% | 176 | 32 |
| P013: | 31-Aug-2018 | 69.6 | 215 | 28 | 13.0% | 161 | 21 |
| P016: | 03-Sep-2018 | 69.2 | 48 | 26 | 54.2% | 36 | 20 |
| P017: | 04-Sep-2018 | 69.1 | 33 | 22 | 66.7% | 25 | 17 |
| P018: | 05-Sep-2018 | 68.9 | 22 | 19 | 86.4% | 17 | 14 |
| P019: | 06-Sep-2018 | 68.7 | 20 | 19 | 95.0% | 15 | 14 |
| P020: | 08-Sep-2018 | 68.5 | 89 | 13 | 14.6% | 68 | 10 |
| P021: | 09-Sep-2018 | 68.3 | 15 | 15 | 100.0% | 11 | 11 |
| P022: | 10-Sep-2018 | 68.2 | 12 | 12 | 100.0% | 9 | 9 |
| P023: | 13-Sep-2018 | 67.8 | 33 | 26 | 78.8% | 25 | 20 |
| P024: | 13-Sep-2018 | 67.8 | 18 | 18 | 100.0% | 14 | 14 |
| P025: | 14-Sep-2018 | 67.6 | 16 | 12 | 75.0% | 12 | 9 |
| Total: | | 1118.9 | 1345 | 668 | 49.7% | 983 | 486 |
| Mean: | 29-Aug-2018 | 69.9 | 84 | 42 | 49.7% | 61 | 30 |

tion of magnitude and epicentral distance. The SNRs plotted here differ slightly from those quoted in the legends of the subspace projections of Fig. 6 (they are not multiscale but rather only within a 1–5 Hz band, and they are not computed considering the entire seismogram but rather over a 30 s window centered on the theoretical arrival time of the first-arriving phase) and their derivation is discussed in detail in Section 7, but the basic idea that they express the ratio of the variances of the seismogram after and before the AIC-based arrival time pick still rings true. Fig. 7(c) is the first detectability curve available for the third-generation MERMAID—to be compared to the first-generation results shown by Simons et al. (2009) (their fig. 8). Here we see trends common to all seismic instruments: small events are preferentially recorded at short epicentral distances, before geometrical spreading and attenuation sap them of their energy, while larger events (greater than $M6$, it seems, in the case of MERMAID) may be recorded globally.

Fig. 8 places the earthquake data of Fig. 7 into their spatial context by plotting the ray paths between the earthquake and MERMAID locations at the time of recording (see Section 4.1). The ray paths are binned by event depth from top to bottom as shallow-focus (Fig. 8a; less than 70 km) intermediate-focus (Fig. 8b; between 70 km and 300 km), and deep-focus (Fig. 8c; greater than 300 km) earthquakes. Listed above each map in Fig. 8 is the total number of unique events recorded within those depth ranges. We find that MERMAID records shallow events most often, with 263 unique reports, though the counts at the other depths are overall similar, proving that MERMAID recorded earthquakes originating at depths ranging from the shallow crust to deep within subducting slabs. The shallowest earthquake in the catalog had its hypocenter at 2.2 km, under Northern Alaska, and the deepest ruptured at a depth of 652.4 km in the Fiji Islands Region. Fig. 8 also shows that MERMAID primarily recorded subduction-zone earthquakes occurring along the Pacific Rim, the so-called "Ring of Fire," the nearly continuous chain of volcanoes fed by subducting oceanic crust that encircles the Pacific Ocean from New Zealand to Chile (Rinard Hinga 2015). This is unsurprising given the location of SPPIM, roughly in the center of the Ring of Fire, and the fact that approximately 90% of annual global seismicity occurs in this most active of regions.

Figs 7 and 8 plot compiled data considering all 16 floats in the Princeton-operated fleet. As combined, these numbers mask the variability in the rate of seismicity recorded by individual floats. In what follows we parse the catalog by specific float numbers to capture the idiosyncrasies of each.

### 6.2 *Catalog summary: by the numbers*

Table 1 is a breakdown of the rate of return of seismograms per MERMAID. The first column lists the MERMAID serial numbers, the second their deployment dates, and the third the total duration, in weeks, over which each MERMAID was active. The fourth and fifth columns list the total number of seismograms returned, and the subset of those identified, respectively, and the sixth column quotes the percentage of the latter. The seventh column lists the average number of seismograms returned per full year of activity, and the eighth column lists the same statistic pertaining to the identified seismograms only. The penultimate row totals the columns, while the ultimate row lists their averages. Columns four, five, seven, and eight (corresponding to a specific number of MERMAID seismograms) are rounded to the nearest integer. As such, some values that are reportedly sums or multiples of other table entries may not be entirely self consistent due to rounding. Further, the sums and means reported in the final two rows are rounded only after performing those operations on the unrounded data in each column, meaning that the integer sum or mean of a specific column may not equal the reported value (e.g., the penultimate row, seventh column, which equals 982 if summed from the integers).

Let us first take a bird's-eye view of the data presented in Table 1 before teasing apart the statistics of the rate of return of individual MERMAIDs. From the penultimate row of Table 1 we see that

our 16 MERMAIDs enjoyed a total of 1118.9 weeks (21.4 years) of deployment thus far, over which time they autonomously recorded and transmitted 1345 seismograms from the South Pacific. Of those, 668 were positively identified with corresponding events in global catalogs available at the time using the methodology and software described in Section 5. This means that roughly half the seismograms over this time period were identified. The others represent myriad diverse signals corresponding to small and/or local events that were missed by the global seismic networks (i.e., not recorded by any other seismic station on Earth, see Section 8.5), oceanic *T* waves from unidentified sources, as well as a substantial number of what we suspect to be instrument glitches, which almost exclusively affected MERMAIDs P012, P013, and P020. An estimated dozen data files from P025 remain to be analyzed as of the time of this writing.

To emphasize a previous point: the MERMAID catalog contains many seismograms which are unidentified by the standards upheld here, but which do in fact record earthquakes that otherwise went undetected by the global seismic network—not every unidentified event is just noise. By summing column seven, the number of MERMAID seismograms divided by number of years that MERMAID was deployed, we find that we maintained a return rate of 983 seismograms per year of deployment. Lastly, by applying the historical percentage of identifications as a ratio of total seismograms from column six, we find that our 16 MERMAIDs averaged 486 identifications per year.

These data are further distilled in the last row of Table 1, where we list the rate of the return of an "average" MERMAID in our fleet. There we quote the arithmetic means of the columns, i.e., not weighted by the length of time that any individual MERMAID was deployed. Ergo, the final value in this row is the number of identified seismograms one may expect to receive from any MERMAID in any given year. Of course, our sample size of 16 is small, and limited in time and space (on average each MERMAID was deployed for around 1.3 years in a very specific part of the world), but this number is the first step towards defining the expected long-term output of an "average" MERMAID. The final value in this row is perhaps most relevant for future MERMAID deployments: we find that on average each instrument returned 30 identified seismograms per year. With a projected lifespan of five years according to the manufacturer, we thus expect a return of approximately 150 identified seismograms over the lifetime of each MERMAID.

However, and perhaps not unexpectedly, the values in the final column which contribute to this mean are broadly distributed, ranging from a maximum of 131 returned by P008, to a minimum of 9 returned by both P022 and P025. This spread is not due to implicit differences in the floats—indeed they all are identical both in manufacturing and software, and the programmable parameters (e.g., parking depth, detection criteria thresholds, etc.) were left unchanged for the duration of the deployments. Rather, this variance is most likely due to the geographic distribution of MERMAIDs.

MERMAID P008, the busiest of the group, returned so many identifiable seismograms because it cruised the oceanic region between Fiji and Samoa, near enough to the former (and drifting closer—see Fig. 4) to record many seismograms matched to light and moderate earthquakes whose energy never reached the more distant MERMAIDs in the open ocean.

Other variables influencing the rate of return of individual MERMAIDs, apart from simple source-receiver distance considerations, are the local oceanic and bathymetric environments. We hypothesize that most notable among these are ocean storms because mid-column noise has been shown to correlate strongly with wind speed (McCreery & Duennebier 1993; Nichols & Bradley 2016). Additionally, the SNRs of signals received by MERMAID are mediated by factors that do not impact common terrestrial stations; of course, like an ordinary terrestrial station the noise is time-variable, but perhaps more importantly, the impedance along the ray path between a repeating earthquake and MERMAID is also time-variable, in contrast to terrestrial stations that do not drift spatially. As MERMAID drifts it may find itself over oceanic regions with varying sedimentary cover, attenuating or amplifying incident *P*-wave energy, resulting in weaker or stronger acoustic conversion in the water column (Ewing et al. 1957; Stephen 1988). Multiple additional factors such as the water depth underlying the float (Lewis & Dorman 1998; Weatherall et al. 2015), nearby seamounts and other kinds of rough-bottom topography (Dougherty & Stephen 1991), the width and depth of the SOund Fixing and Ranging (SOFAR) channel (Munk 1974) over the $\sim 20^{\circ}$ and across the seasons covered by the SPPIM array, and other, unstudied and yet unknown factors may also all play a role in the conversion of energy (Tolstoy & Ewing 1950; Okal 2008) and in determining the local ambient noise field (Gualtieri et al. 2019).

We cannot yet separate the various factors that contributed most to the large variance in the rate of return of individual MERMAIDs after correcting for distance and magnitude considerations. No modeling of the true nature of acoustic conversions under our floats has been performed, indeed even the bathymetry is not well constrained in some areas of the SPPIM array, nor did we correlate wave or storm records with our seismic data (likely the main driver of time-variable background noise levels, see, e.g. Webb & Cox 1986; Babcock et al. 1994; Gualtieri et al. 2013; Farra et al. 2016). It is an interesting question, though beyond the scope of this study, to probe whether the MERMAIDs that sent the least data spent the most time in the noisiest regions stalled over areas of the seafloor with inefficient seismic-acoustic coupling, were muted by some other unidentified disturbance, or some combination of all of these factors. This is the target of future work that will be aided by simulation of seismic-acoustic conversions into realistic ocean layers at MERMAID's (relatively high) sampling frequency (e.g. Fernando et al. 2020).

### 6.3 *Catalog completeness and statistics*

We now move to comparing our seismic catalog with other global catalogs available at the time. How "complete" is our catalog compared to those others? Conversely, how many global earthquakes did MERMAID miss? No catalog can include all earthquakes of all magnitudes, globally (Kagan 2003), and in our own Section 8.5 we show an example of an earthquake in the MERMAID catalog that was not found in the global bulletin, but for the purpose of this section we do take the number of events recorded in global seismic catalogs to be the true population size against which we will derive completeness statistics.

Fig. 9 plots the MERMAID seismic catalog, both by the rate of

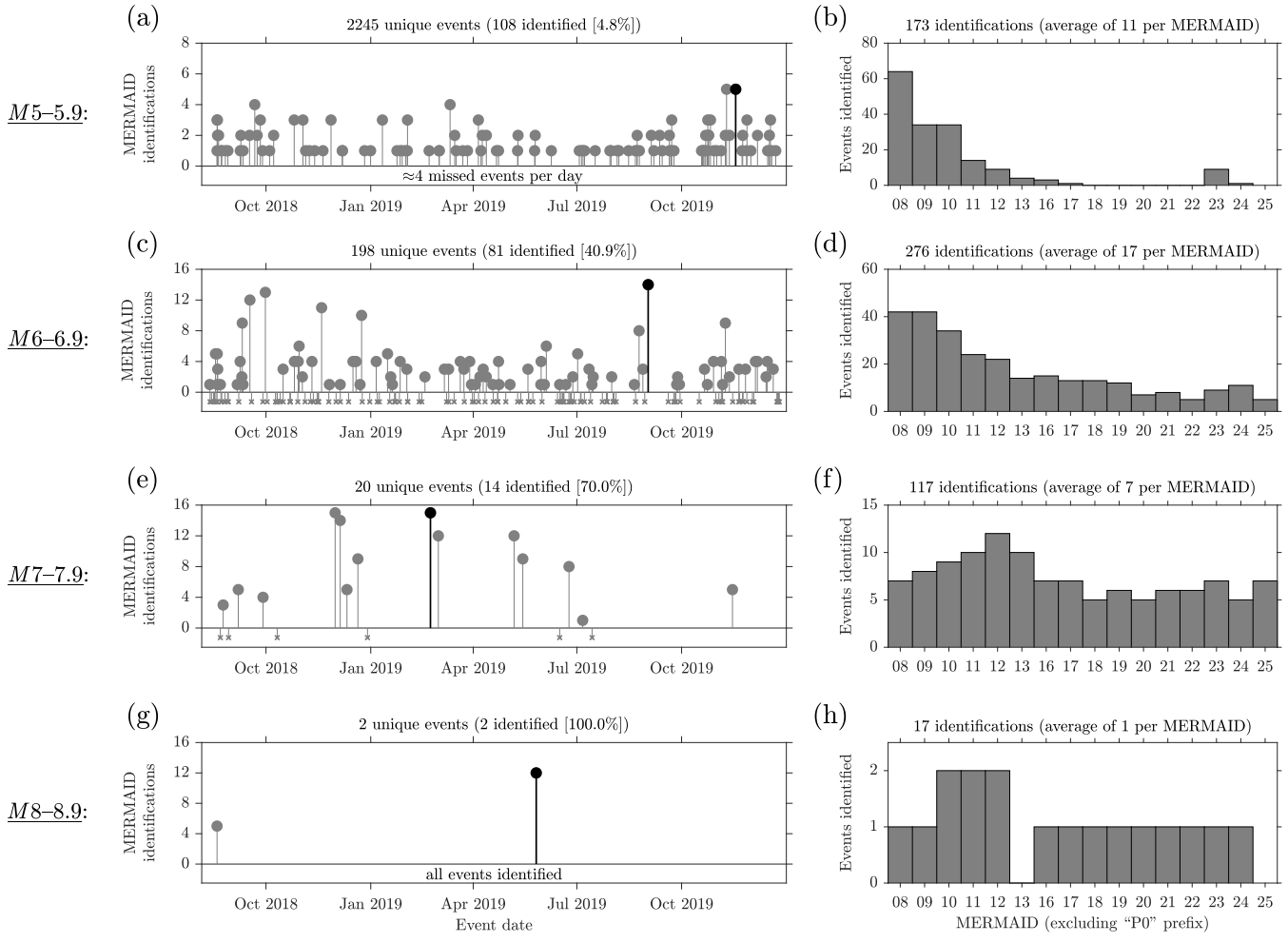


**Figure 9.** The statistics of identified seismic events recorded by MERMAID between 5 August 2018 and 31 December 2019 broken down by magnitude. In each of the panels (a), (c), (e), and (g), a single event is bolded in black—those correspond to the earthquakes which resulted in the most identifications in that magnitude range, shown in Figs 5(a–d), respectively. The stem plots in the left column plot against time the number of MERMAIDs positively identifying an event reported in the NEIC PDE catalog, with those events missed (0 MERMAIDs reporting) marked as crosses below the zero line for clarity, excepting the first (panel (a); moderate earthquakes), which tallied so many misses that its average is simply reported there to avoid visual clutter. Listed above each plot is the total number of unique events in the catalog in that magnitude range over the time period considered (because P008 was the first to be deployed this number corresponds to the first row, second column of Tables 3–6), and in parentheses (and in brackets) the number (and that percentage) of those events positively identified by at least one MERMAID. The histograms in the right column parse the total number of events identified over the deployment thus far, and report the frequency of identifications per float within each magnitude unit. Listed above each histogram is the total number of identifications, considering all 16 MERMAIDs, within that magnitude range over the time period considered (penultimate row, third column in Tables 3–6), and in parentheses that number averaged per MERMAID (ultimate row, third column in Tables 3–6).

return considering the entire fleet, and in sum considering each float individually. It further breaks these numbers down by magnitude, ranging from $M5$ in Figs 9(a and b) through $M8$ in Figs 9(g and h). The stem plots in the left column (Fig. 9a, c, e, and g) show the number of MERMAIDs reporting each positively identified earthquake as a function of time, beginning from the first deployment of P008 on 5 August 2018 through the end of 2019. The histograms in the right column (Fig. 9b, d, f, and h) aggregate these data over time, but separate them by float, to identify which floats reported the most earthquakes within a specific magnitude range.

To get at the question of completeness of our catalog versus other global seismic catalogs available at the time, in the stem plots we also represent missed events, not reported by any MERMAID, as crosses placed below the zero line for clarity. For example, Fig. 9(e), corresponding to all $M7$ earthquakes that occurred globally while MERMAID was deployed, shows that six earthquakes went unreported by the entire Princeton fleet. Conversely, Fig. 9(g) shows that no events were missed in the magnitude range $M8+$. So many $M5$–5.9 events went undetected that rather than plotting each of them in Fig. 9(a), the mean miss-rate (around 4 events per day) is reported below the zero line. Note the different scaling of the ordinate axes in Fig. 9, which highlights the fact that the rate of return of identified earthquakes correlates strongly with magnitude. Listed above each stem plot is the total number of unique global events in that magnitude range over the time period considered, and in parentheses the number, also as a fraction in per cent, which were positively identified by at least a single MERMAID. Finally, in each of the stem plots one event is highlighted in black.

These are the events reported by the largest number of MERMAIDs within each magnitude range and previously rendered in the record sections of Fig. 5.

The histograms in the right column of Fig. 9 parse the cumulative return of each individual float. Figs 9(b) and 9(d) ($M5$–5.9 and $M6$–6.9, respectively) visualize the observation of Table 1 that P008 outpaced all the other floats in terms of reporting identifiable earthquakes, which we attribute to its geographic proximity to Fiji and Tonga, as mentioned in Section 6.2. Listed above the histograms is the total number of identified events reported by any MERMAID in the fleet, and in parentheses the average over all 16 instruments. The complementary distribution for $M4$–4.9 earthquakes is not shown. Most of the light events in that category were missed, but we do note that, of the 85 total events reported (of which 79 were unique identifications), fully 70 were reported by P008.

We now summarize the statistics presented in Fig. 9 for individual magnitudes from $M4$ (not shown) through $M8$, for the time period from 5 August 2018 through the end of 2019. Note that the following statistics, e.g., the average number of identified events per MERMAID, are not rounded as they were in Fig. 9.

In the magnitude range $M4$–4.9 there were 14535 unique global events, of which 79 (0.5%) were positively identified by at least one of our 16 MERMAIDs. If an event was identified, on average 1.1 MERMAIDs reported that unique event. In total, 85 event identifications were reported by 16 MERMAIDs, meaning that on average each MERMAID reported 5.3 unique events.

For the magnitude range $M5$–5.9, there were 2245 unique global events, of which 108 (4.8%) positively identified by at least one MERMAID. If an event was identified, there were on average 1.6 MERMAIDs reporting that unique event. In total, 173 event identifications were reported by 16 MERMAIDs, and on average each MERMAID reported 10.8 unique events.

The magnitude range $M6$–6.9 comprised 198 unique global events, 81 (40.9%) of which were positively identified by at least one MERMAID. If an event was identified, on average 3.4 MERMAIDs reported it. In total, 276 event identifications were reported, for an average of 17.2 unique events reported per MERMAID.

Magnitude range $M7$–7.9 counted 20 unique events, of which 14 (70.0%) were positively identified by at least one of our instruments. If an event was identified, there were on average 8.4 MERMAID reports of it. In total, 117 event identifications were reported, or on average 7.3 unique events per MERMAID.

Finally, in magnitude range $M8$–8.9, there were precisely two events, both positively identified by at least one MERMAID in our fleet, with an average 8.5 MERMAIDs reporting each. In total, 17 event identifications were reported by 16 MERMAIDs, meaning that on average each MERMAID reported 1.1 unique events.

There were no magnitude 9 events during our study period.

We end this section by reiterating that these statistics are computed against the NEIC PDE catalog of global events, which itself is incomplete. There exists a complementary set of uncataloged events that remain undetected by the current global seismic network. MERMAID records some of those events (see Fig. 17). The analysis of those records is the target of future work, but we can report some statistics here: there remain 244 records after the removal of presumed instrument glitches from the list of unidentified (not matched to a cataloged event) MERMAID seismograms. Assuming that every one of those corresponds to an actual event detection by MERMAID we are left with an upper-bound estimate of an average of 15.2 additional uncataloged earthquakes (not necessarily unique) detected by every MERMAID during the SPPIM deployment, or around 1 additional uncataloged earthquake detected by every MERMAID each month.

**Table 2.** Global $M4$–4.9 earthquakes, missed or reported by our MERMAIDs.

| MER. | # EQ | # ID | % ID | $\frac{\#\,\text{ID}}{\text{yr}}$ | $\frac{\mathbb{E}[\#\,\text{ID}]}{5\text{yr}}$ | $\frac{\mathbb{E}[\#\,\text{ID}]}{\overline{\text{yr}}}$ | $\frac{\mathbb{E}[\#\,\text{ID}]}{5\overline{\text{yr}}}$ |
|---|---|---|---|---|---|---|---|
| P008: | 14535 | 70 | 0.5% | 50 | 249 | 59 | 293 |
| P009: | 14496 | 9 | 0.1% | 6 | 32 | 8 | 38 |
| P010: | 14475 | 6 | 0.0% | 4 | 21 | 5 | 25 |
| P011: | 14420 | 0 | 0.0% | 0 | 0 | 0 | 0 |
| P012: | 14379 | 0 | 0.0% | 0 | 0 | 0 | 0 |
| P013: | 13559 | 0 | 0.0% | 0 | 0 | 0 | 0 |
| P016: | 13489 | 0 | 0.0% | 0 | 0 | 0 | 0 |
| P017: | 13464 | 0 | 0.0% | 0 | 0 | 0 | 0 |
| P018: | 13430 | 0 | 0.0% | 0 | 0 | 0 | 0 |
| P019: | 13371 | 0 | 0.0% | 0 | 0 | 0 | 0 |
| P020: | 13315 | 0 | 0.0% | 0 | 0 | 0 | 0 |
| P021: | 13256 | 0 | 0.0% | 0 | 0 | 0 | 0 |
| P022: | 13223 | 0 | 0.0% | 0 | 0 | 0 | 0 |
| P023: | 13151 | 0 | 0.0% | 0 | 0 | 0 | 0 |
| P024: | 13146 | 0 | 0.0% | 0 | 0 | 0 | 0 |
| P025: | 13115 | 0 | 0.0% | 0 | 0 | 0 | 0 |
| Total: | 218824 | 85 | 0.0% | 60 | 302 | 71 | 356 |
| Mean: | 13677 | 5 | 0.0% | 4 | 19 | 4 | 22 |

### 6.4 *Estimating the final size of the MERMAID catalog*

With Table 1 we found that, between deployment in late 2018 and the end of 2019, each MERMAID in our fleet returned an average of 42 identified seismograms, or, normalizing for the amount of time each was deployed, about 30 per year. With Fig. 9 we saw how those 42 identifications were distributed across $M5+$ earthquakes. In this section we extrapolate those historical data to estimate the final size of the complete MERMAID catalog. We will use an anticipated five-year lifespan of MERMAID to make these estimates. Similar to some values in Table 1, the numbers reported in columns 5 through 8 of the tables discussed next are rounded to the nearest integer only after performing the relevant operations, leading to the same phenomenon that some entries that are reportedly sums or multiples of other entries may seem inconsistent (e.g., rows 1 and 2, column 6, of Table 4).

Tables 2–6 break down the rate of return of identified events per magnitude $M4$ through $M8$ for each float, and also use these numbers to project how many identified seismograms within those magnitude ranges each float is likely to return in its lifetime. As in Table 1, the first column in Table 2–6 lists the MERMAID serial number. The second quotes the total number of earthquakes that occurred over the complete deployment of that specific float. For example, the value in this column in the first row (P008) of Tables 3–6 is the same number quoted above the corresponding stem plots in Fig. 9. This number represents the maximum number of earthquakes that each float could have individually identified dur-

**Table 3.** Global $M$5–5.9 earthquakes, missed or reported by our MERMAIDs.

| MER. | # EQ | # ID | % ID | $\frac{\#\text{ ID}}{\text{yr}}$ | $\frac{\mathbb{E}[\#\text{ ID}]}{5\text{yr}}$ | $\frac{\mathbb{E}[\#\text{ ID}]}{\overline{\text{yr}}}$ | $\frac{\mathbb{E}[\#\text{ ID}]}{5\overline{\text{yr}}}$ |
|---|---|---|---|---|---|---|---|
| P008: | 2245 | 64 | 2.9% | 46 | 228 | 46 | 230 |
| P009: | 2242 | 34 | 1.5% | 24 | 121 | 25 | 123 |
| P010: | 2240 | 34 | 1.5% | 24 | 121 | 25 | 123 |
| P011: | 2230 | 14 | 0.6% | 10 | 50 | 10 | 51 |
| P012: | 2222 | 9 | 0.4% | 6 | 32 | 7 | 33 |
| P013: | 2096 | 4 | 0.2% | 3 | 15 | 3 | 15 |
| P016: | 2085 | 3 | 0.1% | 2 | 11 | 2 | 12 |
| P017: | 2081 | 1 | 0.0% | 1 | 4 | 1 | 4 |
| P018: | 2070 | 0 | 0.0% | 0 | 0 | 0 | 0 |
| P019: | 2051 | 0 | 0.0% | 0 | 0 | 0 | 0 |
| P020: | 2039 | 0 | 0.0% | 0 | 0 | 0 | 0 |
| P021: | 2036 | 0 | 0.0% | 0 | 0 | 0 | 0 |
| P022: | 2032 | 0 | 0.0% | 0 | 0 | 0 | 0 |
| P023: | 2019 | 9 | 0.4% | 7 | 35 | 7 | 36 |
| P024: | 2019 | 1 | 0.0% | 1 | 4 | 1 | 4 |
| P025: | 2013 | 0 | 0.0% | 0 | 0 | 0 | 0 |
| Total: | 33720 | 173 | 0.5% | 124 | 621 | 126 | 630 |
| Mean: | 2108 | 11 | 0.5% | 8 | 39 | 8 | 39 |

**Table 4.** Global $M$6–6.9 earthquakes, reported or missed by our MERMAIDs.

| MER. | # EQ | # ID | % ID | $\frac{\#\text{ ID}}{\text{yr}}$ | $\frac{\mathbb{E}[\#\text{ ID}]}{5\text{yr}}$ | $\frac{\mathbb{E}[\#\text{ ID}]}{\overline{\text{yr}}}$ | $\frac{\mathbb{E}[\#\text{ ID}]}{5\overline{\text{yr}}}$ |
|---|---|---|---|---|---|---|---|
| P008: | 198 | 42 | 21.2% | 30 | 149 | 26 | 129 |
| P009: | 198 | 42 | 21.2% | 30 | 150 | 26 | 129 |
| P010: | 198 | 34 | 17.2% | 24 | 121 | 21 | 104 |
| P011: | 198 | 24 | 12.1% | 17 | 86 | 15 | 74 |
| P012: | 198 | 22 | 11.1% | 16 | 79 | 14 | 68 |
| P013: | 181 | 14 | 7.7% | 10 | 52 | 9 | 47 |
| P016: | 181 | 15 | 8.3% | 11 | 57 | 10 | 50 |
| P017: | 181 | 13 | 7.2% | 10 | 49 | 9 | 44 |
| P018: | 181 | 13 | 7.2% | 10 | 49 | 9 | 44 |
| P019: | 180 | 12 | 6.7% | 9 | 46 | 8 | 41 |
| P020: | 178 | 7 | 3.9% | 5 | 27 | 5 | 24 |
| P021: | 178 | 8 | 4.5% | 6 | 31 | 5 | 27 |
| P022: | 176 | 5 | 2.8% | 4 | 19 | 3 | 17 |
| P023: | 175 | 9 | 5.1% | 7 | 35 | 6 | 31 |
| P024: | 175 | 11 | 6.3% | 8 | 42 | 8 | 38 |
| P025: | 175 | 5 | 2.9% | 4 | 19 | 3 | 17 |
| Total: | 2951 | 276 | 9.4% | 202 | 1011 | 177 | 885 |
| Mean: | 184 | 17 | 9.4% | 13 | 63 | 11 | 55 |

**Table 5.** Global $M$7–7.9 earthquakes, reported or missed by our MERMAIDs.

| MER. | # EQ | # ID | % ID | $\frac{\#\text{ ID}}{\text{yr}}$ | $\frac{\mathbb{E}[\#\text{ ID}]}{5\text{yr}}$ | $\frac{\mathbb{E}[\#\text{ ID}]}{\overline{\text{yr}}}$ | $\frac{\mathbb{E}[\#\text{ ID}]}{5\overline{\text{yr}}}$ |
|---|---|---|---|---|---|---|---|
| P008: | 20 | 7 | 35.0% | 5 | 25 | 5 | 23 |
| P009: | 20 | 8 | 40.0% | 6 | 29 | 5 | 26 |
| P010: | 20 | 9 | 45.0% | 6 | 32 | 6 | 30 |
| P011: | 20 | 10 | 50.0% | 7 | 36 | 7 | 33 |
| P012: | 20 | 12 | 60.0% | 9 | 43 | 8 | 40 |
| P013: | 17 | 10 | 58.8% | 7 | 37 | 8 | 39 |
| P016: | 17 | 7 | 41.2% | 5 | 26 | 5 | 27 |
| P017: | 17 | 7 | 41.2% | 5 | 26 | 5 | 27 |
| P018: | 17 | 5 | 29.4% | 4 | 19 | 4 | 19 |
| P019: | 16 | 6 | 37.5% | 5 | 23 | 5 | 25 |
| P020: | 16 | 5 | 31.2% | 4 | 19 | 4 | 21 |
| P021: | 16 | 6 | 37.5% | 5 | 23 | 5 | 25 |
| P022: | 16 | 6 | 37.5% | 5 | 23 | 5 | 25 |
| P023: | 16 | 7 | 43.8% | 5 | 27 | 6 | 29 |
| P024: | 16 | 5 | 31.2% | 4 | 19 | 4 | 21 |
| P025: | 16 | 7 | 43.8% | 5 | 27 | 6 | 29 |
| Total: | 280 | 117 | 41.8% | 87 | 435 | 88 | 438 |
| Mean: | 18 | 7 | 41.8% | 5 | 27 | 5 | 27 |

**Table 6.** Global $M$8–8.9 earthquakes, reported or missed by our MERMAIDs.

| MER. | # EQ | # ID | % ID | $\frac{\#\text{ ID}}{\text{yr}}$ | $\frac{\mathbb{E}[\#\text{ ID}]}{5\text{yr}}$ | $\frac{\mathbb{E}[\#\text{ ID}]}{\overline{\text{yr}}}$ | $\frac{\mathbb{E}[\#\text{ ID}]}{5\overline{\text{yr}}}$ |
|---|---|---|---|---|---|---|---|
| P008: | 2 | 1 | 50.0% | 1 | 4 | 0 | 2 |
| P009: | 2 | 1 | 50.0% | 1 | 4 | 0 | 2 |
| P010: | 2 | 2 | 100.0% | 1 | 7 | 1 | 5 |
| P011: | 2 | 2 | 100.0% | 1 | 7 | 1 | 5 |
| P012: | 2 | 2 | 100.0% | 1 | 7 | 1 | 5 |
| P013: | 1 | 0 | 0.0% | 0 | 0 | 0 | 0 |
| P016: | 1 | 1 | 100.0% | 1 | 4 | 1 | 5 |
| P017: | 1 | 1 | 100.0% | 1 | 4 | 1 | 5 |
| P018: | 1 | 1 | 100.0% | 1 | 4 | 1 | 5 |
| P019: | 1 | 1 | 100.0% | 1 | 4 | 1 | 5 |
| P020: | 1 | 1 | 100.0% | 1 | 4 | 1 | 5 |
| P021: | 1 | 1 | 100.0% | 1 | 4 | 1 | 5 |
| P022: | 1 | 1 | 100.0% | 1 | 4 | 1 | 5 |
| P023: | 1 | 1 | 100.0% | 1 | 4 | 1 | 5 |
| P024: | 1 | 1 | 100.0% | 1 | 4 | 1 | 5 |
| P025: | 1 | 0 | 0.0% | 0 | 0 | 0 | 0 |
| Total: | 21 | 17 | 81.0% | 13 | 63 | 12 | 61 |
| Mean: | 1 | 1 | 81.0% | 1 | 4 | 1 | 4 |

ing its deployment. The third and fourth columns list the number, and percentage, of those events that were identified. The fifth is analogous to the final column of Table 1, except here it is further parsed by magnitude, while there it was the sum across all magnitudes.

The sixth column of Tables 2–6 lists our first estimates of the expected total number of identified seismograms that any individual MERMAID may return over its projected five-year lifespan. It is simply the historical yearly rate of return of identified seismograms (the previous column), multiplied by five. For light and moderate earthquakes, especially, this method of estimation is likely sound because there are so many earthquakes within those magnitude ranges annually that the year-to-year variance in the earthquake sample size (each of which MERMAID either does or does not identify) is relatively small. Conversely, one could imagine a case where the historical rate we derived for, e.g., great earthquakes, was sampled during an anomalous year, and was thus a poor estimator of the true annual population. In that case, projections based on those values could greatly skew our estimates.

To combat the potential issue of anomalous sample sizes skewing the projections of Tables 2–6 we pulled a data set of all events cataloged by IRIS from 1985 through to the end 2014. We choose to base our updated annual seismicity rates on those dates because: 30 years of data surely provides a large enough sample

size within each magnitude to converge to the true population values; 2014 was far enough in the past to ensure that the International Seismological Centre (2015) catalog had been reviewed (Bondár & Storchak 2011) and published (it generally lags behind the PDE, the nearly instantaneous, but not necessarily most accurate, source of earthquake data from IRIS, by a few years); and 1985 was still recent enough to ensure that a robust and relatively modern seismic network was installed globally, which all but guaranteed that the resultant catalogs would be relatively complete. We found that over that 30-year span there were a total of 365378 $M4$, 48511 $M5$, 3650 $M6$, 396 $M7$, and 28 $M8$ earthquakes, resulting in an average of 12179 $M4$, 1617 $M5$, 122 $M6$, 13 $M7$, and 1 $M8$ earthquakes per year. We use the latter numbers to compute the values in the final two columns of Tables 2–6, where the overline, $\overline{\text{yr}}$, denotes an "average" year. In column seven we multiplied these average seismicity rates by the percentage of the total that each float identified (column four) to compute a second estimate of the expected total number of identified seismograms that any individual MERMAID may return in a year. In column eight we again multiplied this number by five to project the final number of earthquakes each float may be expected to identify in its lifetime.

The final two rows of Tables 2–6 summarize the data in much the same way as Table 1—the penultimate row tallies the totals of the columns, and the ultimate row reports their means. Like there, the final number in the final row carries the most meaning: it is our best guess of the total number of identified earthquakes that any given MERMAID will report within a specific magnitude range over its projected lifetime. We find these numbers to be 22 $M4$, 39 $M5$, 55 $M6$, 27 $M7$, and 4 $M8$ earthquakes, or just under 150 earthquakes in total. For a fleet of 16, this equates to nearly 2400 identified earthquakes. However, as we have seen, the variance in the rate of return among the floats is large, and some, for example P008 with its 184 identified events, have already surpassed their expected lifetime-total return.

Ultimately, we return the conclusion of Section 6.2, that it is likely the geographic location, the frequency and severity of nearby storms, and perhaps to a lesser extent the geologic seafloor setting around where MERMAID drifts, that most drives the rate of return of identified seismograms by any individual float. This point is made well in Table 2 columns one and four, where we see that P008 was privy to only 115 more $M4$ earthquakes than P011, due to their different deployment lengths, but the former identified 70 and the latter identified none.

## 7 ESTIMATING DELAY TIMES AND UNCERTAINTIES

Having exhausted our study of the ability of MERMAID to detect, or not, global earthquakes, we now move to discussing the seismograms themselves. This is the main thrust of this study; the high-precision picking of first-arriving $P$ or $p$ waves, the estimation of uncertainty about those times, and what their residuals against various velocity-model predictions may tell us about mantle structure. We shared a preview of our preferred method of phase-picking in Fig. 6 of Section 5.1. Here we elaborate slightly on our procedure, discussing specifically how we applied it in this study to accurately identify first-arrival times and quantify their uncertainties.

### 7.1 *The arrival-time pick*

We developed an automated AIC-based arrival-time estimation scheme (Simon et al. 2020) to rapidly and accurately pick seismic phase arrival times. Our procedure relies on computing the likelihood that a time-pick best partitions the seismogram into two distinct segments: noise and signal. We do so, in essence, by maximizing the SNR over all possible splits, from start to end. Simon et al. (2020) also includes two methods to assess the uncertainty of our arrival-time estimates. We use the first of those methods, Monte-Carlo resimulation and re-picking, to estimate the arrival-time uncertainties reported in this study.

We used the same picking procedure for every seismogram analyzed in this study regardless of whether it was recorded by MERMAID, a traditional seismometer, or a Raspberry Shake, with which we will be comparing and validating the MERMAID results in Section 9. First, a 60 s segment of the demeaned and detrended seismogram, centered on the theoretical phase arrival time, was isolated for inspection. Then it was multiplied by a symmetric window, flat in its 30 s interior and with a 15 s cosine taper at either end (i.e., a 60 s Tukey window with a 50% cosine taper). Next, the tapered seismogram was band-pass filtered between 1 and 5 Hz using a one-pass, four-pole Butterworth filter. Finally, our AIC-based picking scheme was run on the data within the 30 s segment where the window was unity.

### 7.2 *The travel-time residual*

We define the travel-time residual to be the time difference between our travel-time pick, $t_{\text{AIC}}$, and the theoretical travel time of the corresponding phase computed in the model of interest. Note that we are careful to refer separately to "travel times" and "arrival times" in this study; though they tag the same absolute UTC time, they are in reference to different zero times. When we say "travel time" we mean the time elapsed between the event origin time and the time of the phase arrival (either based on theory or observation); and when we use "arrival time" we are referring to the time elapsed between the start of the seismogram and the same phase-arrival time.

For all records of traditional sensors and Raspberry Shake stations on nearby islands that we will be discussing, the travel-time residual is simply

$$t_{\text{res}} = t_{\text{AIC}} - t_{\text{ak135}}, \tag{2}$$

where the relevant model is the 1-D model ak135. Computing MERMAID travel-time residuals in the same model requires adjusting for bathymetry and MERMAID cruising depth,

$$t^{\star}_{\text{res}} = t_{\text{AIC}} - t^{\star}_{\text{ak135}}, \tag{3}$$

as explained in next in Section 7.3.

We perform this simple 1-D comparison first to show that the distributions of residuals from more traditional seismic instruments and MERMAID agree well, indicating that MERMAID is returning tomographically useful data. Later we recompute residuals for MERMAID using the fully-3-D, elliptical LLNL-3DGv3 crust and mantle model of Simmons et al. (2012), defining

$$t^{\oplus}_{\text{res}} = t_{\text{AIC}} - t_{\text{LLNL}}, \tag{4}$$

to interrogate the geographic distribution of velocity perturbations in Earth's mantle as recorded by MERMAID.

### 7.3 *Adjusting for bathymetry and* MERMAID *cruising depth*

Eq. (3) required adjusting the ak135 travel-time for bathymetry, the water layer, and a submerged receiver. There, $t^{\star}_{\text{ak135}}$ is the theoretical travel time computed in the adjusted ak135 velocity model,

$$t^{\star}_{\text{ak135}} = t_{\text{ak135}} + t_{\text{adj}}, \tag{5}$$

where $t_{\text{adj}}$ is the difference between the travel times in the adjusted and standard models. Because we assume that the theoretical ray paths are identical in both models until reaching the seafloor, $t_{\text{adj}}$ equals the difference between the travel time of the converted phase from the seafloor to MERMAID and the travel time of the direct phase in a rock layer equal in thickness to the local water depth,

$$t_{\text{adj}} = \frac{z_{\text{w}} - z_{\text{MER}}}{v_{\text{w}} \cos\theta_{\text{w}}} - \frac{z_{\text{w}}}{v_{\text{r}} \cos\theta_{\text{r}}}. \tag{6}$$

In this convention $z$ is depth in m positive down below the surface, $v$ is the acoustic velocity in m/s, $\theta$ is the angle of incidence in degrees, and subscripts "w" and "r" denote those values in water and rock, respectively. Local bathymetry at the location of the recording MERMAID ($z_{\text{w}}$) is interpolated from GEBCO 2014 (Weatherall et al. 2015), and MERMAID depth at the time of trigger ($z_{\text{MER}}$) was measured via its onboard pressure sensor (the Supplemental Material details these values for every seismogram described here). The standard dive depth is 1500 m. We assume an acoustic velocity of 1500 m/s for the water layer and use 5800 m/s for rock, in keeping with the upper layer in ak135. The incidence angle of the converted phase in the water column is given by Snel's law (Nolet 2008),

$$\theta_{\text{w}} = \arcsin\left(\frac{v_{\text{w}} \sin\theta_{\text{r}}}{v_{\text{r}}}\right). \tag{7}$$

Eq. (6) yields an adjustment $t_{\text{adj}} = +0.98$ s for a *P* wave incident at 0° on the seafloor of a 4000 m deep ocean, and recorded by MERMAID at a cruising depth of 1500 m, in other words, for an "average" ocean depth and an "average" MERMAID cruising depth.

Considering MERMAID's design goal of reporting teleseismic waveforms that bottomed in the lower mantle, which are incident at small angles on the seafloor, a good rule of thumb holds that 1 s should be *added* to travel times computed in the ak135 velocity model (or, equivalently, 1 s should be *removed* from MERMAID travel-time residuals computed against ak135 as in eq. (2). The residuals reported by Simon et al. (2020) for the second-generation MERMAID data were not corrected for bathymetry or cruising depth and hence this rule should be applied to the residuals reported there.

Also note that while we have spoken generally in this section about "the" adjusted model, the specific time adjustment applied in eq. (5) is dependent on source-station geometry (via the incidence angle), ocean depth, and MERMAID cruising depth, and thus differs for every seismogram. The Supplemental Material details these 1-D travel-time adjustments, as well as the analogous 3-D adjustments to convert between ak135 and LLNL-3DGv3, which are also specific to individual seismograms.

### 7.4 *The uncertainty on the residual*

Our AIC-based picking procedure simultaneously provides uncertainty estimates associated with each arrival time. Method 1 of Simon et al. (2020), used here, leverages the statistics of the seismogram to construct synthetic sequences from which timing-error distributions are generated via Monte-Carlo resimulation. Every such "seismogram" is simply modeled as a noise segment preceding a signal segment, individually generated by an uncorrelated Gaussian distribution and concatenated at the presumed arrival time. The means and variances of the two segments are estimated from the data themselves as part of the AIC picking procedure. In practice, zero-mean noise and zero-mean signal sequences result in synthetics whose two segments differ only in variance, and which match the SNR and the picked "changepoint" of the seismogram after which they are modeled. A new AIC arrival-time is picked on each synthetic, and the signed distance between it and the AIC pick on the real seismogram (the assumed truth) is tallied over 1000 simulations to generate the error distribution. For this study we use twice the standard deviation of this distribution, $2\text{SD}_{\text{err}}$, as our standard measure of timing uncertainty, quoted in seconds.

Fig. 10 shows 12 MERMAID seismograms and their travel-time residuals and uncertainty estimates in adjusted ak135 models following the procedures just described. The rows are ordered from low- to high-uncertainty. The first three seismograms (Fig. 10a–c) are the lowest-uncertainty records in the MERMAID catalog, and the final three (Fig. 10j–l) display seismograms with picking uncertainties equal to 0.15 s. The middle rows, Fig. 10(d–f) and Fig. 10(g–i), show the seismograms for which the corresponding uncertainties straddle the 33rd and 66th percentiles between these two uncertainty bounds, respectively. Each panel of Fig. 10 plots 30 s of one MERMAID seismogram with its timing relative the theoretical travel time of the first-arriving *P* or *p* wave (dashed black vertical line at 0 s) in an adjusted ak135 velocity model (eq. 5). This is the complete segment, after tapering and filtering, which was considered for the AIC pick (solid red vertical line, with its estimated uncertainty shown as dashed red vertical lines at $\pm 2\text{SD}_{\text{err}}$ along the time axis), for which the corresponding adjusted residual is quoted above each panel (eq. 3).

For each seismogram, the portion before our arrival-time pick is considered noise and colored gray, while the portion after our pick is considered signal and colored blue. Thus, the SNRs reported here, and for the remainder of the study, are computed as in eq. (1) but we specifically consider only the 30 s windows shown in Fig. 10, and we compute the estimated variances directly from the gray and colored segments as partitioned by our AIC picks. On each seismogram we circle the maximum (absolute) amplitude of the first-arriving phase on the blue signal segment. Its value and the delay time between it and our first-arrival pick are reported in brackets outside the left ordinate and upper abscissa axis, respectively. We define the first-arriving phase window to be the segment of the seismogram starting at the arrival-time pick and ending 1.75 s later. We chose 1.75 s because it is longer than our minimum-retained phase of 1 Hz, ensuring we capture at least one complete cycle, and it is shorter than 2 s, the estimated round-trip travel time of the surface-reflected phase (the large-amplitude, opposite-polarity "ghost"). Within each panel the inset boxes (starting from the upper left and moving clockwise) list the magnitude of the corresponding event, the depth and distance of the event, the timing-uncertainty on the residual, and the SNR of the seismogram.

The seismograms in Fig. 10 span the complete set which contributed residuals data to Fig. 20(c–d), the uncertainty threshold there being 0.15 s. This quality criterion was decided upon after inspecting all seismograms in the MERMAID catalog and finding that

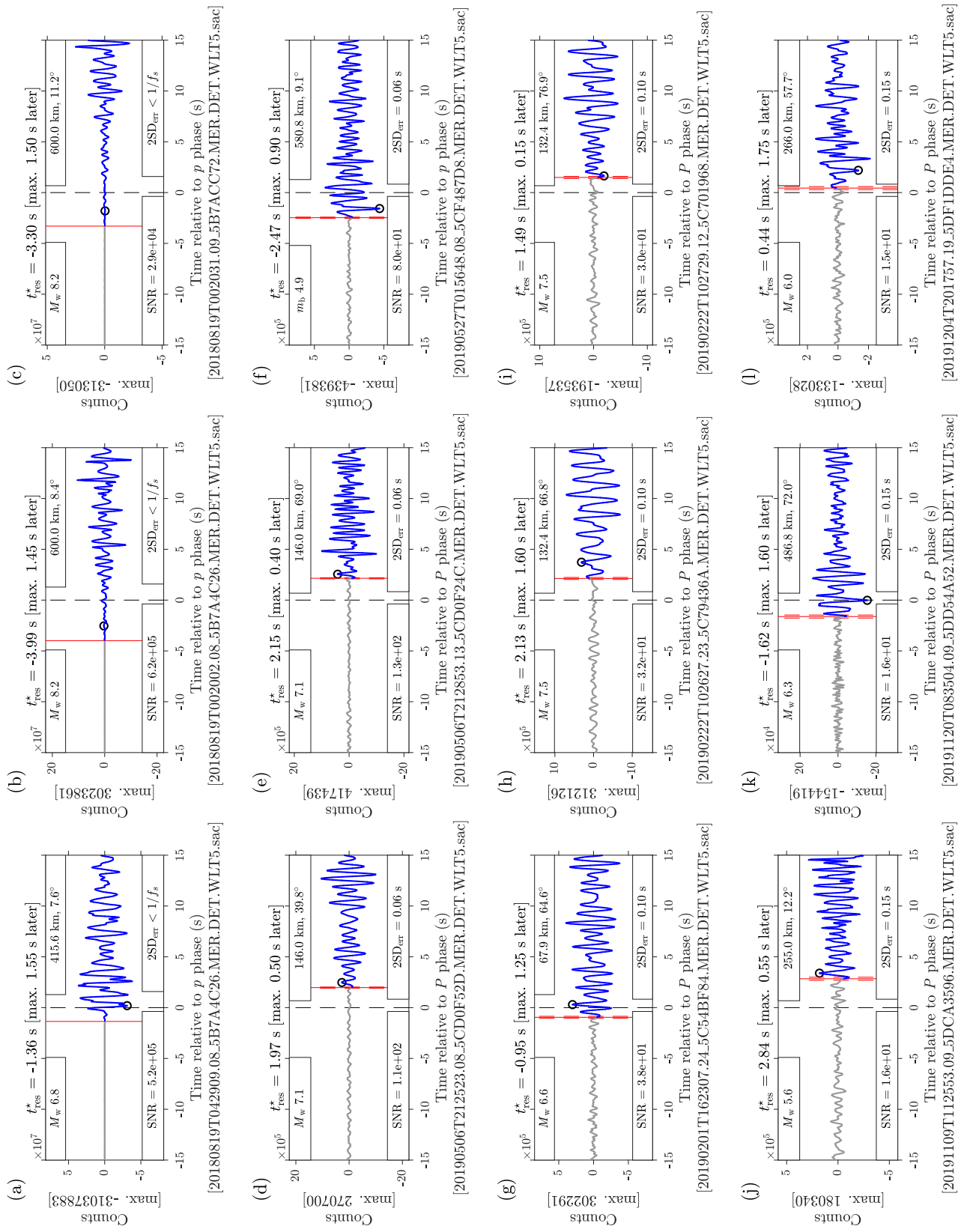


**Figure 10.** MERMAID seismograms showing detail in a 30 s window aligned on the theoretical first-arriving phase in ak135 models adjusted for bathymetry and MERMAID cruising depth. In each, the seismogram is filtered between 1 and 5 Hz and plotted in counts. The timing is relative to the theoretical travel-time of the first-arriving $p$ or $P$ wave (eq. 5, marked as a dashed vertical line at 0 s), and the solid red vertical line marks our AIC-based pick. Therefore, in these model-aligned seismograms, the red lines mark our travel-time residuals in adjusted ak135 models (eq. 3). The estimated uncertainty on our pick is shown as dashed vertical lines extending ±two-standard deviations in both directions along the time axis. We deem the segment preceding our pick to be noise and color it gray, and that which succeeds our pick to be signal and color it blue. Listed above each panel is the adjusted travel-time residual, and the delay between our pick and the time at the maximum (or minimum) amplitude of the signal. This maximum is circled on the blue signal segment and its rounded value in counts is reported within the brackets on the ordinate axis. Inset in each panel clockwise from top left is the earthquake magnitude, the earthquake depth and its distance, the two-standard deviation error estimate of our pick using Method 1 of Simon et al. (2020), and the estimated SNR of the seismogram (eq. 1).

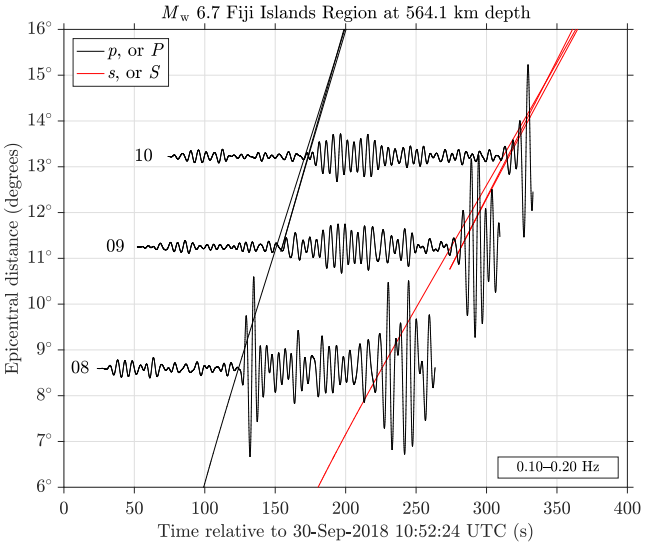


**Figure 11.** Low-frequency MERMAID seismograms showing *S*-wave arrivals from a deep event in the Fiji Islands Region. Theoretical travel times of *P* and *S* waves in the ak135 model are marked by the black and red curves, respectively.

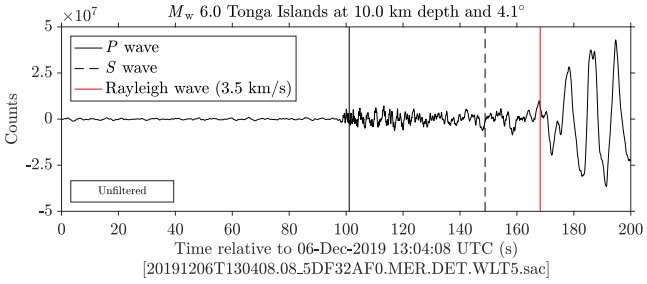


**Figure 12.** Unfiltered MERMAID seismogram from float P008 showing the arrival of surface waves from a nearby shallow event in the Tonga Islands. Black vertical lines mark the theoretical arrival times of the first-arriving *P* (solid) and *S* (dashed) waves, and a red vertical line marks the theoretical arrival time of a surface wave with a horizontal phase velocity of 3.5 km/s, calculated for the ak135 reference model.

the trained eye began to distrust picks with larger uncertainties. For reference, the highest uncertainty among all first-arriving *P* waves in the catalog is 1.13 s. However, it is important to remember that the uncertainties quoted here correspond to a pick made in a single frequency band (1–5 Hz) in which seismic energy for any given event may be emergent or missing. In contrast, the picking procedure detailed by Simon et al. (2020) and shown in Fig. 6 inspects the full bandwidth of the MERMAID seismogram via multiscale wavelet decomposition, and treats every wavelet scale (in practice, scales are roughly analogous to non-overlapping frequency bands) separately for arrival-time estimation, the consideration of all being necessary to the informed matching of seismograms to events.

## 8 BEYOND *P* WAVES: *S*, *T*, SURFACE, AND CORE

Before returning to the main aim of this study, the high-precision picking of *P* waves in the MERMAID catalog for future tomographic inversions, we will take a slight detour to review some of the other, unexpected signals that MERMAID has recorded. As mentioned in Section 2, the MERMAID algorithm was written with the express purpose of triggering on tomographic-quality mantle *P* waves. However, MERMAID has, on occasion, sent us other phases which extend its utility beyond *P*-wave tomography, including *S* waves, surface waves, *T* waves, and even inner- and outer-core phases.

### 8.1 *S waves*

Fig. 11 is a record section for a large ($M_W$ 6.7) and deep (564.1 km) earthquake in the Fiji Islands Region. It is similar to Fig. 5, though here the seismograms are filtered between a much lower frequency band of 0.1 to 0.2 Hz, and the seismograms have not been tapered to retain the visibility of the secondary arrivals near the end of the records. Within this band we clearly see the arrival of both *P* and *S* waves, whose theoretical travel times are marked by black and red curves, respectively. Like in Fig. 5 (and for all other record sections in this study: Figs 11, 15, and 18), these travel-time curves are computed in the ak135 velocity model and they are not adjusted for bathymetry or MERMAID cruising depth because adjustments (eq. 6) uniquely apply to specific MERMAID arrivals and not to entire travel-time curves. Therefore, application of the rule of thumb described in Section 7.3 would delay the phase branches by 1 s.

These are the first published examples of *S* waves recorded by MERMAID. Shear waves cannot travel though water, therefore, what is actually being recorded here are the signals of mantle shear waves that underwent seismic-acoustic (*S* to *p*) conversion at the seafloor.

### 8.2 *Surface Waves*

Fig. 12 shows a clear surface-wave detection in an unfiltered MERMAID seismogram, recorded by float P008. This is the first example ever published of a surface wave recorded by MERMAID. Its dominant period appears to be around 10 s, the longest period resolvable by MERMAID. We label it a Rayleigh wave, rather than a Love wave, because the former produces displacements normal to the seafloor, as is required to generate the hydroacoustic pressure signals that MERMAID records. Note that, depending its on wavelength, a *P-SV* polarized wave traveling along a fluid-solid interface could also be called a Scholte wave (Kugler et al. 2007). The corresponding event was a large ($M_W$ 6.0), shallow (10 km), and proximal (4.1°) earthquake in the Tonga Islands. Plotted as vertical lines from left to right are the theoretical arrival times as computed in ak135 of the first-arriving *P* and *S* waves, as black solid and dashed lines, respectively, and as a red solid line, the theoretical arrival time of a surface wave with a speed of 3.5 km/s. We see that the largest-amplitude signal corresponds to the relatively low-frequency phase which arrives around the theoretical arrival time of the surface wave. We do not see a large arrival associated with the earlier *S* wave, as we did in Fig. 11, in this unfiltered seismogram.

Surface-wave amplitudes decay with distance more slowly than body wave amplitudes. Given that the amplitude of the surface wave is so large in this example we would expect to find other large-amplitude surface waves in the MERMAID data set, if we looked in

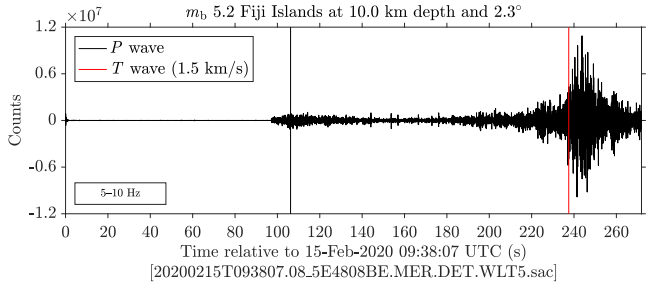


**Figure 13.** High-frequency MERMAID seismogram showing the arrival of a *T* wave from a local and shallow earthquake in the Fiji Islands. Theoretical arrival times in ak135 for the first-arriving *P* wave, and a *T* wave with a horizontal phase velocity of 1.5 km/s (the speed of sound in water), are marked by black and red vertical lines, respectively.

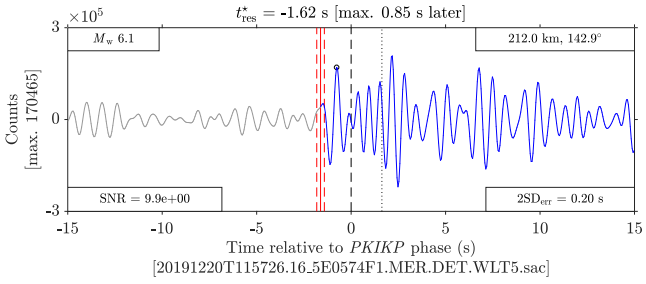


**Figure 14.** MERMAID seismogram filtered between 1 and 2 Hz and annotated like those in in Fig. 10, showing an inner-core *PKIKP* phase arrival corresponding to an earthquake in the Hindu Kush Region of Afghanistan. The timing is relative to the theoretical travel time of *PKIKP* in an adjusted ak135 model (eq. 5), and the dotted vertical line at 3.25 s marks the theoretical offset of the travel time of the secondary inner-core *PKiKP* reflected phase, which we do not see in this seismogram.

the right time and place. In this case, MERMAID P008 was drifting near enough to the source to record these surface waves (which must arrive within ≈100 s of the *P* wave to be included in the default-length 200–250 s seismogram). The two-way Iridium communication system built into every float allows us to request from MERMAID's one-year data buffer any similar segments of interest that might contain surface waves.

### 8.3 *T waves*

Tertiary (*T*) waves are acoustic waves that propagate within the SOFAR channel, a minimum-velocity waveguide that traps sound from a variety of sources, including earthquakes, and permits its efficient propagation across entire ocean basins (see Okal 2008 for historical perspective and a discussion on *T*-wave generation). In the record *T* waves are typically emergent rather than impulsive. This is due to a variety of factors including multipathing in the solid earth before reaching the seafloor, and seafloor geometries that result in the inefficient transfer of (sub)vertically-traveling seismic energy into horizontally-propagating *T*-wave energy without multiple surface-seafloor reverberations at the conversion site (e.g. Talandier & Okal 1998, 2001). These, and potentially other complex scattering effects (Fox et al. 1993; Park et al. 2001), tend to defocus the wavetrain and produce the characteristic spindle-like shape of *T* waves. In MERMAID seismograms *T* waves are most easily distinguishable from the coda that follows *P* arrivals by a higher frequency-content and tapered envelope.

Fig. 13 shows an example of a *T*-wave arrival in a high-frequency MERMAID seismogram. Here, the data are filtered between 5 and 10 Hz and the theoretical arrival time of the first-arriving *P* wave is marked around 100 seconds with a black vertical line. The corresponding event was a local (2.3°) and shallow (10 km) $m_b$ 5.2 earthquake in the Fiji Islands. We speculate that the secondary arrival that has its maximum amplitude around 150 seconds later is a *T* wave, and mark in red the theoretical arrival time of phase with a with a velocity of 1.5 km/s. Various observations make us confident this is in fact a *T* wave: (1) it is of very high frequency; (2) its amplitude is large compared to the *P*-wave arrival, perhaps due in part to the proximity of this event (see also Slack et al. 1999); and most notably, (3) its arrival is emergent and its decay similarly tapered. Body waves, especially at these short distances, arrive impulsively.

### 8.4 *Inner- and outer-core phases*

Fig. 14 displays a *PKIKP* phase-arrival corresponding to a $M_W$ 6.1 earthquake in the Hindu Kush Region of Afghanistan. The seismogram is filtered between 1 and 2 Hz and annotated like those in Fig. 10, where the solid red vertical line marks our AIC-based phase pick and the dashed vertical red lines mark twice its standard deviation uncertainty estimate, 2SD$_{err}$, in both directions. In this example the residual is −1.62 s in the adjusted ak135 model, $t^\star_{ak135}$. Fig. 14 was recorded with a source-receiver geometry (212.0 km depth at 142.9°) in which only inner-core *PKIKP* and *PKiKP* phases are predicted to arrive in the time window of the seismogram as computed in ak135. Next we discuss 10 other MERMAID seismograms that triggered on core phases but which were recorded at epicentral distances beyond the *PKP* caustic (∼145°), where outer-core *PKPbc* and *PKPab* phases are also predicted to arrive close in time to their inner-core complements.

Fig. 15 is a record section corresponding to a $M_W$ 6.8 earthquake under the Ionian Sea. Unlike the unambiguous phase arrivals of the record sections presented in Fig. 5, there all direct *p* or *P* waves, here there exist four potential phase arrivals in the time window of each seismogram. A cross marks our AIC-based travel time picks on each seismogram and we color-code the four theoretical core-phase travel-time curves: blue for *PKIKP*; green for *PKPbc*; red for *PKiKP*; and magenta for *PKPab*. The number of the recording MERMAID is marked outside the right ordinate axis excluding the "P0" prefix.

We hypothesize that in cases like Fig. 15, where multiple core-phase arrivals coexist in each seismogram, the dominant phase actually being detected is *PKPbc*. This is based on a few key observations. First, we can immediately reject the possibility that the inner-core reflection *PKiKP* was detected because *PKPbc* is a higher-amplitude phase at the relevant distances (e.g. fig. 8 of Ohtaki & Kaneshima 2015). Second, arrivals associated with either of the two *PKP* branches are predicted to have higher SNRs than those associated with *PKIKP*, because the former remained in the extremely low-attenuating outer core (often approximated as having a bulk quality factor, $Q_\kappa$, of infinity), while the latter dives into the comparatively high-attenuating inner core (Romanowicz & Mitchell 2015). Lastly, *PKPbc* arrives before *PKPab* and therefore the latter could by drowned out by the persistent reverberations in

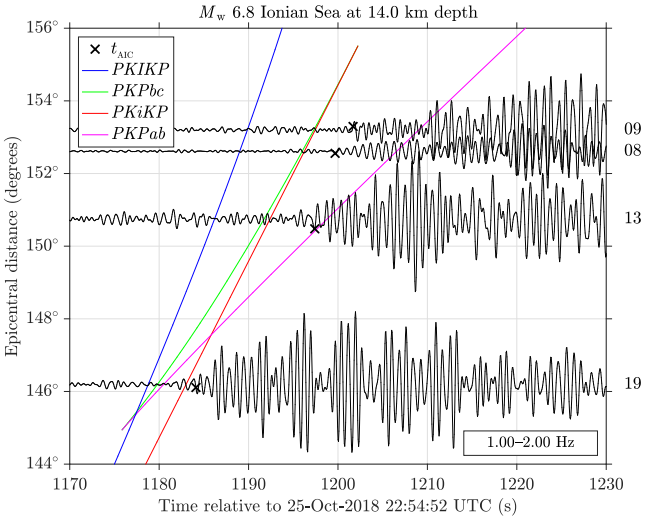


**Figure 15.** MERMAID record section filtered between 1 and 2 Hz corresponding to a $M_W$ 6.8 earthquake in the Ionian Sea. Crosses mark the observed travel times, $t_{AIC}$, on the black seismograms. Colored curves plot the theoretical travel times in ak135 of core phases: *PKIKP* (blue); *PKPbc* (green); *PKiKP* (red); and *PKPab* (magenta). MERMAID serial numbers are marked outside the right ordinate axis and exclude the "P0" prefix. All traces display an arrival that we associate with *PKPbc*, and the top trace exhibits a secondary phase marking the arrival of *PKPab*.

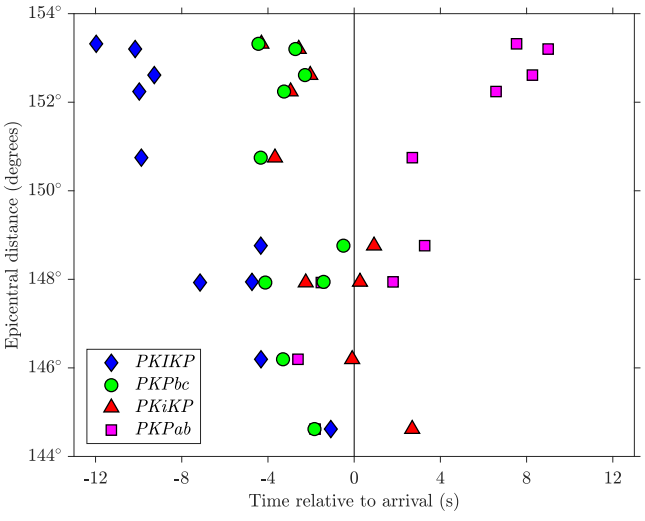


**Figure 16.** Core-phase adjusted "model residuals," $t^{\star}_{ak135} - t_{AIC}$, for MERMAID seismograms predicted to contain both inner- and outer-core phase arrivals. The purpose of this plot is to identify the phases associated with our travel-time picks. The adjusted model residuals of various core phases are colored as in Fig. 15 and further differentiated by marker: diamonds (*PKIKP*); circles (*PKPbc*); triangles (*PKiKP*); and squares (*PKPab*). Only the outer-core *PKPbc* and inner-core *PKiKP* model residuals exhibit no trend with distance; i.e. our picker is preferentially triggering on one of those two phases in this case. Because the latter is a low-amplitude reflected phase we conclude that we must be recording *PKPbc*-phase arrivals.

the water column that often dominate MERMAID seismograms for tens of seconds after the first arrival.

Fig. 16 tests our hypothesis that we are observing *PKPbc* arrivals. It plots the difference between the theoretical (colored curves in Fig. 15, but now individually adjusted for bathymetry and MERMAID cruising depth) and the actual arrival-time observations (crosses in Fig. 15), for various core phases recorded by MERMAID. We call this measure an adjusted "model residual," $t^{\star}_{ak135} - t_{AIC}$, because it has the opposite sign of all other residuals (in eqs 2–4 the word "residual" implies observation minus prediction) discussed in this study. The picks were computed in exactly the same manner as the first-arrival residuals of Section 7, except here the window used for our AIC pick was centered on *PKPbc* in an adjusted ak135 model, and the bandwidth of the filter was narrowed to consider only those frequencies between 1 and 2 Hz. The theoretical travel time phase-branches are colored as in Fig. 15 and further differentiated by their markers: diamonds for *PKIKP*; circles for *PKPbc*; triangles for *PKiKP*; and squares for *PKPab*. We see that the model residuals of both *PKPbc* and *PKiKP* phases are independent of epicentral distance and fall within $\pm$4.5 s. In contrast, the inner-core *PKIKP* and outer-core *PKPab* phases display generally negative and positive model residuals, respectively, which increase with distance.

We submit as evidence Fig. 16 to prove our hypothesis that in potentially ambiguous cases when MERMAID may be recording both inner- and outer-core phases it is most likely triggering on the latter. It shows that when all 1-D travel-time adjustments are made, and bathymetry and MERMAID cruising depth are accounted for, the phase arrivals recorded by MERMAID fall nearest to the expected arrival times of *PKPbc* and *PKiKP*, the former having the larger expected amplitude. Every *PKPbc* adjusted travel-time residual (eq. 3) in our catalog displays a positive bias, meaning that all are delayed with respect their theoretical adjusted travel times. Their mean residual is $+2.82$ s.

To test for the existence of phase-picking bias introduced by our windowing we remade Fig. 16 using *PKIKP*-centered windows and found no significant difference in arrival time picks compared with *PKPbc*-centered windows (barring two low-SNR cases that may be discarded, all arrival-time differences were within 0.1 s regardless of windowing scheme); i.e., as long as the window included the later-arriving outer-core *PKPbc* phase, our AIC-based picker identified it in favor of *PKIKP*. However, we were able to detect secondary *PKPab* arrivals in some MERMAID seismograms by running our picker recursively on time-shifted windows. See for example the top trace in Fig. 15 where both outer-core *PKPbc* and *PKPab* phases can be discerned.

### 8.5 *Unidentified (local) events*

We end this tour of the data that MERMAID has been returning beyond teleseismic *P* waves with an example of unidentified events. In Fig. 17 we see two distinct arrivals: the first near 80 seconds, and the second larger arrival around one minute later. Neither of these two arrivals match with any theoretical phase-arrival times associated with any known events in the global seismic catalogs. Our interpretation is that these two signals are both *p*- (or, less likely, *P*-) wave arrivals from two distinct very nearby events. We mark their AIC arrival times as dashed and solid red vertical lines, picked within 30 s windows (centered first on 80 s, and then on 140 s) of the seismogram filtered between 3–5 Hz, as shown in Fig. 17.

There are a few observations that support this hypothesis. First, both signals are impulsive, especially the secondary signal,

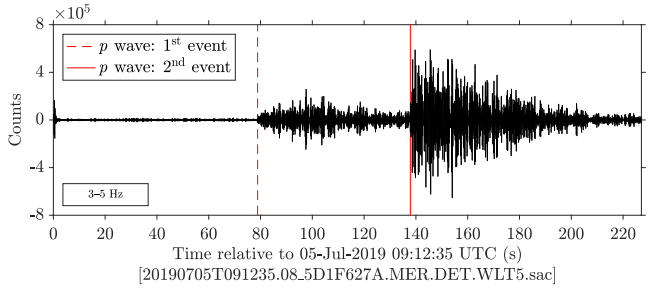


**Figure 17.** Seismogram recorded by MERMAID P008 displaying what are likely two separate unidentified events, not recorded anywhere else. Dashed and solid red vertical lines mark the AIC arrival-time picks of what we interpret to be *p*- (or possibly *P*-) wave arrivals corresponding to both events.

implying that the latter is not a *T* wave associated with the earlier signal. We note, however, that discrimination based on this simple observation is not foolproof, as rather impulsive *T* waves have been recorded in French Polynesia by the Réseau Sismique Polynésien (see Section 9) generated by various sources, including earthquakes (Talandier & Okal 1998) and volcanism (Talandier & Okal 2001). Second, it is also unlikely that the second, larger arrival is an *S* wave because: (1) it is of very high frequency, which is not expected of the shear conversion, and (2) the *S*–*P* delay time would imply an epicentral distance of approximately 500 km. Both arguments can be made against a surface wave as well, the epicentral distance computed in that case being even larger. No other MERMAID recorded these events, further proving their extremely local nature. Both arrivals are still very distinct at frequencies up to 10 Hz, not shown here, which is uncommon for identified MERMAID signals, except in the case of local events like in Fig. 13. Thus we are left to conclude that Fig. 17 depicts two distinct arrivals, from two very proximal earthquakes.

## 9 NEARBY ISLAND SEISMIC STATIONS

To this point we have discussed the MERMAID instrument, its seismograms, our procedure to match those to known global earthquakes, our methods to pick various arrivals with high precision and to estimate their uncertainties, and we have jaunted through a tour of the various signals present in the MERMAID data set. For the remainder of the study we will remain solely focused on the travel-time residuals of first-arriving *p* and *P* waves. In this section we aim to prove the tomographic utility of MERMAID residuals by comparing their statistics against measurements made for the same events at island stations located in the oceanographic neighborhood of the slowly dispersing SPPIM array.

We compare our uncalibrated MERMAID hydroacoustic pressure records (the MERMAID "seismograms") with velocity seismograms from land-based seismic sensors. We then compare the MERMAID catalog of travel-time residuals, SNR estimates, and travel-time uncertainties with a similar catalog that we construct for island seismic stations in the vicinity of MERMAID. Fig. 1 shows the bounding box of MERMAID's oceanic neighborhood, drawn with an approximately 2° buffer around the maximum extent of the SPPIM array as deployed. At 32 million km$^2$, it spans a large portion of the South Pacific and some of the North Pacific, nearly 6.5% of Earth's surface, or roughly double the area of Russia.

**Table 7.** Nearby stations with data available from Incorporated Research Institutions for Seismology (IRIS).

| FDSN code | Station | Latitude | Longitude |
|---|---|---|---|
| G | FUTU | -14.3076 | -178.1210 |
| G | PPTF | -17.5896 | -149.5652 |
| G | TAOE | -8.8549 | -140.1477 |
| AU | NIUE | -19.0763 | -169.9272 |
| C1 | VA02 | -27.1602 | -109.4345 |
| II | MSVF | -17.7448 | 178.0527 |
| II | RPN | -27.1266 | -109.3343 |
| IU | AFI | -13.9093 | -171.7772 |
| IU | FUNA | -8.5259 | 179.1965 |
| IU | KNTN | -2.7744 | -171.7185 |
| IU | PTCN | -25.0713 | -130.0953 |
| IU | RAO | -29.2450 | -177.9290 |
| IU | RAR | -21.2125 | -159.7733 |
| IU | XMAS | 2.0448 | -157.4456 |
| AM | R028A | -17.6936 | -149.5746 |
| AM | R06CD | -17.5675 | -149.5706 |
| AM | R0EF4 | -17.7207 | -149.2979 |
| AM | *RC78F | -17.5315 | -149.4748 |
| | | -17.3423 | -145.5090 |
| AM | RF737 | -17.5315 | -149.4746 |

* station relocated during SPPIM deployment

### 9.1 *Data retrieval*

We queried IRIS for terrestrial seismometers in this neighborhood with data publicly available after July 2018. The search returned 19 stations: 14 "traditional" seismic sensors from GEOSCOPE (G, 1982), the Australian National Seismograph Network (AU, 1994), the Red Sismológica Nacional (C1, 2012), and the Global Seismograph Networks IRIS/IDA (II, 1986) and IRIS/USGS (IU, 1988); and five low-cost Raspberry Shake (Bent et al. 2018; Anthony et al. 2019; Calais et al. 2019) instruments (AM, 2016). Table 7 lists these stations and their locations. They amount to one for every 2.3 million km$^2$, an area larger than Saudi Arabia, and they are very inhomogeneously clustered on islands. Additionally we obtained data from six short-period seismometers in the Réseau Sismique Polynésien (RSP), part of the French Commissariat à l'Energie Atomique et aux Energies Alternatives, Département Analyse et Surveillance de l'Environnement and maintained by the Centre Polynésien de Prévention des Tsunamis (CPPT; Talandier 1993), in Papeete, Tahiti, French Polynesia. Those stations and their locations are listed in Table 8. In addition to the studies mentioned in Section 8.5, data from the RSP have been used to seismically investigate underwater explosions (Reymond et al. 2003), Antarctic ice-calving events (Talandier et al. 2002), and submarine volcanism (Wright et al. 2008; Talandier et al. 2016). Fig. 4(a) shows the locations of the nearby stations in Tables 7 and 8 relative to the SPPIM array.

To construct the complementary data set we retrieved every available seismic trace from these "nearby" stations corresponding to all 284 identified events in our MERMAID catalog beginning five minutes before the arrival of the first ak135 phase.

**Table 8.** Nearby stations from the Réseau Sismique Polynésien (RSP), whose data were made available to us by Dr. Olivier Hyvernaud.

| Network | Station | Latitude | Longitude |
|---|---|---|---|
| RSP | PAE | -17.6610 | -149.5797 |
| RSP | TVO | -17.7825 | -149.2516 |
| RSP | PMOR | -15.0022 | -147.8941 |
| RSP | VAH | -15.2365 | -147.6284 |
| RSP | TBI | -23.3488 | -149.4608 |
| RSP | RKT | -23.1247 | -134.9720 |

For each station listed in Table 7 we requested traces from every location, for all M* (mid period; sampling rate between 1–10 Hz), B* (broadband; 10–80 Hz), H* (high broadband; 80–250 Hz), S* (short period; 10–80 Hz), and E* (extremely short period; 10–80 Hz) vertical channels. No data from mid-period instruments were returned, and all Raspberry Shake stations were short-period or extremely short-period instruments. This yielded 7305 traces. Of those, 6885 were from the traditional sensors, representing data recorded during all 284 earthquakes in the MERMAID catalog, and 420 were from Raspberry Shake instruments, accounting for data recorded during a subset of only 164 of those same earthquakes. The latter instrument class had less data available because, unlike the traditional stations that were all installed before MERMAID P008 was deployed, not all Raspberry Shake stations in Table 7 were installed before the deployment of the SPPIM array.

From the short-period instruments at the stations in Table 8 we obtained 1534 traces, corresponding to all of the 284 MERMAID events. These data are not publicly distributed or long-term archived—we thank Dr. Olivier Hyvernaud, a Geophysicist at the CPPT, for sharing them.

### 9.2 *Data processing*

Each trace had its mean and trend removed, and was tapered at both ends with a symmetric cosine taper of 5% the length of the trace (the SAC defaults). The instrument responses on record in the pole-zero (SACPZ) files were removed by deconvolution using SAC (Goldstein et al. 2003; Goldstein & Snoke 2005), converting the raw data from digital counts into velocity seismograms. Each trace was high-pass filtered above 0.1 Hz and low-passed below 10 Hz to maintain the bandwidth between 0.1–10 Hz. These frequencies were chosen to correspond as closely as possible to the sensitivity band of a MERMAID instrument, whose pressure records are filtered between those bounds before digitization, and whose instrument gain is reported by the manufacturer to be flat within that bandwidth.

SACPZ and/or StationXML files with response data were readily available for the stations in Table 7. SACPZ files were not available for the stations in Table 8. The Supplemental Material contains the necessary details and the software to perform instrument correction, which will be of use to others.

Fig. 18 replots Fig. 5 to include the velocity seismograms from nearby stations, normalized per trace for easy viewing. Station names are labeled inside the right ordinate axis. As in Fig. 5, the MERMAID traces are color-coded for easy differentiation, while those from nearby stations are gray. For clarity, overlapping traces (e.g., corresponding to stations on Tahiti, and those with multiple channels) were removed. To mimic a MERMAID seismogram we trimmed all seismograms to a length of 250 s, with the theoretical first-arrival time at 100 s (the approximate time of the STA/LTA trigger in MERMAID seismograms), and tapered them with a Hann window, as was done in Fig. 5. When required, they were decimated from their original sampling frequency to 20 Hz (or 25 Hz) before band-pass filtering to mirror the sampling frequency of MERMAID. These record sections allow us to compare waveforms and qualitatively assess SNR differences between the three instrument classes by eye. In Section 9.3 we formalize these metrics.

Fig. 18 serves merely as a visual aid to appreciate the types of signals that MERMAID records compared with other stations, given the same earthquake. We do not use the gray waveforms as shown to make first-arrival picks. Rather, for every first-arrival time reported in this study, regardless of instrument, we make the arrival-time picks on segments like those in Fig. 10, not like those shown in Fig. 5 or Fig. 18. Hence, regardless of instrument type, each trace was processed as described in Section 7. For the island stations, the only difference was that, if required, they were decimated to 20 Hz or 25 Hz to match the sampling frequency of MERMAID, and no bathymetric (or elevation) time corrections were applied. Seismograms were rejected if they were less than 200 s long, if they had any missing data within the taper window described in Section 7.1, or if the theoretical first-arrival time was near enough to an edge to result in the deconvolution taper used to remove the instrument response overlapping with the taper used for arrival-time picking.

### 9.3 *MERMAID residuals compared to nearby island stations*

Fig. 19 shows the distributions of *p*- and *P*-wave travel-time residuals (top row), their SNRs (middle row), and their two-standard deviation uncertainty estimates (bottom row), for traditional seismometers, MERMAID, and Raspberry Shake stations, left, middle, and center, respectively. We consider this a substantiation that MERMAID records tomographically-useful *p*- and *P*-wave arrivals.

Starting with the top row of Fig. 19 we plot the travel-time residuals for all first-arriving *p* and *P* waves whose residual fell between 10 s before and 10 s after their ak135 predicted arrival time. For MERMAID (Fig. 19b), we use the adjusted travel times explained in Section 7.3, and label them appropriately as $t^{\star}_{\text{res}}$, while for the traditional (Fig. 19a) and Raspberry Shake stations (Fig. 19c) no adjustments are needed. The only quality-control applied to the MERMAID residuals was the rejection of those that exceeded (positively or negatively) the 10 s cutoff. For the residuals in Fig. 19(a) and Fig. 19(c) we required the additional quality criteria that their SNRs (middle row) must be equal to or greater than the minimum SNR in the MERMAID data set (Fig. 19e); and the two-standard deviations of their uncertainty estimates (bottom row) must be equal to or less than the maximum corresponding value in the MERMAID data set (Fig. 19h). This was done to mimic the result of human intervention on the MERMAID data. Indeed, during manual review often the author would sometimes reject, for various reasons, a phase-arrival pick that aligned nicely with a theoretical arrival time. This is because our AIC picker will report any signal with an SNR greater than one. Therefore, often by algorithmic ne-

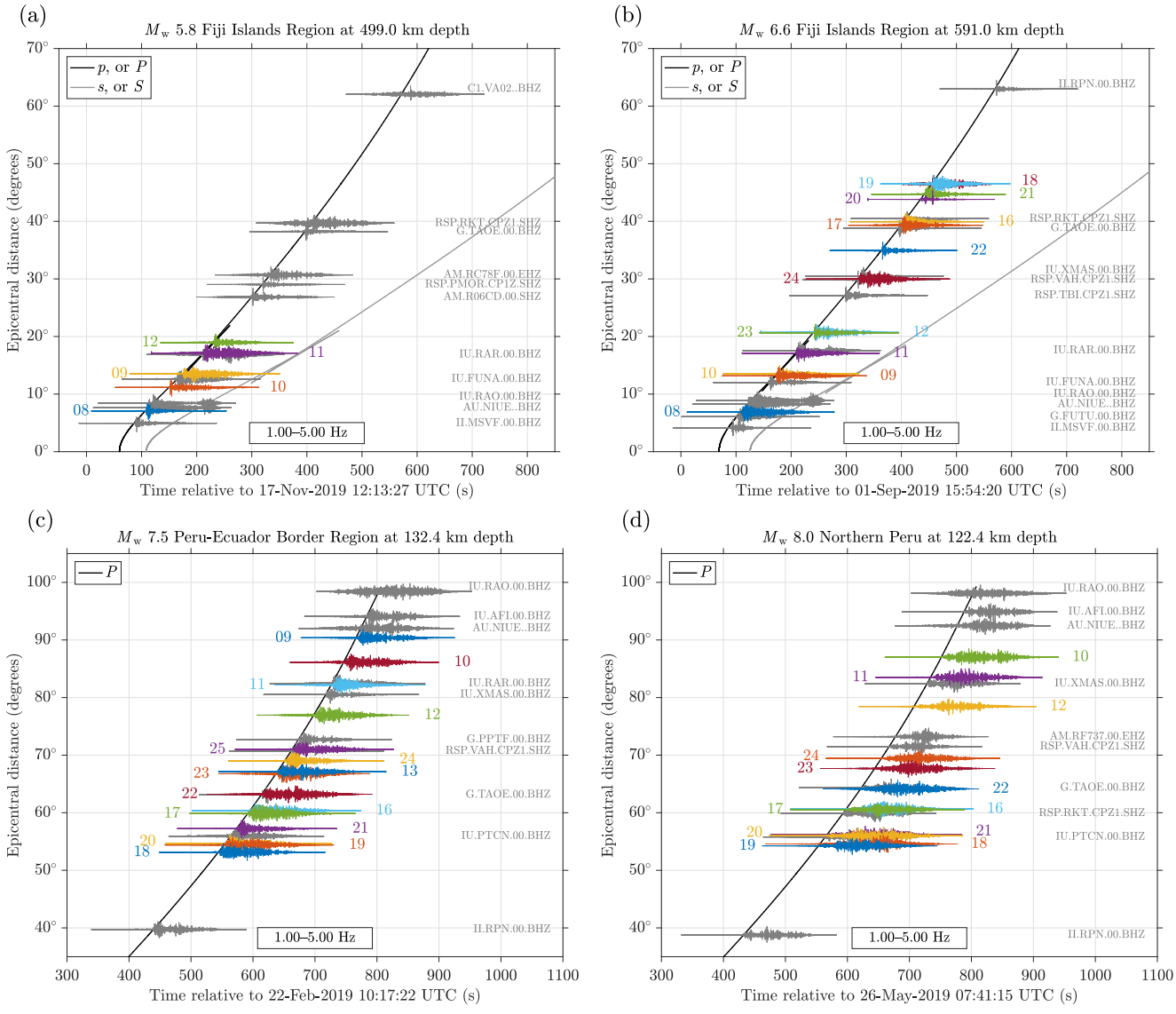


**Figure 18.** Record sections, as in Fig. 5, but now also including, in gray, data from nearby terrestrial, traditional, and Raspberry Shake stations. The gray records were trimmed to a length of 250 s and then processed in exactly the same manner as the MERMAID data so that SNR comparisons for the three instrument platforms may be made easily by eye. We see that MERMAID SNRs for the events shown compare favorably to those of the island stations. This comparison is formalized in Fig. 19d–f for high-quality residuals culled from all three instrument platforms.

cessity the picker will trigger on something that is extremely low-SNR (just above one), which by coincidence also aligns nicely with some theoretical first-arrival, but which a human would readily reject (e.g., a reflected phase from a small and distant earthquake). Every single MERMAID seismogram discussed here was reviewed by a human and a phase-arrival was verified to exist, but not every seismogram from the nearby stations was reviewed (rather, each was simply run though the same phase-picking algorithm). Therefore, it was determined that the minimum SNR and maximum two-standard deviation of the uncertainty estimates of the verified data set could serve to approximately winnow the nearby data to the standards by which the author's eye accepted or rejected a pick. This is clearly an imperfect process, and in doing it we are not implying that noise levels across all three instrument classes are equal (they are not, see the middle row). The number of traces that passed this winnowing process and contributed data to the histograms of Fig. 19(a–c) is quoted above each panel.

In total, we see that the distribution of first-arrival MERMAID residuals in Fig. 19(b) agrees well with the complementary distribution from traditional seismometers in Fig. 19(a), and to a lesser extent the same distribution computed for the Raspberry Shake stations in Fig. 19(c). All are positively biased, meaning that, on average, the arrival time of the first-arriving $p$ or $P$ wave was late compared to the ak135 reference model. The means and standard deviations of the distributions are quoted inside each panel, and the former is marked by a vertical dashed line in each. We find that MERMAID reports a mean residual that falls between the other two instrument classes. The standard deviation of the MERMAID residuals is less than the same statistic computed for the other two instrument classes. These findings bolster our claim that MERMAID reports data useful for seismic tomography.

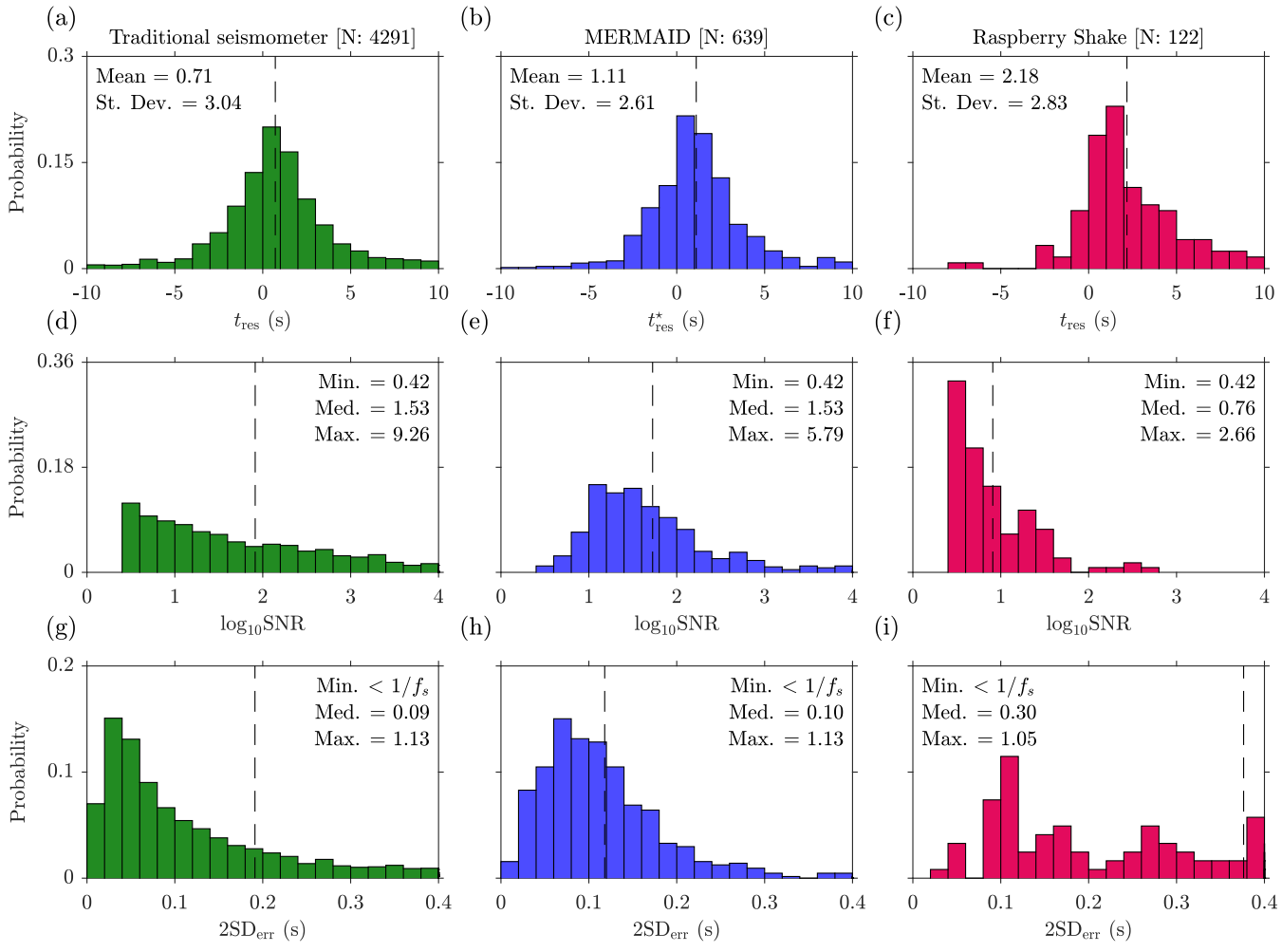


**Figure 19.** MERMAID travel-time residuals (top row), their SNRs (middle row), and their estimated uncertainties (bottom row) compared to traditional seismometers and Raspberry Shake stations installed on islands in the general neighborhood of the SPPIM deployment. MERMAID data (middle column; blue) most closely resemble those of the traditional stations (left column; green), and display much higher mean and maximum SNRs, and much lower mean estimated uncertainties, than its Raspberry Shake neighbors (right column; raspberry). MERMAID travel-time residuals and their corresponding statistics shown here were computed in adjusted ak135 models (eq. 3), while those for traditional and Raspberry Shake stations were computed for the standard ak135 model (eq. 2).

The middle row of Fig. 19 displays histograms of the SNRs of the first-arrival residuals. Quoted inside each panel panel is the minimum, median, and maximum SNR of the data set (in a base-ten logarithmic scale), and their means are marked by a dashed vertical line. Recall that the minimum SNR is the same for all three histograms because that is the minimum SNR in the MERMAID data set, and it was used as a quality threshold for the others. Despite our best attempts to winnow the data from nearby stations we believe we are still seeing the result of human intervention to a greater extent in the shape of the MERMAID histogram when compared to the others. We note that the MERMAID SNR histogram has its mode nearer its mean than in either of the other two cases, and it ramps up to its maximum value as opposed to starting at or near it, and then decreases by some exponential curve. Likely, this is the result of the author rejecting those lower-SNR picks in the MERMAID data set via manual review and not performing the same manual intervention for the other data. We therefore consider our method of winnowing the traditional and Raspberry Shake data using hard thresholds computed from the MERMAID data set to be conservative because a greater proportion of high-noise, high-uncertainty traces were retained than is the case for manual data reduction.

As with the residual data, we see that, very generally, MERMAID SNRs fall between those computed from traditional stations and Raspberry Shake instruments. The median SNRs of the MERMAID and traditional data sets are identical, and both are higher than the same statistic for the Raspberry Shake data set. Interestingly, the maximum SNR among the three differs greatly, with that of the traditional stations being much greater than MERMAID, which is much greater than Raspberry Shake. Note that the abscissa axes in Fig. 19e–f are in base-ten logarithmic scales, and the data extend beyond the limits shown. Here we plot all available data that passed our winnowing procedure from each instrument class to give a complete picture of the data set we compiled. In Fig. S1 of the Supplementary Material we recreate Fig. 19 considering only the earthquakes for which all three instrument classes had at least one station returning data—i.e., for only those events common to the three catalogs (meaning they occurred after the installation of Raspberry Shake stations, the most data-limited instrument class in

our study). That figure presents a proper apples-to-apples comparison of the SNRs returned by the three instrument classes, which we now quote. Considering the subset of events common to all catalogs, at their best: traditional seismometers recorded the first-arriving phase with an SNR of $2.6\times10^7$; MERMAID with an SNR of $6.3\times10^4$; and Raspberry Shake with and SNR of $4.6\times10^2$. In our definition of the SNR (eq. 1), for the same amplitude signal, that equates to a 26 dB reduction in the noise level of a traditional station as compared to MERMAID, and a 21 dB reduction in the noise level of MERMAID compared with Raspberry Shake. One caveat to this, however, is that we have seen that MERMAID seismograms can contain high-amplitude reverberations for many tens of seconds after the initial arrival, which 0can artificially inflate the SNR of those seismogram. Proper noise-spectra comparisons are the target of future work, but for now these approximations suffice.

For those who are interested in a more detailed comparison of the waveforms than can be gleaned from Fig. 18, we have included in the Supplementary Material Figs S2–S4, which each plot the 12 highest-SNR seismograms from the three instrument classes, presented in the same format as Fig. 10, considering only the data in the catalog common to all. Thus the first panel (a) in each plots the highest-SNR seismogram for noise comparison. There it is immediately obvious that the noise levels for both traditional stations and MERMAID stations are much lower than Raspberry Shake, with MERMAID being more like the former than the latter.

The final row of Fig. 19 shows histograms of the corresponding two-standard deviation uncertainty estimates, $2SD_{err}$, discussed in Section 7.4, associated with each first-arrival residual. These are the values quoted in the lower-right legends in each panel of Fig. 10. As in the SNR histograms of the middle row, the minimum, median, and maximum values of the uncertainty estimates are labeled inside each panel, and their means are marked by dashed vertical lines. Similarly, like in the middle row, the data extend beyond the limits of these histograms. We see that the uncertainties associated with traditional stations in Fig. 18(g) display a satisfying exponential decay, with their mode nearest the lower end of the uncertainty scale. The uncertainties associated with MERMAID residuals in Fig. 18(h) display a softer exponential decay, and they do enjoy the lowest uncertainties at nearly the same proportion as the traditional stations. The distribution of Raspberry Shake uncertainties in Fig. 18(i) is quite different from either of the other two instrument classes. It does not display the obvious peakedness at the lower-end, and it is approximately uniform across the full range from low- to high-uncertainty. Further, while the lowest and highest uncertainties corresponding to each instrument class are roughly the same, the median values are quite different, with that associated with Raspberry Shake thrice that of the others.

One caveat concerning our method of uncertainty estimation developed in Simon et al. (2020) is that for comparisons to be usefully made across various instrument types, as we have done here, the data must all be downsampled to match the sampling frequency of the lowest-sampled instrument. Our method relies on estimating uncertainties in terms of samples, which are converted to time via multiplication with the sampling interval. Therefore, given the same estimated sample uncertainty, the timing-uncertainty associated with a 100 Hz Raspberry Shake seismogram that has not been downsampled would be reported as being much lower than that associated with a 20 Hz MERMAID seismogram. In that sense, rather than considering the timing-uncertainty estimates output by our method as absolute times, the uncertainties may better serve as relative metrics for comparisons between and across data sets. Practically speaking, they map an SNR to a time, which the eye may or may not agree with, but they nonetheless provide a convenient means to sort and winnow data.

## 10 TOWARD SOUTH PACIFIC *P*-WAVE TOMOGRAPHY

Having proven the quality of MERMAID residuals compared to the best data available from permanent island stations in the area, we finally move to placing them in their geographic context to explore the velocity perturbations that they reveal in the mantle under the South Pacific.

Fig. 20 plots the highest-quality first-arrival *p*- and *P*-wave travel-time residuals of our MERMAID data set. By highest quality we specifically mean those residuals about which we are most confident. Like in Fig. 19, we performed an initial quality control of rejecting any residuals that exceeded $\pm10$ s to ensure our picker triggered on a legitimate phase arrival and not on other spurious energy. More importantly, we additionally rejected any residuals whose two-standard deviation uncertainty estimates were greater than 0.15 s, the limit beyond which the author's eye began to distrust the picks and/or when it was felt that the uncertainties were underestimated. For reference, Fig. 10 displays the full range of the data plotted in Fig. 20(c) and Fig. 20(d): from the four lowest-uncertainty residuals (top row), through the 33rd and 66th percentiles of uncertainty (second and third row, respectively), to the four highest-uncertainty residuals which passed muster in the bottom row of Fig. 10.

The residuals in Fig. 20 are color-coded blue for fast (the first-arrival is early compared with theory) and red for slow (the first-arrival is late compared to theory), and they are smeared along their ray paths from source to receiver. We plot them against three velocity models: ak135 at the top (Fig. 20a; eq. 2); ak135 adjusted for bathymetry and MERMAID cruising depth in the middle (Fig. 20c; eq. 3); and the fully-elliptical 3-D crust and mantle model LLNL-G3Dv3 at the bottom (Fig. 20e; eq. 4). In all three cases the initial residuals were computed in the adjusted ak135 model, $t^\star_{\text{ak135}}$, as is shown in Fig. 10, and then each was individually readjusted using the relative travel-time difference between that model and ak135 or LLNL-G3Dv3 to generate Fig. 20(a) and and Fig. 20(e), respectively. This means that the residuals shown here were not repicked using slightly adjusted windows computed in the three different models, which is acceptable because the maximum absolute 3-D$-$1-D travel-time difference for all residuals plotted in Fig. 20 is 4.65 s, well within a 30 s window centered on the theoretical first-arrival.

In total, 500 residuals passed these quality thresholds for the standard 1-D model, 503 for the adjusted 1-D model, and 502 were retained in the 3-D case. The distributions of those residuals are displayed in the histograms to the right of their corresponding smeared-residual map in Fig. 20. The mean, standard deviation, and skewness of the histogram is listed inside each panel, and the former is marked by a dashed vertical line. Two numbers are bracketed in the upper right corner of each histogram. The first quotes the

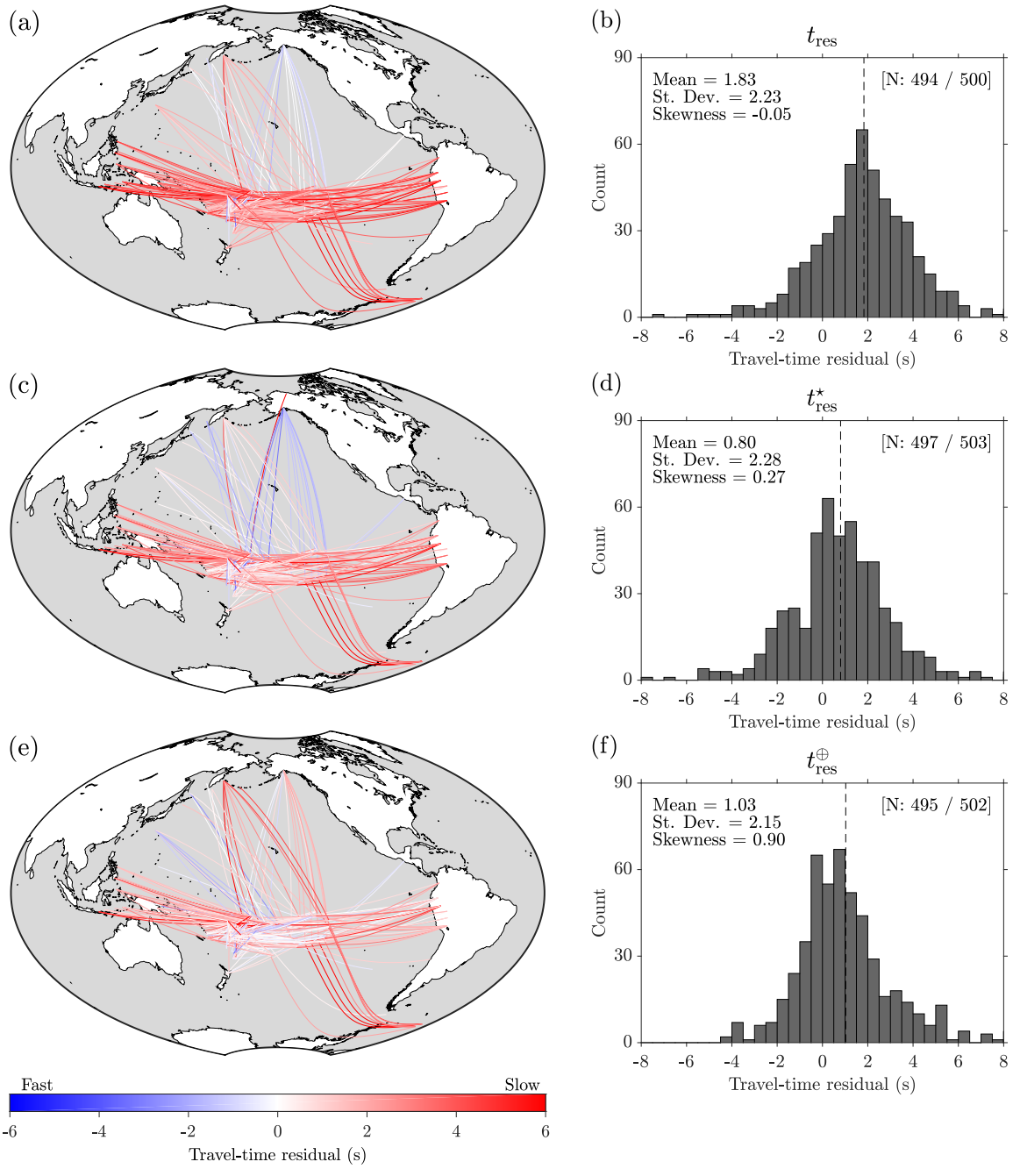


**Figure 20.** Smeared travel-time residuals computed against ak135 (a; eq. 2), ak135 corrected for bathymetry and MERMAID cruising depth (c; eq. 3), and LLNL-G3Dv3 (e; eq. 4), and the distributions of those residuals in (b), (d), and (f), respectively. Here we only show the highest-quality residuals in the MERMAID data set: those with maximum two-standard deviation estimated uncertainties smaller than 0.15 s (the final row of Fig. 10 shows the three "worst" seismograms that made the cut). The colorbar is in units of absolute time, and its color is the residual between our pick and the theoretical arrival time of the reference model (blue is fast, red is slow). The final map (e) and its corresponding histogram (f) includes 3-D mantle and ellipticity corrections absent in the two prior sets, and thus the residuals shown there are the truest picture yet of the velocity perturbations recorded by MERMAID.

number residuals plotted in the histogram (the data extend beyond the limits of the abscissa axis), and the second reports the total number of residuals which passed quality-thresholding and are shown on the corresponding smeared-residual map. The statistics quoted for each histogram were computed using the latter set.

Starting with the smeared residuals in Fig. 20(a), and their corresponding distribution in Fig 20(b), we generally see large positive anomalies (red; delayed) associated with equatorial ray paths, and lower-amplitude negative anomalies (blue; early) associated with more polar ray paths. In this case these data were not corrected for bathymetry or MERMAID cruising depth. Further, the ak135 model used here is spherical and thus does not account for ellipticity (resulting in larger residuals for equatorial ray paths than polar ray paths), or 3-D structure of the crust and mantle. The first point results in an overall mean-shift of around 1 s for all residuals in the histogram in Fig. 20(b), and the second point adds an additional

bias whose geographic distribution is governed by seismological back-azimuth. Combined, these obfuscate the true signal of mantle-velocity anomalies that MERMAID records, and they are corrected for next.

The residuals in the middle row of Fig. 20 have been adjusted for bathymetry and MERMAID cruising depth, though they remain in the spherical ak135 velocity model. As such, the mean-shift in Fig. 20(b) has been reduced by over 1 s in Fig. 20(d), but the signal of Earth's ellipticity remains visible in Fig. 20(c). In fact, that signal is now more pronounced in the North Pacific, those data generally displaying negative, or at most weakly-positive, residuals before applying the adjustment. This image proves why it will be absolutely vital in the ultimate tomographic inversion to use a fully-3-D reference velocity model to compute the travel-time residuals.

Finally, the residuals presented in the bottom row of Fig. 20 are the closest yet to the real signal of velocity perturbations within the Earth's mantle. They are computed against the fully-3-D and elliptical crust and mantle model LLNL-G3Dv3. Immediately we see that we have finally removed the signal of Earth's ellipticity; the ray paths through the North Pacific no longer display generally large negative anomalies, and residuals smeared along equatorial ray paths see their generally large positive residuals lowered slightly. The map is still very red, however, implying that the majority of the 3-D residuals recorded by MERMAID displays positive, slow anomalies for all back-azimuths. Fig. 20(f) proves this to be the case, showing that, on average, the residuals recorded by MERMAID in the South Pacific are around 1 s late compared to LLNL-G3Dv3. This means that, more often than not, MERMAID recorded seismic waves that traversed slower than predicted regions of the mantle. Interestingly, the distribution of these residuals in Fig. 20(f) is actually of higher-mean than the analogous distribution for the adjusted 1-D-model in Fig. 20(d). It is also satisfying to note that adjustment to the 3-D model lowered their standard deviation to the smallest value among all three models (albeit marginally). Further, like the other histograms in Fig. 20, this one displays positive skewness, but most interestingly, it shows the largest positive skewness among all three. Many tomographic inversions somewhat underestimate the magnitude of velocity anomalies, due to the inversion methods used (Burdick & Lekić 2017), thus it is possible that our observations are illuminating stronger slow anomalies in the mantle, possibly associated with the LLVP. Indeed, 338 of the 502 residuals plotted are positive. Further, we recorded no large negative residuals—the lowest (earliest arrival compared to theory) 3-D residual in Fig. 20(e) and Fig. 20(f) is $-4.24$ s. Conversely, the positive residuals display an exponential decay that continues to, and extends beyond, the abscissa axis limit of 8 s. The maximum 3-D residual plotted in Fig. 20(e) is $+9.50$ s, corresponding to a $M_W$ 5.3 earthquake at 10 km depth the Samoa Islands Region. It was recorded by MERMAID P012, which was 12.74° to the east, evidently sampling an extremely low-wave speed mantle along the way.

## 11 CONCLUSION

We described a new seismic instrument, the third-generation Mobile Earthquake Recording in Marine Areas by Independent Divers (MERMAID), which records earthquakes and transmits their seismograms in near real-time from the global oceans. The robotic floats dive to 1500 m depth below the sea surface and passively drift with the mid-column currents while monitoring the ambient acoustic wavefield, surfacing only to relay seismic data, their location, and to download new command files. We discussed the South Pacific Plume Imaging and Modeling (SPPIM) project, which has launched an array of 50 MERMAIDs in the South Pacific Ocean, deployed and maintained by a global consortium, EarthScope-Oceans. The array was completed in August 2019, and as of this writing 47 MERMAIDs are reporting data (see `http://earthscopeoceans.org`), and will be for many years to come. We highlighted the time-variable nature of the locations of the subset of 16 Princeton-operated MERMAIDs, from their deployment in August 2018 through the end of 2019, whose data were the focus of this study.

We proposed a workflow to quickly process the continuous data stream of incoming untagged seismograms, and to match them with earthquakes in the global catalog. We reported on the quality and size of the resultant MERMAID seismic catalog, a data product of this study, built up over 16 months of deployment: which earthquakes MERMAID recorded, and which it missed. We found that our MERMAIDs averaged around 30 event detections per year, equating to an expected 150 over their projected five-year lifespan, though we found these numbers to be highly variable between different MERMAIDs, largely due to their proximity to areas with different earthquake rates, and possibly noise regimes of a variable nature. We discussed the statistics of completeness for our MERMAID seismic catalog and parsed its numbers by magnitude to reveal the types of earthquakes to which MERMAID proved itself most sensitive. We found that for "typical" global earthquakes, an "average" MERMAID had around a 0.5% chance of recording a $M5$, a 9% chance of a recording a $M6$, a 42% chance for an $M7$, and an 81% chance of recording a $M8$ earthquake.

We summarized a procedure to pick, with high precision, the arrival times of phases in MERMAID seismograms, and to estimate their uncertainties. We commented on the discovery of phases other than mantle $P$ waves (on which the MERMAID algorithm was designed to trigger), via our phase-picking method. Among these many signals we highlighted $S$ waves, surface waves, $T$ waves, core phases, and unidentified earthquakes, the latter being small and local earthquakes, likely recorded by no other instrument on Earth.

We compared our catalog of first-arrival residuals, another data product of this study, against a similarly-derived catalog computed using all seismic instruments in the general vicinity of the SPPIM deployment. In all, we collected nearly 9000 seismograms from 25 island stations, corresponding to the 284 unique earthquakes that MERMAID recorded. We compared the distributions of first-arrival travel-time residuals, SNRs, and travel-time uncertainties between traditional seismic stations, MERMAID, and Raspberry Shake instruments, and found the MERMAID data had more in common with the former than the latter, proving that MERMAID is indeed in the process of recording tomographically useful data.

Finally, we winnowed our set of first-arrival $p$- and $P$-wave travel time residuals down to the highest-quality subset—just over 500 picks—which we compared against the fully-3-D and elliptical model LLNL-G3Dv3. We found that, on average, phase arrivals at MERMAID were delayed by approximately 1 s, revealing that

the novel ray paths sampled in this study navigated slow regions of the Earth's mantle. We displayed these residuals smeared along their ray paths to gain a geographic sense for the signature of those velocity anomalies under the South Pacific. These residuals, their weights being dictated by the associated uncertainties computed here, will form the basis of future tomographic inversions to probe the structure beneath the South Pacific Superswell.

The Supplemental Material contains text files detailing the first-arrival residuals computed in all three models discussed here, all events recorded during this study, and every GPS fix recorded by every MERMAID through its first complete dive cycle of 2020, should others be interested in relocating our stations. Any and all code generated during this study is freely and publicly available on GitHub at `https://github.com/joelsimon/omnia/`.

## 12 DATA AVAILABILITY AND RESOURCES

The MERMAID FDSN network code is MH (2003; `https://fdsn.org/networks/detail/MH/`, doi: 10.7914/SN/MH). The SAC and miniSEED files discussed here will shortly make their way into the IRIS DMC for public distribution. The Supplemental Material contains text files detailing the corresponding events and travel-time residuals computed in the three models discussed here. Continuously-updated text files of GPS fixes reported by individual MERMAIDs are available at, e.g., `http://geoweb.princeton.edu/people/simons/SOM/P008_all.txt` (the stations described here are numbered P008 through P025, excluding P014 and P015, which never existed), and described at `http://geoweb.princeton.edu/people/simons/SOM/hdr.txt`. In the Supplemental Material we include winnowed versions of those larger files detailing only the GPS fixes most relevant to this study.

Beyond homegrown software written by the authors we rely on: `irisFetch.Events` version 2.0.10, available from IRIS, to query seismic the NEIC PDE catalog; `MatTaup`, written in MATLAB by Qin Li while at the University of Washington in 2002, to compute theoretical travel times in the ak135 model of Kennett et al. (1995); `LLNL-Earth3D` to compute theoretical travel times in the LLNL-G3Dv3 model of Simmons et al. (2012); and ObsPy (Beyreuther et al. 2010) version 1.1.0 (doi: 10.5281/zenodo.165135) to convert Raspberry Shake instrument-response metadata from StationXML to SACPZ file formats. Excepting the latter two, which may be retrieved at `https://www-gs.llnl.gov/nuclear-threat-reduction/nuclear-explosion-monitoring/global-3d-seismic-tomography/`, and `https://github.com/obspy/`, respectively, we maintain all of those codes with minor modifications at `https://github.com/joelsimon/omnia/`, which furthermore contains all of our software developed for this study.

## 13 ACKNOWLEDGMENTS

Part of this work was supported by the National Science Foundation (DGE-1656466 to J. D. S. and OCE-1917058, EAR-1644399 to F. J. S. and J. C. E. I.). We are grateful to Dr. Olivier Hyvernaud from the Centre Polynésien de Prévention des Tsunamis in Papetee, Tahiti, French Polynesia, for providing seismic data from the Réseau Sismique Polynésien, as well as guidance on how to remove their instrument response. Credit goes to Yann Hello and the team at OSEAN SAS for the design of the third-generation MERMAID instrument, and to Guust Nolet for continuous support, advice, and encouragement. We thank Ifremer/Genavir, and commander Jean-François Barazer and his crew aboard the R/V *Alis* for a seamless series of deployments in the South Pacific.

We are indebted to the many people behind the scenes that collect, organize, store, and disseminate data for use by the community. Next we do our best to acknowledge each group individually for helping us collect the data set we analyzed; the Supplemental Material contains extra details about how exactly we collected these data from each individual contributor. Concerning nearby stations, event metadata were provided by: the Alaska Regional Network (AK, 1987), operated by the Alaska Earthquake Center, University of Alaska Fairbanks (AEC), doi: 10.7914/SN/AK; the United States National Seismic Network (US, 1990), operated by the Albuquerque Seismological Laboratory (ASL)/USGS, doi: 10.7914/SN/US; and the Caltech/USGS Southern California Seismic Network (SCSN, 1926), doi: 10.7914/SN/CI, operated by the California Institute of Technology and United States Geological Survey Pasadena (Caltech and USGS), which is archived at the Southern California Earthquake Data Center (SCEDC), doi: 10.7909/C3WD3xH1. The SCEDC and SCSN are funded through U.S. Geological Survey Grant G10AP00091, and the Southern California Earthquake Center, which is funded by NSF Cooperative Agreement EAR-0529922 and USGS Cooperative Agreement 07HQAG0008. Waveform data and instrument response metadata corresponding to nearby stations were provided by the following data centers: Institut de Physique du Globe de Paris (IPGP; `http://ws.ipgp.fr/`); Incorporated Research Institutions for Seismology (IRIS DMC; `https://service.iris.edu/fdsnws/`); Raspberry Shake (RASPISHAKE; `https://fdsnws.raspberryshakedata.com`); and Dr. Olivier Hyvernaud at the Centre Polynésien de Prévention des Tsunamis in Papetee, Tahiti, French Polynesia. The networks from which we queried nearby data included: GEOSCOPE (G, 1982; `http://geoscope.ipgp.fr`), doi: 10.18715/GEOSCOPE.G); Australian National Seismograph Network (AU, 1994; `https://www.fdsn.org/networks/detail/AU/`); Red Sismológica Nacional (C1, 2012; `http://www.sismologia.cl/`, doi: 10.7914/SN/C1); Global Seismograph Network—IRIS/IDA (II, 1986; `http://ida.ucsd.edu`, doi: 10.7914/SN/II); Global Seismograph Network—IRIS/USGS (IU, 1988; `http://earthquake.usgs.gov/monitoring/gsn/`, doi: 10.7914/SN/IU); Raspberry Shake (AM, 2016; `https://raspberryshake.org`, doi: 10.7914/SN/AM); and Réseau Sismique Polynésien (RSP) via Dr. Olivier Hyvernaud at the Centre Polynésien de Prévention des Tsunamis in Papetee, Tahiti, French Polynesia

## REFERENCES


Abraham, J. P., Baringer, M., Bindoff, N. L., Boyer, T., Cheng, L. J., Church, J. A., Conroy, J. L., Domingues, C. M., Fasullo, J. T., Gilson, J., Goni, G., Good, S. A., Gorman, J. M., Gouretski, V., Ishii, M., Johnson, G. C., Kizu, S., Lyman, J. M., Macdonald, A. M., Minkowycz, W. J., Moffitt, S. E., Palmer, M. D., Piola, A. R., Reseghetti, F., Schuckmann, K., Trenberth, K. E., Velicogna, I. & Willis, J. K., 2013. A review of global ocean temperature observations: Implications for ocean heat content estimates and climate change, *Rev. Geophys.*, **51**(3), 450–483, doi: 10.1002/rog.20022.

Adam, C., Yoshida, M., Suetsugu, D., Fukao, Y. & Cadio, C., 2014. Geodynamic modeling of the South Pacific superswell, *Phys. Earth Planet. Inter.*, **229**, 24–39, doi: 10.1016/j.pepi.2013.12.014.

Akaike, H., 1998, Information theory and an extension of the maximum likelihood principle, in *Selected Papers of Hirotugu Akaike*, edited by E. Parzen, K. Tanabe, & G. Kitagawa, pp. 199–213, doi: 10.1007/978–1–4612–1694–0_15, Springer, New York.

Alaska Earthquake Center, University of Alaska Fairbanks (AEC), 1987, *Alaska Regional Network*, International Federation of Digital Seismograph Networks, http://earthquake.alaska.edu. doi: 10.7914/SN/AK.

Albuquerque Seismological Laboratory (ASL)/USGS, 1988, *Global Seismograph Network (GSN—IRIS/USGS)*, International Federation of Digital Seismograph Networks, http://earthquake.usgs.gov/monitoring/gsn/. doi: 10.7914/SN/IU.

Albuquerque Seismological Laboratory (ASL)/USGS, 1990, *United States National Seismic Network (USNSN)*, International Federation of Digital Seismograph Networks, https://earthquake.usgs.gov/contactus/golden/neic.php. doi: 10.7914/SN/US.

Allen, R. V., 1978. Automatic earthquake recognition and timing from single traces, *B. Seismol. Soc. Am.*, **68**(5), 1521–1532.

Anthony, R. E., Ringler, A. T., Wilson, D. C. & Wolin, E., 2019. Do low-cost seismographs perform well enough for your network? An overview of laboratory tests and field observations of the OSOP Raspberry Shake 4D, *Seismol. Res. Lett.*, **90**(1), 219–228, doi: 10.1785/0220180251.

Babcock, J. M., Kirkendall, B. A. & Orcutt, J. A., 1994. Relationships between ocean bottom noise and the environment, *B. Seismol. Soc. Am.*, **84**(6), 1991–2007.

Balfour, N. J., Salmon, M. & Sambridge, M., 2014. The Australian Seismometers in Schools Network: Education, outreach, research, and monitoring, *Seismol. Res. Lett.*, **85**(5), 1063–1068, doi:10.1785/0220140025.

Barnes, C. R., Best, M. M. R., Johnson, F. R., Pautet, L. & Pirenne, B., 2013. Challenges, benefits, and opportunities in installing and operating cabled ocean observatories: Perspectives from NEPTUNE Canada, *IEEE J. Ocean. Eng.*, **38**(1), 144–157, doi: 10.1109/JOE.2012.2212751.

Beauduin, R., Montagner, J. P. & Karczewski, J. F., 1996. Time evolution of broadband seismic noise during the French pilot experiment OFM/SISMOBS, *Geophys. Res. Lett.*, **23**(21), 2995–2998, doi: 10.1029/96GL02880.

Bent, A. L., Cassidy, J., Prépetit, C., Lamontagne, M. & Ulysse, S., 2018. Real-time seismic monitoring in Haiti and some applications, *Seismol. Res. Lett.*, **89**(2A), 407–415, doi: 10.1785/0220170176.

Berger, J., Laske, G., Babcock, J. & Orcutt, J., 2016. An ocean-bottom seismic observatory with near real-time telemetry, *Earth Space Sci.*, **3**, 68–77, doi: 10.1002/2015EA000137.

Beyreuther, M., Barsch, R., Krischer, L., Megies, T., Behr, Y., & Wassermann, J., 2010. ObsPy: A Python toolbox for seismology, *Seismol. Res. Lett.*, **81**(3), 530–533, doi: 10.1785/gssrl.81.3.530.

Bondár, I. & Storchak, D., 2011. Improved location procedures at the International Seismological Centre, *Geophys. J. Int.*, **186**(3), 1220–1244 doi: 10.1111/j.1365-246X.2011.05107.x.

Bradner, H., 1964. Seismic measurements on the ocean bottom, *Science*, **146**(3641), 208–216, doi: 10.1126/science.146.3641.208.

Bradner, H., de Jerphanion, L. G. & Langlois, R., 1970. Ocean microseism measurements with a neutral buoyancy free-floating midwater seismometer, *B. Seismol. Soc. Am.*, **60**, 1139–1150.

Burdick, S. & Lekić, V., 2017. Velocity variations and uncertainty from transdimensional *P*-wave tomography of North America, *Geophys. J. Int.*, **209**(2), 1337–1351, doi: 10.1093/gji/ggx091.

Butler, R., Chave, A. D., K., F., Duennebier, Yoerger, D. R., Petitt, R., Harris, D., Wooding, F. B., Bowen, A. D., Bailey, J., Hildebrand, J. J. E. H. J. A. & Dodeman, A. H., 2000. Hawaii-2 observatory pioneers opportunities for remote instrumentation in ocean studies, *Eos Trans. AGU*, **81**(15), 157–168, doi: 10.1029/00EO00105.

Calais, E., Boisson, D., Symithe, S., Momplaisir, R., Prépetit, C., Ulysse, S., Etienne, G. P., Courboulex, F., Deschamps, A., Monfret, T., Ampuero, J.-P., de Lépinay, B. M., Clouard, V., Bossu, R., Fallou, L. & Bertrand, E., 2019. Monitoring Haiti's quakes with Raspberry Shake, *Eos Trans. AGU*, **100**, 17–21, doi: 10.1029/2019EO123345.

California Institute of Technology and United States Geological Survey Pasadena (Caltech and USGS), 1926, *Southern California Seismic Network*, International Federation of Digital Seismograph Networks, http://www.scsn.org. doi: 10.7914/SN/CI.

Cochran, E. S., Lawrence, J. F., Christensen, C. & Jakka, R. S., 2009. The Quake-Catcher Network: Citizen science expanding seismic horizons, *Seismol. Res. Lett.*, **80**(1), 26–30, doi: 10.1785/gssrl.80.1.26.

Cohen, A., Daubechies, I. & Feauveau, J., 1992. Biorthogonal bases of compactly supported wavelets, *Comm. Pure Appl. Math.*, **45**, 485–560, doi: 10.1002/cpa.3160450502.

Collins, J. A., Vernon, F. L., Orcutt, J. A., Stephen, R. A., Peal, K. R., Wooding, F. B., Spiess, F. N. & Hildebrand, J. A., 2001. Broadband seismology in the oceans: Lessons from the Ocean Seismic Network Pilot Experiment, *Geophys. Res. Lett.*, **28**(1), 49–52, doi: 10.1029/2000GL011638.

Cottaar, S. & Lekić, V., 2016. Morphology of seismically slow lower-mantle structures, *Geophys. J. Int.*, **207**(2), 1122–1136, doi: 10.1093/gji/ggw324.

Cottaar, S. & Romanowicz, B., 2012. An unsually large ULVZ at the base of the mantle near Hawaii, *Earth Planet. Sci. Lett.*, **355–356**, 213–222, doi: 10.1016/j.epsl.2012.09.005.

Cowles, T., Delaney, J., Orcutt, J. & Weller, R., 2010. The Ocean Observatories Initiative: Sustained ocean observing across a range of spatial scales, *Mar. Technol. Soc. J.*, **44**(6), 54–64, doi: 10.4031/MTSJ.44.6.21.

Davaille, A., 1999. Simultaneous generation of hotspots and superswells by convection in a heterogeneous planetary mantle, *Nature*, **402**(6763), 756–760, doi: 10.1038/45461.

Davis, R. E., 2005. Intermediate-depth circulation of the Indian and South Pacific oceans measured by autonomous floats, *J. Phys. Oceanog.*, **35**(5), 683–707, doi: 10.1175/JPO2702.1.

Davis, R. E., Webb, D. C., Regier, L. A. & Dufour, J., 1992. The Autonomous Lagrangian Circulation Explorer (ALACE), *J. Atmos. Ocean Tech.*, **9**(3), 264–285, doi: 10.1175/1520-0426(1992)009<0264:TALCE>2.0.CO;2.

Davis, R. E., Sherman, J. T. & Dufour, J., 2001. Profiling ALACEs and other advances in autonomous subsurface floats, *J. Atmos. Ocean Tech.*, **18**(6), 982–993, doi: 10.1175/1520–0426(2001)018<0982:PAAOAI>2.0.CO;2.

Dougherty, M. E. & Stephen, R. A., 1991. Seismo/acoustic propagation through rough seafloors, *J. Acoust. Soc. Am.*, **90**(5), 2637–2651, doi: 10.1121/1.402067.

Duennebier, F. K., Becker, N. C., Caplan-Auerbach, J., Clague, D. A., Cowen, J., Cremer, M., Garcia, M., Goff, F., Malahoff, A., McMurtry, G., Midson, B. P., Moyer, C. L., Norman, M., Okubo, P., Resing, J. A., Rhoses, J. M., Rubin, K., Sansone, F. J., Smith, J. R., Spencer, K., Wen, X. & Wheat, C. G., 1997. Researchers rapidly respond to submarine

activity at Loihi volcano, Hawaii, *Eos Trans. AGU*, **78**(22), 229–237, doi: 10.1029/97EO00150.

Duennebier, F. K., Harris, D. W., Jolly, J., Babinec, J., Copson, D. & Stiffel, K., 2002. The Hawaii-2 Observatory seismic system, *IEEE J. Ocean. Eng.*, **27**(2), 212–217, doi: 10.1109/JOE.2002.1002475.

Ewing, M. & Vine, A., 1938. Deep-sea measurements without wires or cables, *Eos Trans. AGU*, **19**(1), 248–251, doi: 10.1029/TR019i001p00248.

Ewing, W. M., Jardetzky, W. S. & Press, F., 1957. *Elastic Waves in Layered Media*, Intern. Ser. Earth Sci., McGraw-Hill, New York.

Farra, V., Stutzmann, E., Gualtieri, L., Schimmel, M. & Ardhuin, F., 2016. Ray-theoretical modeling of secondary microseism *P* waves, *Geophys. J. Int.*, **206**(3), 1730–1739, doi: 10.1093/gji/ggw242.

Favali, P. & Beranzoli, L., 2006. Seafloor observatory science: a review, *Ann. Geophys.–Italy*, **49**(2–3), 515–567, doi: 10.4401/ag–3132.

Fernando, B., Leng, K. & Nissen-Meyer, T., 2020. Oceanic high-frequency global seismic wave propagation with realistic bathymetry, *Geophys. J. Int.*, **222**(2), 1178–1194, doi: 10.1093/gji/ggaa248.

Fox, C. G., Dziak, R. P., Matsumoto, H. & Schreiner, A. E., 1993. Potential for monitoring low-level seismicity on the Juan-de-Fuca ridge using military hydrophone arrays, *Mar. Tech. Soc. J.*, **27**(4), 22–30.

French, S. W. & Romanowicz, B., 2015. Broad plumes rooted at the base of the Earth's mantle beneath major hotspots, *Nature*, **525**, 95–99, doi: 10.1038/nature14876.

Garnero, E. J., McNamara, A. K. & Shim, S.-H., 2016. Continent-sized anomalous zones with low seismic velocity at the base of Earth's mantle, *Nature Geosci.*, **9**, 481–489, doi: 10.1038/NGEO2733.

GEBCO Bathymetric Compilation Group, 2019, The GEBCO_2019 grid—A continuous terrain model of the global oceans and land, Tech. rep., British Oceanographic Data Centre, National Oceanography Centre, NERC.

Geoscience Australia (GA), 1994, *Australian National Seismograph Network (ANSN)*, International Federation of Digital Seismograph Networks, https://www.fdsn.org/networks/detail/AU/.

Goldstein, P. & Snoke, A., 2005. SAC availability for the IRIS community, *IRIS DMC Electronic Newsletter*, **7**(1).

Goldstein, P., Dodge, D., Firpo, M. & Minner, L., 2003, SAC2000: Signal processing and analysis tools for seismologists and engineers, in *International Handbook of Earthquake and Engineering Seismology, Part B*, edited by W. H. Lee, H. Kanamori, P. C. Jennings, & C. Kisslinger, vol. 81 of **International Geophysics**, pp. 1613–1614, doi: 10.1016/S0074-6142(03)80284-X, Academic Press.

Gould, W. J., 2005. From Swallow floats to Argo—The development of neutrally buoyant floats, *Deep-Sea Res. II*, **52**(3–4), 529–543, doi: 10.1016/j.dsr2.2004.12.005.

Gualtieri, L., Stutzmann, E., Capdeville, Y., Ardhuin, F., Schimmel, M., Mangeney, A. & Morelli, A., 2013. Modelling secondary microseismic noise by normal mode summation, *Geophys. J. Int.*, **193**(3), 1732–1745, 10.1093/gji/ggt090.

Gualtieri, L., Stutzmann, E., Juretzek, C., Hadziioannou, C. & Ardhuin, F., 2019. Global scale analysis and modelling of primary microseisms, *Geophys. J. Int.*, **218**(1), 560–572, doi: 10.1093/gji/ggz161.

Hammond, J. O. S., England, R., Rawlinson, N., Curtis, A., Sigloch, K., Harmon, N. & Baptie, B., 2019. The future of passive seismic acquisition, *Astron. Geoph.*, **60**(2), 2.37–2.42, doi: 10.1093/astrogeo/atz102.

Helffrich, G., Wookey, J. & Bastow, I., 2013. *The Seismic Analysis Code. A Primer and User's Guide*, Cambridge Univ. Press, Cambridge, UK.

Hello, Y., Ogé, A., Sukhovich, A. & Nolet, G., 2011. Modern mermaids: New floats image the deep Earth, *Eos Trans. AGU*, **92**(40), 337–338, doi: 10.1029/2011EO400001.

Hirata, K., Aoyagi, M., Mikada, H., Kawaguchi, K., Kaiho, Y., Iwase, R., Morita, S., Fujisawa, I., Sugioka, H., Mitsuzawa, K., Suyehiro, K., Kinoshita, H. & Fujiwara, N., 2002. Real-time geophysical measurements on the deep seafloor using submarine cable in the Southern Kurile subduction zone, *IEEE J. Ocean. Eng.*, **27**(2), 170–181, doi: 10.1109/JOE.2002.1002471.

Houser, C., Masters, G., Shearer, P. & Laske, G., 2008. Shear and compressional velocity models of the mantle from cluster analysis of long-period waveforms, *Geophys. J. Int.*, **174**(1), 195–212, doi: 10.1111/j.1365-246X.2008.03763.x.

Institut le Physique du Globe de Paris (IPGP), & Ecole et Observatoire des Sciences de la Terre de Strasbourg (EOST), 1982, *GEOSCOPE, French Global Network of broad band seismic stations*, Institut de Physique du Globe de Paris (IPGP), http://geoscope.ipgp.fr. doi: 10.18715/GEOSCOPE.G.

International Seismological Centre, 2015, *On-line Bulletin*, http://www.isc.ac.uk. doi: 10.31905/D808B830.

Jeddi, Z., Voss, P. H., Sørensen, M. B., Danielsen, F., Dahl-Jensen, T., Larsen, T. B., Nielsen, G., Hansen, A., Jakobsen, P. & Frederiksen, P. O., 2020. Citizen seismology in the Arctic, *Front. Earth Sci.*, **8**, 139, doi: 10.3389/feart.2020.00139.

Joubert, C., Nolet, G., Bonnieux, S., Deschamps, A., Dessa, J.-X. & Hello, Y., 2016. *P*-delays from floating seismometers (MERMAID), part I: Data processing, *Seismol. Res. Lett.*, **87**(1), 73–80, doi: 10.1785/0220150111.

Kagan, Y. Y., 2003. Accuracy of modern global earthquake catalogs, *Phys. Earth Planet. Inter.*, **135**(2–3), 173–209, doi: 10.1016/S0031–9201(02)00214–5.

Kebe, H.-W., 1981. Self-noise measurements using a moored sonobuoy with a suspended hydrophone, *Marine Geophys. Res.*, **5**(2), 207–220, doi: 10.1007/BF00163480.

Kelley, D. S., Delaney, J. R. & the Cabled Array Team, 2016, NSF's cabled array: A wired tectonic plate and overlying ocean, in *OCEANS 2016 MTS/IEEE Monterey*, pp. 1–10, doi: 10.1109/OCEANS.2016.7761398, Proc. IEEE.

Kennett, B. L. N., Engdahl, E. R. & Buland, R., 1995. Constraints on seismic velocities in the Earth from travel-times, *Geophys. J. Int.*, **122**(1), 108–124, doi: 10.1111/j.1365-246X.1995.tb03540.x.

Kohler, M. D., Hafner, K., Park, J., Irving, J. C. E., Caplan-Auerbach, J., Collins, J., Berger, J., Tréhu, A. M., Romanowicz, B. & Woodward, R. L., 2020. A plan for a long-term, automated, broadband seismic monitoring network on the global seafloor, *Seismol. Res. Lett.*, **91**(3), 1343–1355, doi: 10.1785/0220190123.

Kong, Q., Allen, R. M. & Schreier, L., 2016. MyShake: Initial observations from a global smartphone seimic network, *Geophys. Res. Lett.*, **43**, 9588–9594, doi: 10.1002/2016GL070955.

Kugler, S., Bohlen, T., Forbriger, T., Bussat, S. & Klein, G., 2007. Scholte-wave tomography for shallow-water marine sediments, *Geophys. J. Int.*, **168**(2), 551–570, doi: 10.1111/j.1365-246X.2006.03233.x.

Lavender, K. L., Davis, R. E. & Owens, W. B., 2000. Mid-depth recirculation observed in the interior Labrador and Irminger seas by direct velocity measurements, *Nature*, **407**, 66–69, doi: 10.1038/35024048.

Lewis, B. T. R. & Dorman, L. M., 1998. Recording teleseisms on the seafloor; an example from the Juan de Fuca plate, *B. Seismol. Soc. Am.*, **88**(1), 107–116.

Lindsey, N. J., Dawe, T. C. & Ajo-Franklin, J. B., 2019. Illuminating seafloor faults and ocean dynamics with dark fiber distributed acoustic sensing, *Science*, **366**(6469), 1103–1107, doi: 10.1126/science.aay5881.

Matabos, M., Best, M., Blandin, J., Hoeberechts, M., Juniper, S. K., Pirenne, B., Robert, K., Ruhl, H. A., Sarrazin, J. & Vardaro, M., 2016, Seafloor observatories, in *Biological Sampling in the Deep Sea*, edited by M. Clark, M. Consalvey, & A. A. Rowden, chap. 14, pp. 306–337, doi: 10.1002/9781118332535.ch14, Wiley, Chichester, UK.

McCreery, C. S. & Duennebier, F. K., 1993. Correlation of deep ocean noise (0.4-30 Hz) with wind, and the Holu Spectrum — A worldwide constant, *J. Acoust. Soc. Am.*, **93**(5), 2639–2648, doi: 10.1121/1.405838.

McNutt, M. K. & Fischer, K. M., 1987, The South Pacific superswell, in *Seamounts, Islands, and Atolls*, edited by B. H. Keating, P. Fryer, R. Ba-

tiza, & G. W. Boehlert, vol. 43 of **Geophysical Monograph**, pp. 25–34, doi: 10.1029/GM043, Amer. Geophys. Union.

McNutt, M. K. & Judge, A. V., 1990. The Superswell and mantle dynamics beneath the South Pacific, *Science*, **248**(4958), 969–975, doi: 10.1126/science.248.4958.969.

Montagner, J.-P., Lognonné, P., Beauduin, R., Roult, G., Karczewski, J.-F. & Stutzmann, E., 1998. Towards multiscalar and multiparameter networks for the next century: The French efforts, *Phys. Earth Planet. Inter.*, **108**(2), 155–174, doi: 10.1016/S0031-9201(98)00093-4.

Moulik, P. & Ekström, G., 2016. The relationships between large-scale variations in shear velocity, density, and compressional velocity in the Earth's mantle, *J. Geophys. Res.*, **121**(4), 2737–2271, doi: 10.1002/2015JB012679.

Munk, W. H., 1974. Sound channel in an exponentially stratified ocean, with application to SOFAR, *J. Acoust. Soc. Am.*, **55**(2), 220–226, doi: 10.1121/1.1914492.

Nichols, S. M. & Bradley, D. L., 2016. Global examination of the wind-dependence of very low frequency underwater ambient noise, *J. Acoust. Soc. Am.*, **139**(3), 1110–1123, doi: 10.1121/1.4943544.

Nolet, G., 2008. *A Breviary for Seismic Tomography*, Cambridge Univ. Press, Cambridge, UK.

Nolet, G., Hello, Y., van der Lee, S., Bonnieux, S., Ruiz, M. C., Pazmino, N. A., Deschamps, A., Regnier, M. M., Font, Y., Chen, Y. J. & Simons, F. J., 2019. Imaging the Galápagos mantle plume with an unconventional application of floating seismometers, *Sci. Rep.*, **9**, 1326, doi: 10.1038/s41598–018–36835–w.

Ohtaki, T. & Kaneshima, S., 2015. Independent estimate of velocity structure of Earth's lowermost outer core beneath the northeast Pacific from PKiKP−PKPbc differential traveltime and dispersion in PKPbc, *J. Geophys. Res.*, **120**(11), 7572–7586, doi: 10.1002/2015JB012140.

Okal, E. A., 2008. The generation of *T* waves by earthquakes, *Adv. Geoph.*, **49**, 1–65, doi: 10.1016/S0065–2687(07)49001–X.

Park, M., Odom, R. I. & Soukup, D. J., 2001. Modal scattering: a key to understanding oceanic T-waves, *Geophys. Res. Lett.*, **28**(17), 3401–3404, doi: 10.1029/2001GL013472.

Petitt, R. A., Harris, D. W., Wooding, B., Bailey, J., Jolly, J., Hobart, E., Chave, A. D., Duennebier, F., Butler, R., Bowen, A. & Yoerger, D., 2002. The Hawaii-2 Observatory, *IEEE-OE*, **27**(2), 245–253, doi: 10.1109/JOE.2002.1002479.

Princeton University, 2003, *Mobile Earthquake Recording in Marine Areas by Independent Divers (*MERMAID*)*, International Federation of Digital Seismograph Networks, https://www.fdsn.org/networks/detail/MH/. doi: 10.7914/SN/MH.

Raspberry Shake, S.A., 2016, *Raspberry Shake (RASPISHAKE)*, International Federation of Digital Seismograph Networks, https://raspberryshake.org. doi: 10.7914/SN/AM.

Rawlinson, N., Pozgay, S. & Fishwick, S., 2010. Seismic tomography: A window into deep Earth, *Phys. Earth Planet. Inter.*, **178**, 101–135, doi: 10.1016/j.pepi.2009.10.002.

Red Sismológic Nacional, 2012, *Universidad de Chile (UCH)*, International Federation of Digital Seismograph Networks, http://www.sismologia.cl/. doi: 10.7914/SN/C1.

Reid, I., Reichle, M., Brune, J. & Bradner, H., 1973. Microearthquake studies using sonobuoys: Preliminary results from the Gulf of California, *Geophys. J. R. Astron. Soc.*, **34**(3), 365–379, doi: 10.1111/j.1365-246X.1973.tb02401.x.

Reymond, D., Hyvernaud, O., Talandier, J. & Okal, E. A., 2003. *T*-Wave detection of two underwater explosions off Hawaii on 13 April 2000, *B. Seismol. Soc. Am.*, **93**(2), 804–816, doi: 10.1785/0120010296.

Rinard Hinga, B., 2015. *Ring of Fire: An Encyclopedia of the Pacific Rim's earthquakes, tsunamis, and volcanoes*, ABC-CLIO, Santa Barbara, Calif.

Roemmich, D., Johnson, G. C., Riser, S., Davis, R., Gilson, J., Owens, W. B., Garzoli, S. L., Schmid, C. & Ignaszewski, M., 2009. The Argo program: Observing the global ocean with profiling floats, *Oceanography*, **22**(2), 34–43, doi: 10.5670/oceanog.2009.36.

Romanowicz, B., 2008. Using seismic waves to image Earth's structure, *Nature*, **451**, 266–268, doi: 10.1038/nature06583.

Romanowicz, B. & Giardini, D., 2001. The future of permanent seismic networks, *Science*, **293**(5537), 2000–2001, doi: 10.1126/science.1061771.

Romanowicz, B., Stakes, D., Dolenc, D., Neuhauser, D., McGill, P., Urhammer, R. & Ramirez, T., 2006. The Monterey Bay broadband ocean bottom seismic observatory, *Ann. Geophys.–Italy*, **49**(2–3), 607–623, doi: 10.4401/ag-3132.

Romanowicz, B. A. & Mitchell, B. J., 2015, Deep Earth structure: Q of the Earth from crust to core, in *Treatise on Geophysics*, edited by B. Romanowicz & A. M. Dziewoński, vol. 1, pp. 789–827, doi: 10.1016/B978–0–444–53802–4.00021–X, Elsevier, Amsterdam, Neth.

Rossby, T. & Webb, D., 1970. Observing abyssal motions by tracking Swallow floats in the SOFAR channel, *Deep-Sea Res.*, **17**(2), 359–365, doi: 10.1016/0011-7471(70)90027-6.

Scripps Institution of Oceanography (SIO), 1986, *Global Seismograph Network (GSN—IRIS/IDA)*, International Federation of Digital Seismograph Networks, http://ida.ucsd.edu. doi: 10.7914/SN/II.

Shinohara, M., Kanazawa, T., Yamada, T., Machida, Y., Shinbo, T. & Sakai, S., 2014. New compact ocean bottom cabled seismometer system deployed in the Japan Sea, *Mar. Geopys. Res.*, **35**, 231–242, doi: 10.1007/s11001–013–9197–1.

Simmons, N. A., Forte, A. M., Boschi, L. & Grand, S. P., 2010. GyPSuM: A joint tomographic model of mantle density and seismic wave speeds, *J. Geophys. Res.*, **115**, B12310, doi:10.1029/2010JB007631.

Simmons, N. A., Myers, S. C., Johannesson, G. & Matzel, E., 2012. LLNL-G3Dv3: Global P wave tomography model for improved regional and teleseismic travel time prediction, *J. Geophys. Res.*, **117**, B10302, doi: 10.1029/2012JB009525.

Simon, J. D., Simons, F. J. & Nolet, G., 2020. Multiscale estimation of event arrival times and their uncertainties in hydroacoustic records from autonomous oceanic floats, *B. Seismol. Soc. Am.*, **110**(3), 970–997, doi: 10.1785/0120190173.

Simons, F. J., Dando, B. D. E. & Allen, R. M., 2006. Automatic detection and rapid determination of earthquake magnitude by wavelet multiscale analysis of the primary arrival, *Earth Planet. Sci. Lett.*, **250**(1–2), 214–223, doi: 10.1016/j.epsl.2006.07.039.

Simons, F. J., Nolet, G., Babcock, J. M., Davis, R. E. & Orcutt, J. A., 2006. A future for drifting seismic networks, *Eos Trans. AGU*, **87**(31), 305 & 307, doi: 10.1029/2006EO310002.

Simons, F. J., Nolet, G., Georgief, P., Babcock, J. M., Regier, L. A. & Davis, R. E., 2009. On the potential of recording earthquakes for global seismic tomography by low-cost autonomous instruments in the oceans, *J. Geophys. Res.*, **114**, B05307, doi: 10.1029/2008JB006088.

Slack, P. D., Fox, C. G. & Dziak, R. P., 1999. *P* wave detection thresholds, $P_n$ velocity estimates, and *T* wave location uncertainty from oceanic hydrophones, *J. Geophys. Res.*, **104**(B6), 13061–13072.

Sladen, A., Rivet, D., Ampuero, J. P., Barros, L. D., Hello, Y., Calbris, G. & Lamare, P., 2019. Distributed sensing of earthquakes and ocean-solid Earth interactions on seafloor telecom cables, *Nat. Commun.*, **10**, 5777, doi: 10.1038/s41467–019–13793–z.

Stephen, R. A., 1988. A review of finite difference methods for seismo-acoustics problems at the seafloor, *Rev. Geophys.*, **26**(3), 445–458, doi: 10.1029/RG026i003p00445.

Stephen, R. A., Spiess, F. N., Collins, J. A., Hildebrand, J. A., Orcutt, J. A., Peal, K. R., Vernon, F. L. & Wooding, F. B., 2003. Ocean Seismic Network Pilot Experiment, *Geochem. Geophys. Geosys.*, **4**(10), 1092, doi: 10.1029/2002GC000485.

Subedi, S., Hetúnyi, G., Denton, P. & Sauron, A., 2020. Seismology

at school in Nepal: A program for educational and citizen seismology through a low-cost seismic network, *Front. Earth Sci.*, **8**, 73, doi: 10.3389/feart.2020.00073.

Suetsugu, D. & Shiobara, H., 2014. Broadband ocean-bottom seismology, *Annu. Rev. Earth. Planet. Sc.*, **42**, 27–43, doi: 10.1146/annurev–earth–060313–054818.

Sukhovich, A., Irisson, J.-O., Simons, F. J., Ogé, A., Hello, Y. M., Deschamps, A. & Nolet, G., 2011. Automatic discrimination of underwater acoustic signals generated by teleseismic *P*-waves: A probabilistic approach, *Geophys. Res. Lett.*, **38**(18), L18605, doi: 10.1029/2011GL048474.

Sukhovich, A., Irisson, J.-O., Perrot, J. & Nolet, G., 2014. Automatic recognition of *T* and teleseismic *P* waves by statistical analysis of their spectra: An application to continuous records of moored hydrophones, *J. Geophys. Res.*, **119**(8), 6469–6485, doi: 10.1002/2013JB010936.

Sukhovich, A., Bonnieux, S., Hello, Y., Irisson, J.-O., Simons, F. J. & Nolet, G., 2015. Seismic monitoring in the oceans by autonomous floats, *Nat. Commun.*, **6**, 8027, doi: 10.1038/ncomms9027.

Swallow, J. C., 1955. A neutral-buoyancy float for measuring deep currents, *Deep-Sea Res.*, **3**(1), 74–81, doi: 10.1016/0146-6313(55)90037-X.

Talandier, J., 1993. French Polynesia Tsunami Warning Center (CPPT), *Nat. Haz.*, **7**(3), 237–256, doi: 10.1007/BF00662649.

Talandier, J. & Okal, E. A., 1998. On the mechanism of conversion of seismic waves to and from T waves in the vicinity of island shores, *B. Seismol. Soc. Am.*, **88**(2), 621–632.

Talandier, J. & Okal, E. A., 2001, Identification criteria for sources of *T* waves recorded in french polynesia, in *Monitoring the Comprehensive Nuclear-Test-Ban Treaty: Hydroacoustics*, edited by C. deGroot Hedlin & J. Orcutt, vol. 158, pp. 567–603, doi: 10.1007/978-3-0348-8270-5_7, Birkhäuser Verlag, Basel.

Talandier, J., Hyvernaud, O., Okal, E. A. & Piserchia, P.-F., 2002. Long-range detection of hydroacoustic signals from large icebergs in the Ross Sea, Antarctica, *Earth Planet. Sci. Lett.*, **203**(1), 519–534, doi: 10.1016/S0012-821X(02)00867-1.

Talandier, J., Hyvernaud, O. & Maury, R. C., 2016. Unusual seismic activity in 2011 and 2013 at the submarine volcano Rocard, Society hot spot (French Polynesia), *Geophys. Res. Lett.*, **43**(9), 4247–4254, doi: 10.1002/2016GL068342.

Tanaka, S., Obayashia, M., Suetsugua, D., H. Shiobarab, H. S., Yoshimitsua, J., Kanazawab, T., Fukaoa, Y. & Barruolc, G., 2009. P-wave tomography of the mantle beneath the South Pacific Superswell revealed by joint ocean floor and islands broadband seismic experiments, *Phys. Earth Planet. Inter.*, **172**(3–4), 268–277, doi: 10.1016/j.pepi.2008.10.016.

Tanaka, S., Suetsugu, D., Shiobara, H., Sugioka, H., Kanazawa, T., Fukao, Y., Barruol, G. & Reymond, D., 2009. On the vertical extent of the large low shear velocity province beneath the South Pacific Superswell, *Geophys. Res. Lett.*, **36**(7), L07305, doi: 10.1029/2009GL037568.

Tesoniero, A., Auer, L. & Cammarano, L. B. F., 2015. Hydration of marginal basins and compositional variations within the continental lithospheric mantle inferred from a new global model of shear and compressional velocity, *J. Geophys. Res.*, **120**, 7789–7813, doi: 10.1002/2015JB012026.

Tolstoy, I. & Ewing, M., 1950. The *T* phase of shallow-focus earthquakes, *B. Seismol. Soc. Am.*, **40**(1), 25–51.

Tolstoy, M., Cowen, J. P., Baker, E. T., Fornari, D. J., Rubin, K. H., Shank, T. M., Waldhauser, F., Bohnenstiehl, D. R., Forsyth, D. W., Holmes, R. C., Love, B., Perfit, M. R., Weekly, R. T., Soule, S. A. & Glazer, B., 2006. A sea-floor spreading event captured by seismometers, *Science*, **314**(5807), 1920–1922, doi: 10.1126/science.1133950.

Toomey, D. R., Allen, R. M., Barclay, A. H., Bell, S. W., Bromirski, P. D., Carlson, R. L., Chen, X., Collins, J. A., Dziak, R. P., Evers, B., Forsyth, D. W., Gerstoft, P., Hooft, E. E., Livelybrooks, D., Lodewyk, J. A., Luther, D. S., McGuire, J. J., Schwartz, S. Y., Tolstoy, M., Tréhu, A. M., Weirathmueller, M. & Wilcock, W. S., 2014. The Cascadia Initiative: A sea change in seismological studies of subduction zones, *Oceanography*, **27**(2), 138–150, doi: 10.5670/oceanog.2014.49.

Weatherall, P., Marks, K. M., Jakobsson, M., Schmitt, T., Tani, S., Arndt, J. E., Rovere, M., Chayes, D., Ferrini, V. & Wigley, R., 2015. A new digital bathymetric model of the world's oceans, *Earth Space Sci.*, **2**, 331–345, doi: 10.1002/2015EA000107.

Webb, S. C., 1998. Broadband seismology and noise under the ocean, *Rev. Geophys.*, **36**(1), 105–142.

Webb, S. C. & Cox, C. S., 1986. Observations and modeling of seafloor microseisms, *J. Geophys. Res.*, **91**(B7), 7343–7358.

Webb, S. C. & Crawford, W. C., 2003. Shallow-water broadband OBS seismology, *B. Seismol. Soc. Am.*, **100**(4), 1770–1778, doi: 10.1785/0120090203.

Wessel, P. & Kroenke, L., 1997. A geometric technique for relocating hotspots and refining absolute plate motions, *Nature*, **387**(6631), 365–369, doi: 10.1038/387365a0.

Wessel, P., Sandwell, D. T. & Kim, S.-S., 2010. The global seamount census, *Oceanography*, **23**(1), 24–33, doi: 10.5670/oceanog.2010.60.

Whitmarsh, R. B., 1970. An ocean bottom pop-up seismic recorder, *Mar. Geopys. Res.*, **1**(1), 91–98, doi: 10.1007/BF00310012.

Williams, E. F., Fernández-Ruiz, M. R., Magalhaes, R., Vanthillo, R., Zhan, Z., González-Herráez, M. & Martins, H. F., 2019. Distributed sensing of microseisms and teleseisms with submarine dark fibers, *Nat. Commun.*, **10**, 5778, doi: 10.1038/s41467–019–13262–7.

Wright, I. C., Chadwick Jr., W. W., de Ronde, C. E. J., Reymond, D., Hyvernaud, O., Gennerich, H.-H., Stoffers, P., Mackay, K., Dunkin, M. A. & Bannister, S. C., 2008. Collapse and reconstruction of Monowai submarine volcano, Kermadec arc, 1998–2004, *J. Geophys. Res.*, **113**, B08S03, doi: 10.1029/2007JB005138.

Zhao, D., Xu, Y., Wiens, D. A., Dorman, L., Hildebrand, J. & Webb, S., 1997. Depth extent of the Lau back-arc spreading center and its relation to subduction processes, *Science*, **278**(5336), 254–257, doi: 10.1126/science.278.5336.254.